

Ultrashort Laser Pulses from Optical Parametric Amplifiers and Oscillators

Von der Fakultät für Mathematik und Physik
der Gottfried Wilhelm Leibniz Universität Hannover
zur Erlangung des Grades

Doktor der Naturwissenschaften

- Dr. rer. nat. -

genehmigte Dissertation

von

Dipl.-Ing. (FH) Tino Lang

geboren am 07.06.1978 in Reichenbach im Vogtland

2014

Referent: Prof. Dr. U. Morgner
Korreferent: Prof. Dr. Franz Kärtner
Korreferent: Prof. Dr. Christian Ospelkaus
Tag der Promotion: 18.07.2014

Kurzfassung

Tino Lang

Ultrakurze Pulse mittels nichtkollinearen Optisch Parametrischen Verstärkern und Oszillatoren

Hochenergetische und hochrepetierende Laserpulse können heutzutage mit Pulsdauern im Bereich nur weniger optischer Zyklen und mehreren hundert MW Spitzenleistung erzeugt werden. Durch diese einzigartigen Eigenschaften sind sie Grundlage wissenschaftlicher Anwendungen quer über alle Fachgebiete. Ultrabreitbandige Ti:Saphir Lasersysteme und Verstärker sind dabei die vorherrschenden Technologien. Allerdings sind die erreichbaren Ausgangsleistungen und die spektralen Spezifikationen dieser Systeme, aufgrund des thermischen Eintrags im Laserkristall sowie dessen begrenztes Emissionsspektrums, grundsätzlichen Limitationen unterworfen.

Im Gegensatz dazu wird in optisch parametrischen Verstärkern (OPAs) und Oszillatoren (OPOs) aufgrund ihres Prinzips keine Energie innerhalb des Kristalls gespeichert. Dementsprechend können die aktuellen Fortschritte bezüglich der Leistungsskalierung geeigneter Pumpquellen, wie Yb-basierter Scheibenlaser und Faserverstärker, direkt genutzt werden. Des Weiteren ermöglicht ein nichtkollineares Phasenanpassungskonzept ein wesentlich breiteres Verstärkungsfenster als Ti:Saphir, welches zudem vom UV bis in den IR-Spektralbereich verschoben werden kann.

Im Rahmen dieser Arbeit wird die komplexe raum-zeitliche Pulsformungsdynamik während eines solchen Verstärkungsprozesses untersucht. Die umfassende Analyse aktueller OPA-Systeme mittels einer neuartigen (2+1)D Simulation ermöglicht dabei Erkenntnisse über das Zusammenspiel aller parasitären und raum-zeitlichen Effekte. Diese Erkenntnisse haben unter anderem zur Entwicklung eines nichtkollinearen optisch parametrischen Oszillators (NOPO) geführt, welcher zum ersten Mal die Vorteile oktavbreiter dispersiver Spiegel mit der außerordentlichen Verstärkungsbandbreite des nichtkollinearen parametrischen Verstärkungsprozesses kombiniert. Dies ermöglicht entweder ein schnelles, schmalbandiges Durchstimmungsverhalten oder die Erzeugung ultrakurzer Pulse mit nur wenigen optischen Zyklen. Beide Konzepte wurden im Rahmen dieser Arbeit sowohl realisiert als auch analysiert. Die dabei erzielten Ergebnisse stellen den NOPO als vielversprechenden und skalierbaren Konkurrenten zum alteingesessenen Ti:Saphir Laser dar.

Schlagnote: Optisch parametrische Verstärker und Oszillatoren, nichtkollineare Phasenanpassung, (2+1)D Simulation, chi2D, parasitäre und raum-zeitliche Effekte

Abstract

Tino Lang

Ultrashort Laser Pulses from Optical Parametric Amplifiers and Oscillators

Ultrashort, highly energetic and repetitive laser pulses, as they can nowadays be generated down to the few-cycle pulse duration and with several hundreds of MWs of peak power opened a wide field of applications in physics, chemistry and life-science. These pulses are usually provided by ultra-broadband Ti:sapphire laser systems. However, these systems are fundamentally restricted in their output power and spectral bandwidth due to unavoidable limitations caused by the quantum-defect heating and the limited emission spectrum of the laser crystal.

In contrast, optical parametric amplifiers (OPAs) and oscillators (OPOs) have many advantageous aspects against these lasers. So, the recent power scaling of Yb-based thin-disk lasers can be easily transferred to a power scaling of these systems, since no energy is stored in the crystal within the parametric process. Furthermore, the non-collinear parametric concept allows for a much broader amplification window than any laser material which in addition can be shifted from the UV to the IR.

This thesis concerns the investigation of the complex spatiotemporal dynamics during such an ultra-broadband non-collinear amplification process. The comprehensive analysis of different state-of-the-art OPAs, aided by the use of a novel (2+1) dimensional simulation model, will gain the knowledge about the interplay of the different parasitic and spatiotemporal effects during the process.

The deep insights achieved by these studies will not only help for the development of future OPA-systems, but also a novel non-collinear optical parametric oscillator (NOPO) has been developed within this work. This NOPO firstly combines the advantages of octave-spanning double-chirped mirrors, the new high-power pump laser technologies, with the ultra-broadband non-collinear phase-matching concept. This enables either a rapidly narrowband tuning behaviour or the generation of few-cycle pulses. Both concepts are realized and analyzed within this work. Accordingly, the presented results show that the ultra-broadband NOPO is the most promising candidate to supersede the Ti:sapphire laser, especially beyond the NIR-spectral range.

Key words: Optical parametric amplifier and oscillator, ultra-broad non-collinear phase-matching, (2+1)D simulation, chi²D, parasitic and spatiotemporal effects

Contents

1	Introduction	1
1.1	Motivation	1
1.2	Overview	2
2	Theory of optical parametric processes	5
2.1	Nonlinear interaction of ultrashort pulses in birefringent crystals . . .	6
2.1.1	Mathematical formalism of linear propagation	7
2.1.2	Generalized coupled equations for second-order nonlinear interaction	11
2.2	Phase-matching and spatiotemporal effects in parametric amplifiers .	14
2.2.1	General aspects of the phase-matching conditions	14
2.2.2	Geometric aspects of non-collinear parametric amplification .	18
2.2.3	Temporal aspects of non-collinear parametric amplification . .	21
2.3	Simulation of ultrashort-pulses optical parametric interaction	23
2.3.1	(2+1) dimensional Fourier split-step algorithms	24
2.3.2	Interpretation of simulation data	29
3	Temporal and spatial effects in ultra-broadband parametric amplifiers	33
3.1	Double stage high power OPCPA-system	34
3.1.1	Experimental verification of the numerical model	34
3.1.2	Fundamental properties and phase relations of cascaded mixing products in high power OPCPAs	38
3.2	Two-color pumped sequential OPCPA-system	45
3.2.1	Experimental conditions	46
3.2.2	Unexpected amplification bandwidth and spectral features . .	48
3.3	Limits of the non-collinear phase-matching geometries	51
3.4	Conclusion	59

4 Ultra-broadband phase-matched Non-collinear Optical Parametric Oscillators	61
4.1 Widely tuneable femtosecond NOPO	63
4.1.1 Theoretical considerations	64
4.1.2 Experimental setup	68
4.1.3 Experimental results and discussion	71
4.2 NOPO with KLM mode-locking and breathing pulse dispersion management	84
4.2.1 Experimental setup	85
4.2.2 First experimental results	88
5 Conclusion	91
6 Outlook	95
6.0.3 (2+1)D NOPO simulation	96
Bibliography	101
List of Figures	107
Appendix	109
A Acknowledgements (German)	111
B Curriculum Vitae	113
C Scientific Publications	115

Chapter 1

Introduction

1.1 Motivation

The most exciting questions in nature are most often found at the very limits of our observable world. Ultra-short and high energetic light pulses can nowadays be generated down to a few femtosecond time duration and their unique properties provide a window into the smallest and fastest processes in physics. The new fundamental insights in nature, e.g. real-time observation of the electronic dynamics in chemical reactions [Liu13] or the attosecond physics on the atomic level [Kra09b, Sch13], are thereby not only overwhelming for the scientists, but also address fundamental questions about the true nature of our world.

But also in our daily life ultra-short pulsed laser sources enable new technologies and products, as for example extremely precise processing of a variety of materials. Especially, their strong impact in the field of life-science is greatly beneficial for the biological and medical progress. For instance, pump-probe techniques using ultra-short pulses can provide information about the different biochemical kinetics of specific organic macromolecules and thus allow for the possibility to distinguish in-vivo between normal and cancerous cells [Liu02].

The most widespread systems providing these ultra-short laser pulses are based on Ti:sapphire laser and amplifier technologies. However, no significant progress in the development of these systems has been made in the last decade, which is mainly caused by fundamental limitations of the laser concept itself. Accordingly, the main issue for a further power scaling is the unavoidable heat load in the laser crystal. Furthermore, also the gain spectrum is limited due to the emission wavelengths of the material. Especially this last point restricts the availability of ultra-short laser pulses with high repetition rates in the UV and the IR-spectral range. Moreover, the amplification of these short pulses in the NIR is strongly restricted due to the gain narrowing of Ti:sapphire amplifiers to approximately 30 fs. Here, low efficient nonlin-

ear spectral broadening concepts were necessary for a subsequential re-compression of these pulses.

A novel approach for the generation, as well as for the amplification of few-cycle high energy pulses at high repetition rates, is based on a completely different concept: the parametric amplification. These 2nd order nonlinear processes enable much broader amplification windows than any laser medium. Additionally, due to the multitude of different nonlinear crystals available, almost any spectral region within their transparency ranges is accessible. So, nowadays optical parametric oscillators (OPOs) are commercially available for the generation of fs-laser pulses covering the whole spectral range from UV up to the far-IR spectral region. However, their output power is mainly limited by Ti:sapphire laser used for pumping these systems. Moreover, these tuneable OPOs are based on narrowband phase-matching concepts which drastically limits the tuning speed (which can take tens of seconds). As it will be shown in this work, parametric amplification can also offer ultra-broad gain bandwidth in both NOPO and the OPCPA concepts with very high efficiencies. On the one hand, the scaling properties and broad bandwidth are very beneficial for few-cycle high repetition OPCPA systems which are an ideal light source e.g. for attosecond physics spectroscopy.

On the other hand, these properties also allow for a next generation parametric oscillator, the NOPO, which for the first time combines ultra-broadband noncollinear phase-matching with high power Yb-based thin-disk pump sources. Accordingly, the recent power scaling of these systems [Sar12a] can be directly transferred to the NOPO due to the absence of any quantum-defect heating in the nonlinear crystal. Moreover, the use of double-chirped mirrors, providing a flat phase over one optical octave [Kae01] in the NOPO, enables a fast ramping of the output spectrum over a wide range since no slow adaption of the phase-matching is necessary. Furthermore, since the simultaneously phase-matched gain window supports a few-cycle pulse duration, the NOPO is a potential candidate to supersede the ultra-broadband Ti:sapphire lasers.

1.2 Overview

The NOPO developed in the scope of this work can be seen as a first demonstration of a new exciting type of light sources providing outstanding parameters for many imaging or spectroscopic applications in physics, biology and medicine. Besides the experimental realization of the system, an extensive investigation will be made about the complex spatial and temporal dynamics which take place during parametric

amplification processes. The corresponding simulation model presented in this thesis allows for a deeper understanding of the parametric amplification process itself. Thereby, apart from the new insights provided about the process new design concepts can be analyzed and predicted both for OPCPA or NOPO systems.

The thesis is structured as follows: The next chapter will introduce the mathematical description of the non-collinear propagation and the 2nd order parametric interaction of ultra-short optical pulses in birefringent crystals. This treatment will be the basis of a (2+1) dimensional algorithm for the numerical simulation of ultra-broadband parametric amplifiers. Additionally, the complex spatiotemporal effects, as they occur during this non-collinear interaction processes, will be explained separately on a simplified example which will be the basis for later discussions and conclusions.

In the following Chapt.3.3, the developed simulation model will be used to get deeper insights into the spatiotemporal and parasitic effects during the parametric amplification processes. Therefore two different in-house built state-of-the-art optical parametric amplifier systems will be extensively analyzed. The conclusions, raising from the comparison of the experimental and the simulation results, will be used to verify the numerical model and answer several open questions about the experimental observations. Based on the comparison of the systems operating in different power regimes the formulation of guidelines for the future OPCPA development is possible.

In Chapt.4, the experimental realization of the novel ultra-broadband NOPO concept developed in this work will be presented. The first system is a rapidly and widely tuneable NOPO which will be deeply characterized. Accordingly the development of the first ultra-broadband two-foci NOPO with a Kerr-lens assisted mode-locking mechanism and a breathing pulse dispersion management is presented.

Finally both, the theoretical and the experimental part of this work, will be summarized together with the final conclusions and the future prospects and steps towards a new power scalable NOPO generation providing stable few-cycle pulse trains.

The outlook of this work will show the first simulation results of the on-going numerical investigations of the ultra-broadband NOPO. These preliminary results will demonstrate impressively the potential of the (2+1)D simulation for the future development in this most promising field of research.

Chapter 2

Theory of optical parametric processes

In this chapter the principles of the nonlinear parametric interaction between ultrashort light pulses will be introduced. The description will be focused on the non-collinear pulse propagation in one defined plane of birefringent nonlinear crystals.

The particular goal of this work is to give a deeper understanding of the spatial and temporal pulse dynamics during the rather complex non-collinear ultra-broadband interaction in optical parametric amplification processes. Both propagation and nonlinear interaction will be discussed in (2+1) dimensions including information about the amplitude and phase of the ordinary and extraordinary field in space and time. Based on the well known mathematical description of the ultrashort pulse propagation and second order nonlinear interaction, the basic equation for a (2+1) dimensional numerical model will be introduced. It should be mentioned, that for an interested reader a comprehensive or explicit derivation of the underlying equations and basic concepts are referred to the corresponding review papers or text books of the particular subject. Rather, the focusing on the interpretation of the mathematical issues and the explanation of their consequences in Sec. 2.1 provide the basis for discussions and conclusions arising from the comparison between experiment and simulation which is the scope of the next chapters.

Accordingly, the algorithm of the simulation, including all second order nonlinear mixing processes¹ and the pulse propagation due to dispersion and birefringence of the nonlinear crystals, will be explained in detail in Sec. 2.3. Nevertheless, because the mentioned broadband and non-collinear amplification processes are extremely sensitive regarding the relative phase and propagation of the involved pulses to each

¹In addition to the second-order interaction also one special third-order process is implemented: the spectral broadening due to self-phase modulation (SPM) which goes along with the self-focusing effect (see Sec. 2.3.1).

other, the model needs to be verified. Therefore, in Sec. 2.2 an approximation-free method for the analytical calculation of the phase-matching conditions will be introduced, which helps to address features visible in the experiment and simulation and to understand the interplay of parasitic, temporal and spatial effects.

Finally, the (2+1)D simulation will be tested regarding the approximations made in the model and the limitations due to the neglect of the third spatial dimension, which will be discussed in the last section of this chapter. Furthermore, an example will help to understand how to interpret the quite complex simulation data.

2.1 Nonlinear interaction of ultrashort pulses in birefringent crystals

The evolution of ultrashort light pulses or optical fields in general can be fully mathematically expressed by Maxwell's equations. However, no analytical solution of these differential equations exists that would describe how the light behaves exactly without well known simplifications such as the paraxial wave approximation or the slowly varying envelope approximation [Sie86].

The particular scope of this work is the non-collinear propagation of ultrashort pulses and their nonlinear interaction in birefringent crystals. Furthermore, as it will be explained later, due to phase-matching considerations the propagation of these pulses can be restricted to the principle plane² which includes the walk-off direction in the birefringent crystal. Thus, the electric field orientation of a pulse propagating in a certain direction z can be expressed by the superposition of only two orthogonally polarized complex electric fields: the ordinary field $E_o = \vec{e}_{n_o} A e^{ikz}$ and the extraordinary field $E_e = \vec{e}_{n_e} A e^{ikz}$. The unity vectors \vec{e}_{n_o} and \vec{e}_{n_e} pointing in the direction of the ordinary and extraordinary dielectric polarizations³ in the crystal, respectively.

In order to introduce the mathematical formalism to perform the propagation steps in the numerical model, the used propagation equations will be defined and discussed in the next section. Especially the used approximations and limitations of the employed (2+1) dimensional treatment of the pulse propagation with only two

² A crystallographic plane which is defined by two main axes of the refractive index ellipsoid [Dmi10].

³The ordinary direction is defined by the dielectric polarization with a refractive index n_o invariant to the orientation of the wavevector of the optical field in a principle plane of the crystal. The extraordinary direction is orthogonal to both the wavevector and the ordinary direction. The corresponding coordinate on the index ellipsoid defines the extraordinary refractive index n_e .

equations including the dispersion, refraction and the relative propagation as well as the walk-off will be subject of discussion.

2.1.1 Mathematical formalism of linear propagation

By considering the evolution of the pulses only along the z -direction, their complex electric field amplitude A , with an accumulated phase (e^{ikz}) during propagation, can be defined in time and space for each position along the z -coordinate. The wavevectors of this field are given by the dispersion relation of light $|\vec{k}| = \frac{2\pi}{\lambda}n$ with the optical refractive index n of the medium and the vacuum wavelength λ . As previously mentioned, in a birefringent crystal this refractive index depends on the polarization of the optical field. By defining ordinary and extraordinary wavevectors to lay in a principle plane of the crystal, an optical pulse at a certain position along z can then be represented by the superposition of orthogonally polarized complex field amplitudes in space and time ($E_o(x, y, t)$, $E_e(x, y, t)$).

To describe the evolution of these complex optical fields between two positions along the z -coordinate a solution⁴ of the paraxial wave equation can be used [Kog66], which is based on the Fourier representation of the complex electric field in time and space $E(x, y, t)$. This Fourier space is defined by the corresponding spatial frequencies (f_x, f_y) and temporal/optical frequencies (f_t) at each position along the z -coordinate [Fle76, Fle83]. In other words, a complicated complex wave in x, y and t can be described by the superposition of a series of plane waves, each with the spatial frequencies f_x and f_y and their particular optical wavelength $\lambda = \frac{c \cdot n}{f_t}$. Hence, the propagation of an optical pulse in z -direction can be handled by adding the accumulate phase $e^{ik_z z}$, with $k_z(\lambda, f_x, f_y) = [k(\lambda)^2 - (2\pi f_x)^2 - (2\pi f_y)^2]^{1/2}$, to each plane wave with their particular spatial and optical frequency components in the Fourier representation of $E(x, y, t)$ [Szi75].

Another important simplification should be introduced and explained at this point: the negligence of one spatial dimension to a (2+1) dimensional treatment of the pulse propagation. In other words, the electrical fields of all involved pulses are only considered in one plane which is defined to include the walk-off and the non-collinear propagation between all pulses. This especially makes sense, since the definition of the direction of the walk-off and electric field vector can become complicated in bi-axial birefringent crystals. Additionally, no further important phase-matching possibilities outside these principle planes can be expected, which is also proven by

⁴This solution requires the neglect of the fast oscillating term in z -direction which implies that the electric field will not change much within a propagation distance in the order of the optical wavelength.

the experimental observations as shown in the next chapter by photographs of the super-fluorescence of a high-power OPCPA-system in Fig. 3.3 (c).

Under the mentioned conditions the still rather complex and interesting spatial evolution of the light field during the nonlinear interaction process mainly takes place in one spatial dimension. There are two reasons for that: firstly, the walk-off between pulses with different polarizations can be observed in this dimension which is caused by the separation of the Poynting and wavevector in the birefringent medium. The walk-off even affects the beam profile, bandwidth and the efficiency of nonlinear processes with collinear phase-matching conditions. Secondly, and even more important is the massive spatial separation of the involved pulses due to non-collinear phase-matching geometries taking place in this considered dimension. This effect, which allows for an ultra-broadband phase-matching and drastically influences the efficiency of a nonlinear process, will be one of the main issues in the following chapters.

In contrast to this spatial dimension, which will be called x from now on, there is no spatial separation of the optical pulses in the orthogonal dimension y under the mentioned simplifications. Moreover, at least within the Rayleigh length, it can also be assumed that the light diffraction is negligible in this spatial dimension, whereas the separation of the pulses in x -direction can cause a significant reduction of the beam quality (M_x^2) due to the nonlinear interaction, as explained later.

Consequently it is sufficient to restrict the treatment of the spatial and temporal evolution of all involved optical pulses to (2+1) dimensions, including the temporal axis t and the important spatial axis x with their corresponding Fourier components f_t and f_x , at each position along the propagation direction z .

Considering all simplifications and restrictions expressed in this section⁵, the temporal and spatial evolution of the superposition of all differently polarized optical pulses can be performed for a propagation step in z -direction by applying the two propagation equations for E_o and E_e in the Fourier domain:

$$E_o(f_t, f_x, z + dz) = E_o(f_t, f_x, z) e^{i\sqrt{\left(\frac{2\pi f_t n_o(f_t)}{c}\right)^2 - (2\pi f_x)^2} dz}, \quad (2.1)$$

⁵ - slowly varying envelope approximation and paraxial wave approximation

- no diffraction and propagation in y -direction ($k_y = 0$): $k_z(\lambda, f_x, f_y) \approx [k(\lambda)^2 - (2\pi f_x)^2]^{1/2}$
 - restriction to one principle plane of the birefringent crystal given by the main axis of the refractive index ellipsoid

includes all ordinary polarized fields with their corresponding wavelength dependent refractive indices $n_o(f_t)$ given by the Sellmeier formalism. The extraordinary field

$$E_e(f_t, f_x, z + dz) = E_e(f_t, f_x, z) e^{i\sqrt{\left(\frac{2\pi f_t}{c} n_e(f_t, f_x)\right)^2 - (2\pi f_x)^2} dz}, \quad (2.2)$$

involves all extraordinary polarized pulses propagating with the refractive index $n_e(f_t, f_x)$. This extraordinary refractive index depends on the optical frequency as well as on the relative angle ϑ between the propagation direction of each spectral component and the optical axis of the crystal [Dmi10]. Thus, the extraordinary refractive index along a certain propagation direction is given by the index ellipsoid with the ordinary and the extraordinary indices (n_{ea}, n_{oa}) along the optical axes of the crystal.

$$n_e(f_t, \vartheta) = n_{oa} \sqrt{\frac{1 + \tan^2 \vartheta}{1 + (n_{oa}/n_{ea})^2 \tan^2 \vartheta}}. \quad (2.3)$$

Please note that both the relative angle of the optical axis of the crystal θ and the angle of propagation α are measured towards the main propagation direction z (see Fig. 2.1 (a)), such that,

$$\vartheta = \alpha + \theta, \quad (2.4)$$

whereas the angle of propagation α has a well defined connection with the temporal and spatial frequencies of the complex spectral field $E(f_x, f_t)$. This can be

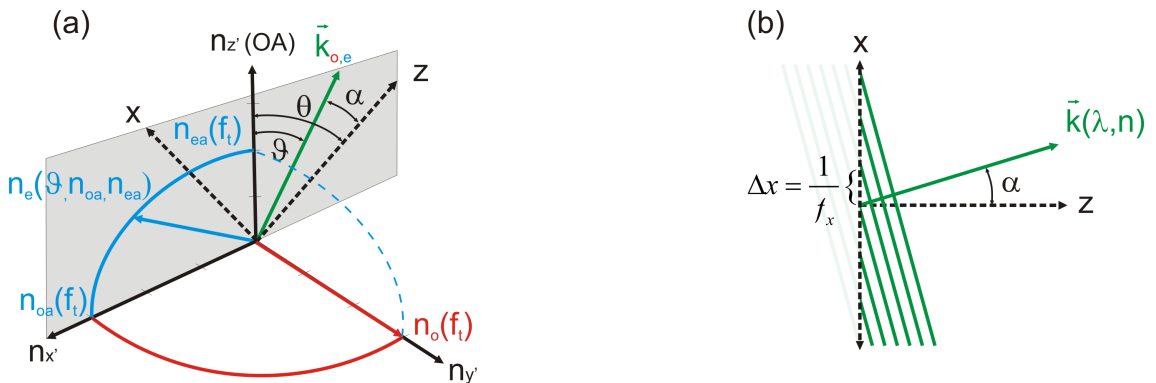


Figure 2.1: Schematic of (a) the propagation direction in a BBO-like index ellipsoid with the optical axes $(n_{x'}, n_{y'}, n_{z'})$ of the crystal, the main propagation direction (z) , the ordinary and extraordinary wavevector of the optical field in $(\vec{k}_{o,e})$. (b) the connection between spatial frequency (f_x) and the propagation angle (α) towards the main propagation.

understood by keeping in mind that the Fourier representation of any spatiotemporal wave front is just described as a series of plane waves with different optical and spatial frequencies. Each spatial frequency of the complex field amplitude at a certain plane orthogonal to z , however, can also be interpreted as the difference / interference of a plane wave propagating exactly in z -direction and one propagating under a relative angle α . Thus, as illustrated in Fig. 2.1 (b), the connection between the relative propagation angle towards the z -direction of a certain plane wave and their spatial frequency can be found by:

$$\sin(\alpha) = f_x \cdot \lambda \cdot n \quad (2.5)$$

Whereas the ordinary refractive index itself does not depend on the propagation direction in the birefringent crystal, the equation for the angle between the z -axis and the wavevector of a certain extraordinary plane wave is given by:

$$\alpha_e(f_t, f_x, n_e) = \arcsin \frac{f_x}{f_t} \frac{c}{n_e(f_t, \alpha_e + \theta)} \quad (2.6)$$

Because of this interdependence between $\alpha_e(f_t, f_x, n_e)$ and $n_e(f_t, \alpha_e + \theta)$ an iterative algorithm can be used to calculate the extraordinary refractive index for each element of the field $E_e(f_t, f_x)$. In a first iteration step, the refractive index is assumed to be independent of the propagation direction, so a first approximation of the propagation angles $\alpha_e(f_t, f_x)$ of each field element can be calculated by Eq.(2.5). In the following iterations the extraordinary refractive index is calculated based on the previously approximated propagation directions leading to a more precise result with each iteration step. The iteration converges rather quickly and is stopped, when the change in $\alpha_e(f_t, f_x, n_e)$ and $n_e(f_t, \alpha_e + \theta)$ drops below a certain threshold.

The wavelength dependent ordinary phase and the inhomogeneous angle and wavelength dependent extraordinary phase which are added by these refractive index fields at each propagation step dz Eq.(2.2), automatically implements dispersion, diffraction, and walk-off of all involved fields in just one single computational step in the spectral domain. Of course the same applies to the symmetric ordinary field with a refractive index distribution which is constant along f_x , hence no walk-off effect can be observed for this polarization.

It should be mentioned again that due to the two-dimensional representation of the light field, diffraction is only considered in the x -dimension, so that for tightly focused pulses with a Rayleigh length smaller than the propagation length in the crystal, the (2+1)D model produces a significant error concerning the intensity evolution. This occurs because of the two dimensional spreading of the energy in the

model, leading to a linear decrease of the intensity in case of a divergent beam, whereas in a three-dimensional space the intensity proportionally decreases with the square of the distance. This is a strong restriction, especially with respect to a quantitative calculation of the nonlinear interaction efficiency between pulses which of course shows a strong dependence on the intensity. Fortunately, as discussed in detail in the next section, the crystal length for the generation of ultrashort pulses should never be longer than the Rayleigh length of the involved pulse, because of phase-matching and efficiency aspects.

2.1.2 Generalized coupled equations for second-order nonlinear interaction

The basics of second-order nonlinear processes, e.g. the second harmonic frequency generation (SHG), the sum frequency generation (SFG) or the difference frequency generation (DFG) - are well known and matter of ongoing investigation since decades [Fra61, Boy08]. A rich variety of nonlinear χ^2 -crystals in which these nonlinear processes are phase-matched and which can be used for an efficient conversion, are well established and can be found in many publications and text books. Therefore, the following section will not be concerned with the detailed derivation and description of all the basic equations, parameters and crystal geometries, e.g. the detailed crystallographic structure of β -Barium-Borat (BBO). For these basic concepts, the reader shall be referred to [Dmi10].

Rather, the focus of discussion shall lay on how to establish a mathematical description that can be used as a basis for the numerical model, which has been developed in this work. This model offers significant improvements in the description of the rich spatiotemporal dynamics of the interplay between different nonlinear interactions compared to previous works.

For example, the typical method for the calculation of the parametric difference frequency generation is based on a split-step Fourier method solving the three coupled nonlinear differential equations [Con10],

$$\frac{\partial}{\partial z} E_{\omega_p} \sim -i E_{\omega_i} E_{\omega_s}, \quad \frac{\partial}{\partial z} E_{\omega_s} \sim -i E_{\omega_p} E_{\omega_i}^*, \quad \frac{\partial}{\partial z} E_{\omega_i} \sim -i E_{\omega_p} E_{\omega_s}^*. \quad (2.7)$$

Each equation describes the change for one specific complex pump, signal and idler wave (E_{ω_p} , E_{ω_s} , E_{ω_i}) separately. Hence, each phase-matched nonlinear process beyond the considered difference mixing needs to be individually implemented by adding additional differential equations for each mixing product [Bro11]. Especially

for new phase-matching concepts and new nonlinear crystals, the relevance of a specific phase-matched mixing process is difficult to estimate.

In contrast, in this work all second-order nonlinear interaction processes of ultrashort light pulses are handled with only two coupled differential equations for the two orthogonal complex optical fields $E_o(t, x)$ and $E_e(t, x)$,

$$\begin{aligned} \frac{\partial E_o(t, x)}{\partial z} &= -i \kappa_o \left(\overbrace{2E_e E_o^* + E_e E_e}_{\text{oo-e}} + \overbrace{E_e E_e}_{\text{ee-o}} + \overbrace{2E_e E_e^* + 2E_o E_e^* + 2E_e E_o}_{\text{eo-e}} \right) \\ \frac{\partial E_e(t, x)}{\partial z} &= -i \kappa_e \left(\overbrace{E_o E_o}_{\text{oo-e}} + \overbrace{2E_o E_e^*}_{\text{ee-o}} + \overbrace{2E_e E_o^*}_{\text{eo-e}} + \overbrace{2E_e E_o}_{\text{eo-e}} + \overbrace{2E_o E_o^*}_{\text{eo-o}} \right), \end{aligned} \quad (2.8)$$

with the nonlinear interaction parameter:

$$\kappa_{o,e} = \frac{\pi f_t d_{\text{eff}}}{n_{o,e}(f_t, f_x) c}. \quad (2.9)$$

In these equations the nonlinear coefficient d_{eff} is assumed to be constant for all processes and wavelengths, but for a more accurate quantification of each process, it can be easily implemented separately. However, since κ depends on the optical frequency f_t as well as on the direction dependent refractive index $n_e(f_t, f_x)$ for the extraordinary field, the implementation of the nonlinear parameter in the numerical model is realized in the spectral domain $E_{o/e}(f_t, f_x) = \mathcal{F}(E_{o/e}(t, x))$ as described in the next section.

To explain the origin and the effect of the different terms in the two coupled equations, which include all possible nonlinear mixing processes between the involved pulses, a simple example shall be given in Fig. 2.2. The particular example will describe the forward and back-conversion processes, which occur in a Type-II (eo-e) sum frequency conversion process, exemplary for three specific frequencies of the involved pulses.

In the simplified example the ordinary and the extraordinary fields ($E_{o/e}$) contain only two different optical waves with the frequencies ω_1 and ω_2 . As illustrated on the top right hand side of Fig. 2.2 the whole process starts with the up-conversion of both fields each containing the frequency ω_1 and frequency ω_2 , which can either be ordinary (red) or extraordinary polarized (black). As indicated by the equation ($\frac{\partial E_e}{\partial z} \sim -i2E_e E_o$) a new wave in the extraordinary field is created with a $\frac{\pi}{2}$ -phase-shift and a frequency $\omega_3 = \omega_1 + \omega_2$. Of course, the energy conservation has to be fulfilled, which becomes clear by keeping in mind the physical process of two photons which create a new one containing the energy of both. Consequently, the

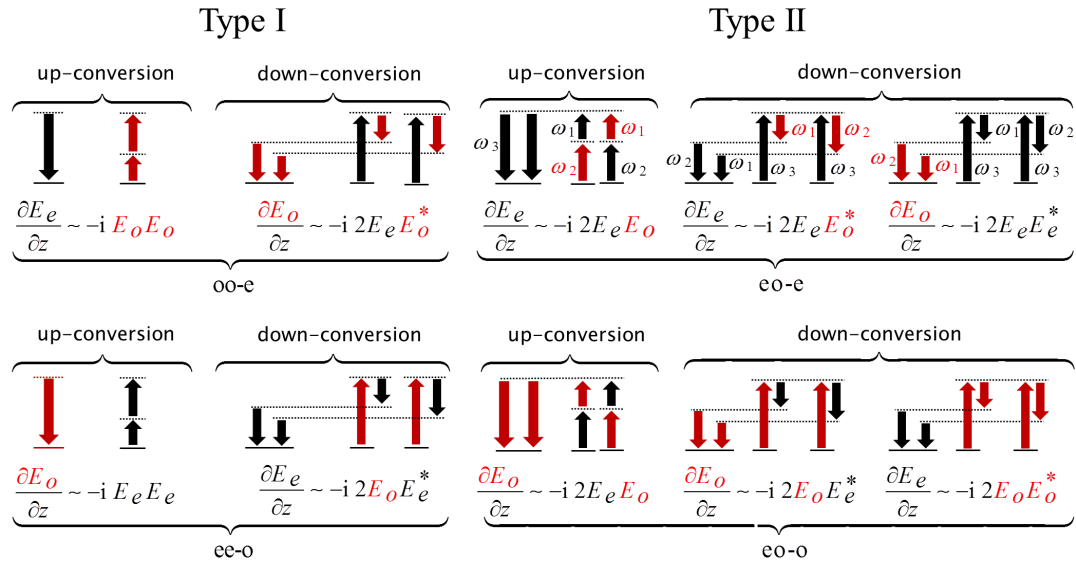


Figure 2.2: Illustration of the origin of the two generalized coupled equations in Eq. (2.8). The schematic shows the energy level diagram and the related coupled equations of all possible second order mixing processes in a principle plane of a birefringent nonlinear crystal, exemplary for three waves with the frequencies $\omega_1, \omega_2, \omega_3$. The processes are sorted by the type of phase-matching and the polarization of the involved electric fields.

two original photons need to be destroyed. This process is described by the down-conversion or difference frequency conversion between the newly created waves and the original waves. In this case there are two possibilities, namely $\omega_3 - \omega_1$ and $\omega_3 - \omega_2$, two new waves with the frequency ω_1 in the ordinary field and ω_2 in the extraordinary field are additionally created but with a phase-shift of π . This leads to a destructive interference between the two original waves which finally fulfills the energy conservation.

The same principle can be applied to each process shown in Fig. 2.2 which finally leads to Eq. (2.8). Thus, the change in the orthogonal optical fields with respect to every single mixing process is considered, notwithstanding that due to the dispersion each of these processes is not automatically phase-matched. As it will be explained in Sec. 2.3.1, in the numerical model this fact is implemented by the split-step algorithm which combines the nonlinear interaction with the phase-matching conditions given by the temporal and angular dispersed propagation considered by Eq. (2.2). In the numerical model, which includes all phase-matched mixing processes simultaneously, it is not always obvious which process causes a certain feature in the simulation results. Thus, an analytic method is introduced in the next section, which helps

to illustrate the phase-matched spectral components with respect to the nonlinear process and the propagation direction and polarization of the involved optical fields.

2.2 Phase-matching and spatiotemporal effects in parametric amplifiers

Nonlinear conversion processes often exhibit prominent and quite complicated features in the spectral and spatiotemporal phase and intensity distribution. These experimental observations cannot be explained analytically since they are mainly caused by propagation effects and parasitic nonlinear processes.

In particular, the spatial and temporal gain evolution during a parametric amplification process can vary strongly in the different non-collinear geometries. This is especially the case for beam sizes in the order of the displacement due to the walk-off and non-collinear propagation with respect to the crystal length. With regard to the technical complexity of the pump systems it is desirable to keep the required pump pulse energies in a moderate regime. In order to reach the necessary peak intensities for a sufficient conversion efficiency the pump beam needs to be focused to a size where these geometrical effects become one of the main issues of the optical parametric amplification.

This section will distinguish the influences of different phase-matching processes (Sec. 2.2.1), spatial walk-off-effects between the interacting pulses (Sec. 2.2.2) and special temporal aspects like the compression of certain spectral components caused by the dispersion in the birefringent crystals (Sec. 2.2.3). In order to get a better understanding on how each of these particular processes can be explained, the complicated nonlinear pulse shaping dynamics is discussed at the example of a broadband non-collinear parametric amplification process. It will be discussed in detail how each effect contributes to the observations, which can be seen in the experiment and the numerical simulation for the different phase-matching geometries.

Keeping in mind this simplified processes and considerations, as explained in the following, will help to interpret the more complicated implications in the experimental chapters.

2.2.1 General aspects of the phase-matching conditions

The nonlinear interaction of laser pulses as well as the generation of second-order nonlinear frequency mixing products is a fundamental process which occurs in every non-centrosymmetric medium, as long as the driving pulses are intense enough

(typically in the range of $\frac{GW}{cm^2}$). Of course, similar to any other physical mechanism, the conservation of momentum and energy has to be fulfilled as well. For very short interaction lengths, in the range of the optical wavelength, and for ultrashort pulses, the uncertainty of the momentum allows for almost any thinkable nonlinear conversion process. However, since the efficiency of the nonlinear processes shows a quadratic dependence with respect to the interaction length, the used crystal length for a typical parametric conversion process is in the range of some tens of micrometer to millimeter. Consequently, the relative phase between the interacting pulses is dominated by the dispersion in the nonlinear medium [Boy08].

Keeping in mind the variety of possible mixing processes which can occur in one single nonlinear crystal as illustrated in Fig. 2.2, the question of which one is efficiently amplified over a certain interaction length with respect to the phase-matching conditions, cannot be overseen by a single analytical formalism. Nevertheless, for each process in particular an analytical formalism can be found separately, describing which wavelengths under which angle are phase-matched for a certain nonlinear crystal and process. As previously mentioned, this analytical method can help in finding a connection between a particular feature observed in the experiment and simulation to a certain process.

This section shall introduce this analytical formalism and exemplarily discuss the consequences of the simultaneous occurrence of two phase-matched processes in a broadband non-collinear optical parametric amplification process. Besides the well known parasitic effects, which differ in the two phase-matching geometries [Oie97, Cer03, Bro11], additional considerations, e.g. the self-compression of the idler etc., will be pointed out in the next chapters.

The analyzed parametric amplification process is based on a difference frequency generation (DFG) pumped by a narrowband pulse with the wavevector \mathbf{k}_p which points in z -direction ($\alpha_p = 0$) as illustrated in Fig. 2.3. The seed pulse which is going to be amplified to a broadband signal pulse propagates under a certain angle α_s which is represented by the multi-color wavevectors \mathbf{k}_s in the schematic symbolizing the different wavelengths. In order to realize a broadband amplification of the seed, the residual phase-mismatch ($\Delta\vec{\mathbf{k}} = \vec{\mathbf{k}}_p - \vec{\mathbf{k}}_s - \vec{\mathbf{k}}_i$) between pump, signal and the generated idler pulses needs to be small enough to avoid substantial back conversion during the propagation within the crystal length.

For an (oo-e) non-collinear DFG process in BBO, pumped by an extraordinary polarized narrowband pulse, this residual phase-mismatch, with respect to the differ-

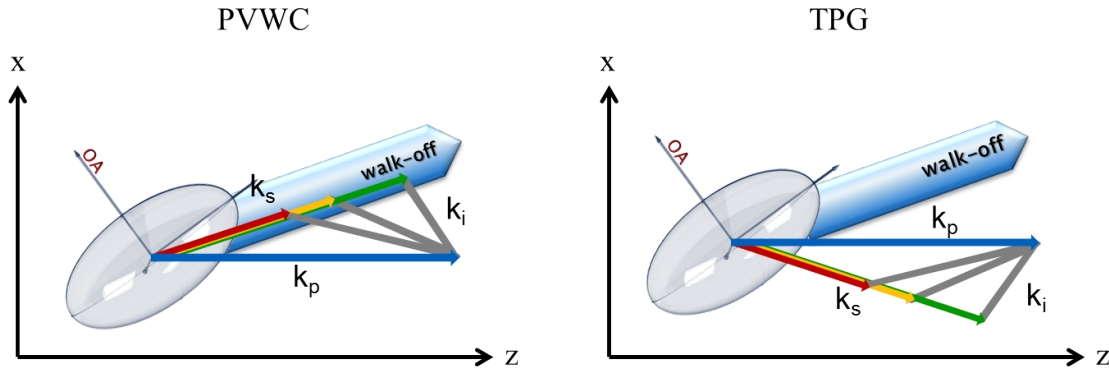


Figure 2.3: Schematic of the different non-collinear phase-matching geometries in a negative birefringent crystal: left: the Poynting Vector Walk-off Compensation geometry (PVWC), right: the Tangential Phase-matching Geometry (TPG), OA: optical axis, k_s : wavevectors of the broadband signal pulse, k_p : narrowband pump pulse, k_i : angular dispersed broadband idler pulse, blue bold arrow: Poynting vector of the extraordinary pump beam

ent propagation angles α_s and wavelengths λ_s of the signal pulse, can be calculated by:

$$\Delta k(\lambda_s, \alpha_s)_{\text{DFG}} = \frac{\frac{n_e(\lambda_p, \theta)}{\lambda_p} - \sin(\alpha_s) \frac{n_o(\lambda_s)}{\lambda_s} - \sin(\alpha_i) \frac{n_o(\lambda_i)}{\lambda_i}}{\sin(\alpha_i)}, \quad (2.10)$$

where the projected length of the pump, signal and idler wavevectors are given by the Sellmeier formalism and the corresponding index ellipsoid of the crystal Eq. (2.3). The idler wavelengths are determined by the energy conservation. This defines together with the conservation of momentum the propagation angles of the angularly chirped idler pulse.

$$\cos(\alpha_i) = \frac{\vec{k}_p \vec{e}_z - \vec{k}_s \vec{e}_z}{|\vec{k}_p - \vec{k}_s|} \quad (2.11)$$

The result for three different phase-matching angles θ of the BBO-crystal is shown by the red shaded area in Fig. 2.4. The saturation of the red color represents the expected phase-matched spectral broadness and the acceptance angle for a $L=1$ mm BBO-crystal as it can be calculated by $\text{sinc}(\Delta k L/2)$. As it can be seen, the ordinarily polarized seed pulse can only be efficiently amplified for particular combinations of propagation angles and wavelengths. Thereby, the broadest possible phase-matched bandwidth of the signal pulse can be realized for a phase-matching angle θ of 24.5° (see also Eq. (2.4)) at the "magic angle" of $\alpha = \pm 2.5^\circ$ as shown in Fig. 2.4 (b). As

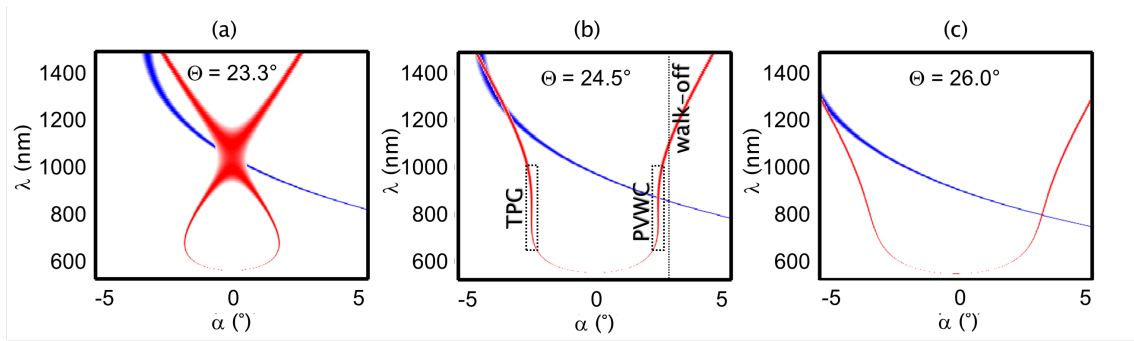


Figure 2.4: Color-maps showing the DFG (red) and the SHG (blue) - phase-matched wavelengths with respect to the propagation angle in 1 mm BBO for $\alpha_p = 0^\circ$ and a pump wavelength of 515 nm for different phase-matching angles θ . The dotted line shows the angle of the pump walk-off. The dotted boxes highlight the two different phase-matching geometries, the tangential phase-matching geometry (TPG) and the Poynting vector walk-off compensation geometry (PVWC).

indicated by the black dashed line in Fig. 2.4(b), as well as by the comparison in Fig. 2.3, the non-collinear arrangement between pump and signal can be either realized in a way which compensates the displacement of the pump due to the walk-off - the Poynting Vector Walk-off Compensation geometry (PVWC) - or the other way around - the Tangential Phase-matching Geometry (TPG). Although in the TPG the signal pulse shows a strong displacement regarding the pump pulse, parts of the angularly chirped idler pulse, however, are now co-propagating with the pump. Nevertheless, the results in terms of the spectrally and angularly distributions of the amplified signal will differ significantly in these two geometries, which is completely disregarded in the analytical considerations.

Another important effect is caused by parasitic conversion processes which are simultaneously phase-matched. To give just one example, by taking a closer look under which angles and wavelengths the amplified ordinary polarized signal pulse is phase-matched for the generation of the second harmonic,

$$\Delta k(\lambda, \alpha)_{\text{SHG}} = 2\pi \left(\frac{n_e(\lambda, \alpha)}{\lambda} - \frac{n_o(2\lambda)}{\lambda} \right), \quad (2.12)$$

it is obvious that in the overlapping phase-matching areas of SHG (blue shaded area in Fig. 2.4) and DFG (red) the two processes will compete with each other. The result will be a very complicated phase and intensity distribution which strongly differs from the expectations given by the analytical calculations [Ros02].

The mentioned geometrical and parasitic effects are just a few of the countless effects that can appear besides the desired nonlinear parametric amplification process. At this point a quantitative prediction, especially for small beam parameters and strong gain factors, can only be given by a numerical model which includes all essential effects occurring in such a process [Lan13].

However, for a qualitative understanding the spatial and temporal pulse evolution can be simplified and discussed separately. In particular, the next two sections will describe how these major effects in combination result in the complex spatiotemporal pulse shaping dynamics as it is observed during the propagation in a non-collinear amplification process.

2.2.2 Geometric aspects of non-collinear parametric amplification

In the previous section the two discussed broadband non-collinear phase-matching geometries can show strong differences regarding the phase-matching of parasitic processes in parametric amplifiers. As already mentioned, the two geometries differ in the most obvious way by the fact that in the Poynting vector walk-off compensation geometry (PVWC) the non-collinear angle of the signal pulse compensates the walk-off angle leading to a long spatial overlap; whereas in the tangential phase-matching geometry (TPG) the strong divergence between pump and seed pulse lead to a very short effective co-propagation length. It is tempting to say that this clearly leads to a more advantageous condition for the PVWC with respect to the efficiency of the process. However, by looking more carefully at the numbers for a specific example, e.g. the PVWC phase-matching geometry in BBO pumped at 515 nm, the walk-off angle of the extraordinary pump beam is 3.3° which is slightly larger than the "magic angle" in BBO with $\sim 2.4^\circ$ for a phase-matching angle of 23.5° . In practice this leads to the situation where a perfect overlap of pump and seed pulse at the very beginning of the crystal (Fig. 2.5(a)) ends with a rather small spatial overlap between pump and signal at the end of the crystal for the specific example shown in Fig. 2.5(b).

In the following, this effect shall be carefully explained in case of the two phase-matching geometries in a BBO crystal and the mentioned numbers. Therefore, Fig. 2.5 shows a very simplified schematic of the spatial evolution of the pump and seed pulse to the depleted pump, amplified signal and generated idler pulse, separated from any other effect occurring during a non-collinear parametric amplification process. To be able to illustrate the transversal displacement of the signal and idler pulses relative to the energy flow of the pump pulse before and after the ampli-

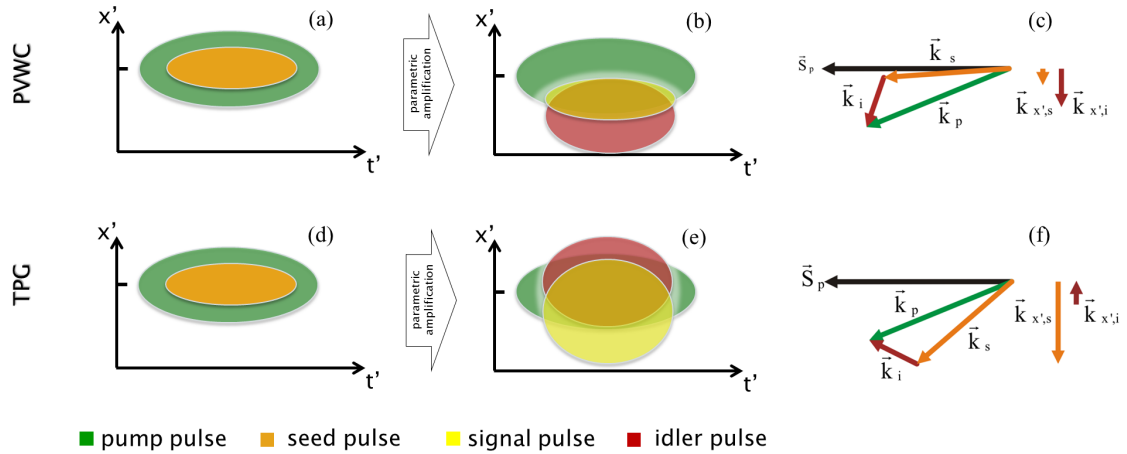


Figure 2.5: Schematic of spatial pulse shaping and in-homogeneous efficiency due to contrary parametric feedback in the two phase-matching geometries (PVWC / TPG) during an optical parametric amplification process in a nonlinear crystal (e.g. BBO). Figures (a-f) shows both the simplified schemes of the spatiotemporal pulse shapes of pump and signal before and pump, signal and idler after the parametric amplification. The differences are caused by the spatial overlap due to the non-collinear propagation together with the nonlinear cross-talk/cross-seeding of signal and idler pulses within the pump field. Figure (c) and (f) show the propagation directions represented by the wavevectors of signal \vec{k}_s and idler \vec{k}_i pulse with respect to the propagation direction of the extraordinary pump pulse \vec{S}_p .

fication, the time axis shows the retarded time⁶ ($t' = t - z/v_g$). Additionally, the coordinates (x, t) are rotated in order to orthogonalize the spatial coordinate x' and the propagation of the pump pulse \vec{S}_p (the pump will not be displaced in x' after amplification). Respectively, the wavevector of the extraordinary pump pulse \vec{k}_p in the birefringent crystal is rotated by the walk-off angle of -3.3° (Fig. 2.5 (c, f)). It can be seen, that the arrangement of signal and idler wavevectors (\vec{k}_s, \vec{k}_i) in the two non-collinear phase-matched geometries are symmetrically oriented with respect to the wavevector of the pump, since they differ only geometrically due to the angularly invariant ordinary refractive index of the signal and idler pulses.

The important insight in this diagram regarding the PVWC-geometry can be found by considering a slightly larger walk-off angle of the pump compared to the non-collinear angle of the signal pulse in the specific example. As a result, the x' -projection of the signal and idler wavevectors ($\vec{k}_{x',s}, \vec{k}_{x',i}$) are pointing in the same direction. In other words, since the propagation direction and the direction of the

⁶The differences in the group velocities v_g of pump, signal and idler pulses shall be neglected.

wavevector are equal for the ordinary pulses, the same is true for the relative propagation of signal and idler, whereas the propagation direction of the extraordinary pump pulse follows its Poynting vector \vec{S}_p . The consequence is shown in Fig. 2.5 (b), after a sufficient propagation distance the efficiency of the parametric amplification process is almost zero in a large pump pulse area. This is caused since the DFG-process is not seeded in this major part of the pump pulse, neither by the signal nor by the idler pulse, due to the displacement between signal and idler in the same direction. Thus, the overall efficiency is limited by the fact that the walk-off of the pump is bigger than the non-collinear angle of the seed pulse in a PVWC amplification process in BBO. Furthermore, it will become important for the broadness of the phase-matching to keep in mind that especially long-wavelength spectral components of the strongly angular dispersed idler pulse show a rather high non-collinear angle and consequently just a very short effective co-propagation length as it can be seen in Fig. 2.3 and Fig. 2.4.

The situation is quite different in the tangential phase-matching geometry which is considered in the right hand side of Fig. 2.5 (d-f), under the same starting conditions. In the schematic of the involved wavevectors (Fig. 2.5 (f)) it can be seen that in this case, the x' -components of the signal $\vec{k}_{x',s}$ and idler $\vec{k}_{x',i}$ wavevectors are counter-propagating with respect to the propagation direction of the pump pulse \vec{S}_p . This causes a continuous co-seeding of the signal and idler pulses over a theoretically unlimited propagation length. To give an example, if the group delay of all pulses is neglected in the retarded time-window in Fig. 2.5 (f) the signal and idler pulses are counter-propagating relatively to each other along the x -coordinate. Because of the strong non-collinearity of the seed pulses with respect to the pump ("magic angle" + walk-off angle) it quickly leaves the interaction region and even the observation window downwards. In contrast, the idler pulse is generated with a slightly larger non-collinear angle than the given walk-off angles of the pump pulse which results in a slowly upwards propagation. To be more precise, for clarity the generated broadband angularly dispersed idler pulse is not shown in the example. With respect to the pump pulse propagation the non-collinear angles of this idler pulse spanning from slightly negative, for wavelength close the degeneracy up to strongly positive propagation angles for the long-wave idler components.

Consequentially, the long-wave idler components, which are propagating in positive x' -direction acting as a seed for the generation of new short-wave signal components propagating quickly in the negative x' -direction. Before this short-wave signal pulse leaves the pump pulse region it seeds again the counter-propagating long-wave idler pulse. This process continues until the nonlinear crystal ends or the pump pulse

is completely depleted. Additionally, signal and idler components which already left the pump pulse area, cannot be back-converted to the pump pulse, since they are spatially separated on both sides of the pump pulse.

This counter-propagating seeding process can be seen as an analogy to a mirrorless optical parametric oscillator, which is well known for periodically poled crystals [Khu07]. However, in this context the back-coupling of the pulses is restricted to the x' -components of the signal and idler wavevectors in an ultra-broad non-collinear phase-matched amplification process.

In conclusion, the transversal counter-propagation of signal and idler pulses in respect to the propagation of the pump pulse causes a continuous co-seeding of both pulses within the whole pump pulse area. Furthermore, since there is no spatial overlap between signal and idler pulse outside the pump area, their back-conversion to the pump is suppressed. That in principle allows for a total pump depletion for a sufficient crystal length. Moreover, since for the given example the numbers for the walk-off and "magic" angle are given by the dispersion properties of BBO, other nonlinear crystals in principle can show the same back-coupling mechanism for the PVWC-geometry. For example, this is the case for a broadband non-collinear phase-matched BIBO-crystal, showing a larger "magic angle" of 3.9° compared to the walk-off angle of 2.3° .

However, at this point it has to be mentioned again that strong simplifications to the example are made. Here, only the effects of the localization of the signal pulse in the PVWC, as well as, the high conversion efficiency of short-wave signal components in the TPG should be explained. Consequently, no statement about beam quality, the compressibility or the spectral bandwidth of the amplified signal pulses can be pointed out by this example. However, for many applications such questions are even more important than only the goal of the highest conversion efficiency possible. Especially, the origin of spectral and temporal features, which are strongly connected to the compressibility of the ultra-broadband amplified signal pulse is one of the main points which will be discussed in the next section.

2.2.3 Temporal aspects of non-collinear parametric amplification

Together with the mentioned spatial effects, as they were explained by aid of a strongly simplified example in the previous section, an additional important impact is given by the temporal evolution due to linear dispersion, as well as, the nonlinear phase shaping effects. The last one is caused mainly by the nonlinear process itself which can be understood by a cascaded back and forward conversion due to a residual phase-mismatch [Ros02]. Another strong contribution to the pulse evolution

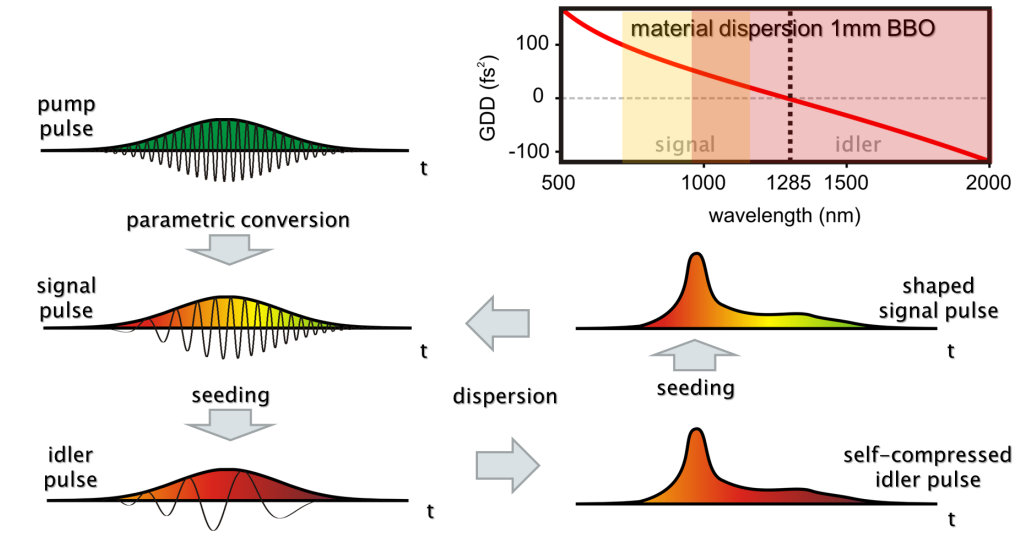


Figure 2.6: Illustration of the inhomogeneous temporal pulse shaping dynamic due to self-compression of the generated negatively chirped idler pulse. In the upper right corner the theoretical GDD-curve of the idler pulse and the positively chirped signal pulse in 1 mm BBO is shown. The high intense self-compressed part of the idler between 1000 nm and 1285 nm acts in a reverse sense as a strong seed for the signal pulse, shaping it in a similar way.

is the strong nonlinear feedback and amplification of intensity modulations due to self-compression effects. These intensity modulations can be caused by the linear dispersion properties of the crystal or by parasitic cascaded effects for different spectral components in the signal and idler pulse. Accordingly, the nonlinear feedback and the amplification of temporal intensity peaks, e.g. due to self-compression of spectral components, strongly depends on the present spatiotemporal intensity distribution in all involved pulses. Since the parametric phase also strongly depends on the strength of this parametric coupling, nonlinear self-compression effects induced by spectral and temporal intensity inhomogeneities can be amplified and transferred between the pulses due to the nonlinear conversion process.

Figure 2.6 shows a typical sequence of the temporal evolution during a parametric amplification which is strongly influenced by the idler self-compression. The example considers the broadband signal amplification in a BBO crystal pumped by a narrowband green pulse. The left side of the figure illustrates the envelope and the oscillating electric field of the involved pump, signal and generated idler pulses, in time. During the propagation the positively chirped signal pulse will accumulate more and more positive dispersion leading to a stretching in time, as indicated by the dispersion curve of the BBO in the upper right corner of the figure. Meanwhile,

the parametric difference frequency generation process creates, together with the amplification of the signal, an idler pulse with a similar envelope. The chirp of this idler pulse, however, is inversely related to the chirp of the signal pulse since the leading part of the pulses contains the frequency components close to the degeneracy, whereas the trailing part covers the highest signal frequency components and the lowest corresponding idler frequencies. It is easy to see that with respect to the dispersion curve in BBO, the generated negatively chirped leading part of the idler is compressed by the positive dispersion of the BBO before the zero-dispersion point around $1.3\ \mu\text{m}$. However, the compression gets weaker close to the zero-dispersion point and even turns into a pulse stretching for the long-wavelength trailing part of the idler pulse. Finally, the dispersively shaped idler pulse seeds and enhances the parametric amplification process of the signal pulse proportional to the temporal idler intensity. This coupling matches the temporal and spectral intensity distribution of the signal pulse to the rather complicated pulse shape of the idler.

In conclusion, it can be said that the resulting pulse shapes and efficiencies as well as the spatiotemporal intensity and phase inhomogeneities are mainly caused by three effects: the non-collinear propagation, causing a strong signal localization in the PVWC and a co-seeding and spatial signal stretching in the TPG; the induced nonlinear (parasitic) phase, leading to intensity modulations; and the self-compression of the idler, causing a strong inhomogeneous spectral efficiency distribution. All these effects are additionally strongly nonlinear coupled to each other. Consequently, the question which phase-matching geometry, PVWC or TPG and which crystal should be preferred for a certain set of parameters, e.g. pump and seed pulse energy or required phase-matching bandwidth, compressibility and beam quality, can not be answered analytically. However, if all participating nonlinear spatiotemporal and parasitic effects are considered with their quantitative impacts, a deeper understanding and a quantitative prediction of any 2nd order parametric amplification processes could be given. To provide a computational tool which opens this possibility, the (2+1) dimensional model has been developed which will be introduced in the next section.

2.3 Simulation of ultrashort-pulses optical parametric interaction

It was already mentioned in Sec. 2.1.2, that the numerical treatment of second-order nonlinear interactions, especially for parametric difference frequency generation, is typically based on split-step Fourier methods solving the three coupled nonlinear

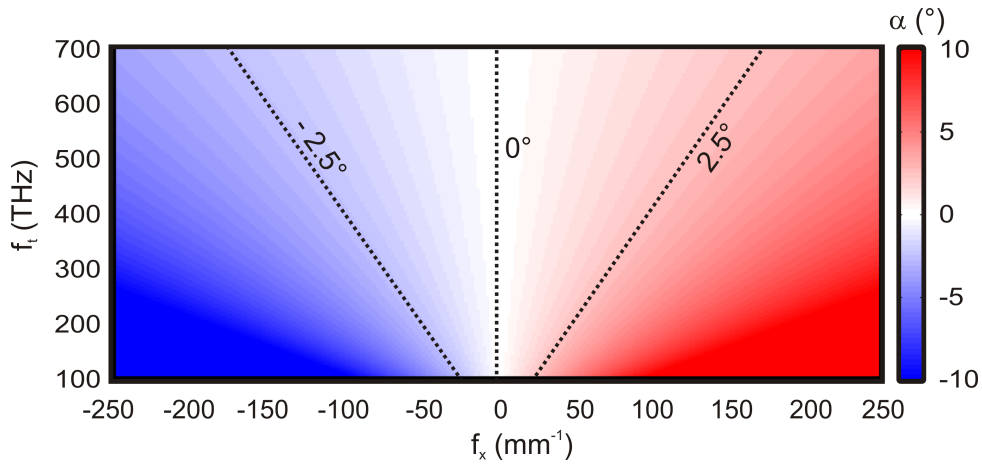


Figure 2.7: Mapping of the propagation angle α with respect to the spatial frequency f_x and optical frequency f_t for the ordinary polarization in BBO with a phase-matching angle θ of 24.5° between the optical axis and the main propagation direction along z at $\alpha = 0^\circ$.

differential equations Eq.(2.7) [Con10]. Each equation describes the change for pump, signal and idler wave separately. Hence, each phase-matched nonlinear process beyond the considered difference mixing needs to be implemented individually by adding differential equations for each additional nonlinear interaction process responsible for a specific mixing product [Bro11]. Especially for new phase-matching concepts and new nonlinear crystals the relevance of a specific phase-matched mixing-process is difficult to forecast. Furthermore, the processing of the split-step algorithm for all three spatial dimensions and the time is a huge computational effort [Ari97].

2.3.1 (2+1) dimensional Fourier split-step algorithms

In contrast to these works, as mentioned above, the (2+1) dimensional split-step algorithm developed in this work is based on only two spatial dimensions [Lan13]. As it will be shown in the following, the model implements all possible second-order nonlinear interaction processes of ultrashort light pulses in a birefringent crystal with the two coupled differential equations (Eq.(2.8) for the ordinary $E_o(t, x)$ and the extraordinary $E_e(t, x)$ electric fields. As explained in Sec. 2.1.2 the equations can be restricted to one spatial transverse dimension in the principal plane which is defined by the non-collinear propagation of all involved pulses. This transversal dimension is orthogonal to the main propagation direction towards the z -coordinate, whereas the angle between this coordinate and the optical axis is chosen to fulfill

required phase-matching conditions in the respective nonlinear crystal. At the same plane the dispersive and diffractive evolution of the pulses are taken into account by Eq. (2.1) and Eq. (2.2) in the spectral domain with the optical and the spatial frequency spectrum revealed by the Fourier transformation of the two orthogonally polarized optical fields $E_{o/e}(f_t, f_x) = \mathcal{F}(E_{o/e}(t, x))$. Figure 2.7 shows the dependency of the propagation angle with respect to the spatial and the optical frequencies. The example illustrates the distribution of propagation angles as it can be calculated by Eq. (2.6), for ordinary polarized spectral components in BBO under broadband phase-matching conditions. With help of this connection the quite counterintuitive spatiotemporal frequency space representation of the optical fields, as shown in Fig. 2.8, can be mapped to an angular distribution of all involved spectral components. Fig. 2.8 shows the computational electric field arrays as they are processed in the numerical model. The pump pulse in the example is well defined at optical frequency of 583 THz and propagates exactly along the z -axis. Consequently, as shown in Fig. 2.8 (a), the spectrum of the pump pulses in the frequency domain is quite narrowband in both, the optical and the spatial frequencies. However, the spatial and optical frequency range for this extraordinary field have to be set wide enough to cover all possible mixing products that can be generated in extraordinary field as shown in the following. In Fig. 2.8 (b) the seed pulse - as typically provided by an ultra-broadband Ti:Sapphire oscillator [Kae01] - is implemented in a way that all spectral components are propagating in the same direction under the magic angle of 2.5° to the propagation direction of the pump.

For the starting conditions of the simulation of an e.g. DFG-process of an extraordinary pump and an ordinary signal pulse, two corresponding computational field arrays are defined. Also the refractive indices $n_{o,e}(f_x, f_t)$ of two orthogonal polarizations as well as the strength of the nonlinear interaction $\kappa_{o,e}(f_x, f_t)$ and the transmission $T(f_t)$ of the crystal are set in at the beginning of the split-step algorithm as illustrated in Fig. 2.9. In addition to the well defined optical field arrays which contain the pump and the seed pulses, a noise field array with a certain amplitude (typically one photon per frequency interval and a random phase distribution) can be added to supersede the quantum noise, which is not quantum mechanically included in the simulation. For the propagation the nonlinear crystal is divided in small steps in order to reach a sufficient accuracy of the explicit Euler method. Within a loop, the current optical field arrays in the spectral domain are then transformed by a 2D-FFT to the spatiotemporal domain in order to perform the nonlinear interaction procedure. The results of the coupled equations Eq. (2.8), namely the change in the complex electric fields due to the nonlinear interaction $\partial E_{o,e}(t, x)$, are

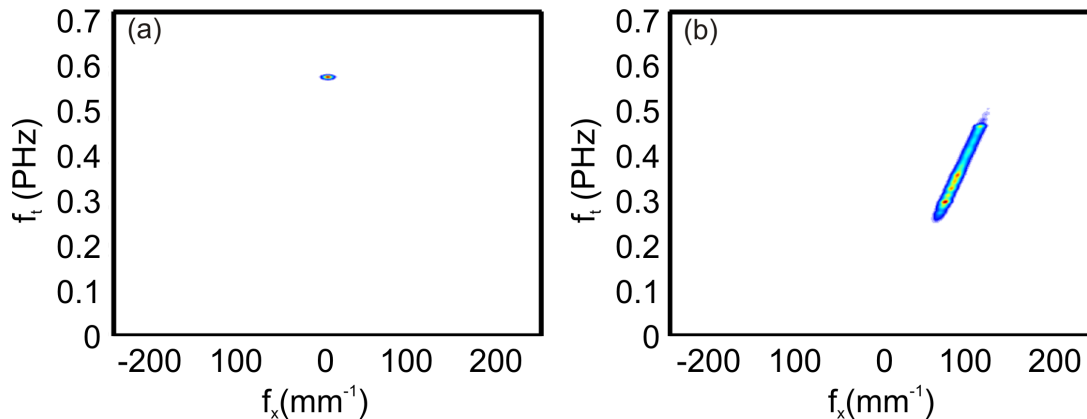


Figure 2.8: Typical input computational field arrays for the (2+1)D simulation of the broadband parametric amplification in BBO: (a) $|E_e(f_t, f_x)|^2$ is the spectral intensity distribution of the extraordinary complex optical field array containing the green pump pulse and (b) $|E_o(f_t, f_x)|^2$ the ordinary complex field array with the ultra-broadband seed pulse, whereas all spectral components propagate under the same angle of 2.5° to the pump pulse.

transformed back by an inverse 2D-iFFT to represent the change of the complex optical fields in the spectral domain. Before adding these spectral differential ordinary and extraordinary complex optical fields to the field arrays from the previous loop, $\partial E_{o,e}(f_t, f_x)$ is multiplied by the nonlinear interaction parameter $\kappa_{o,e}(f_x, f_t)$ in order to represent the strength of the nonlinear process Eq. (2.9). Finally, the propagation equation Eq. (2.1) is applied to the new spectral fields to perform the next propagation step in z -direction and continue with the following loop.

At each position along the propagation in the crystal, the data analysis allows to monitor all essential parameters, such as the pulse energy, pulse duration, the pulse width, etc. as well as the evolution of the spectrum and phase as it can be measured in the experiment. As will be explained in the following sections, especially data which it is not easily accessible in the experiment can now be analyzed carefully and is very valuable in gaining new insights on the process.

One of the most important benefits of the novel (2+1) model developed in this work, is the moderate computing time on a standard desktop computer. This is possible without substantial loss of accuracy due to the neglect of the third rather unimportant spatial dimension. In fact, to compute the example presented in the next section takes less than 15 seconds. Thereby the model handles the four complex computational field arrays ($E_{o,e}(x, t)$, $E_{o,e}(f_x, f_t)$) with a resolution of 2048×1024 , for 500 steps in 5 mm BBO on a low cost GPU (NVIDIA GeForce GTX 680).

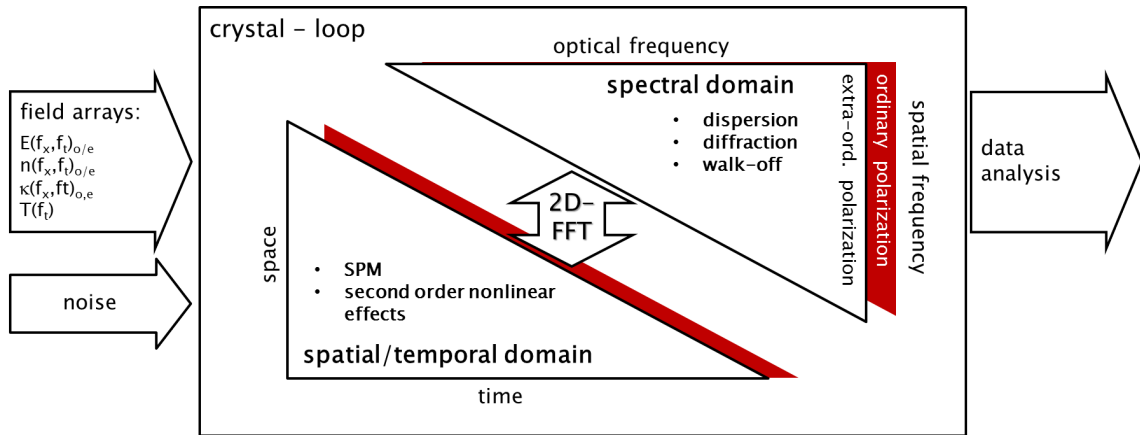


Figure 2.9: Principle of the split-step simulation model depicts the complex electric fields of the two Fourier-domains together with their corresponding mathematical operations for propagation and nonlinear interaction.

This enables for extensive parameter scans with precise predictions of the performance which allows for an optimization of system parameters, e.g. spot sizes, lengths and crystals, right from the planning phase of an OPA system. Beam profiles, the compressibility of the amplified pulses, the peak intensities, as well as a good estimation of the expected pulse energy can now be evaluated in dependence of e.g. pump and seed focus, crystal length or the chosen geometry, etc.

Implementation of the self phase modulation

As the comparison to experimental observation is one of the important objectives of this work, in addition to the second-order nonlinear interaction processes which are fully included in the model, as discussed in the previous sections, the self phase modulation (SPM) [Agr00] is implemented as well. This becomes especially important for parametric amplifiers with very high intensities applied to the crystal, but also for optical parametric oscillators in which all nonlinear phase contributions are accumulated over several round trips. Thus within each simulation loop the corresponding additional nonlinear phase for a step dz ,

$$\phi_{\text{SPM}}(x, t) = \frac{2\pi f_t}{c} n_2 I(x, t) dz, \quad (2.13)$$

depends on the optical frequency f_t and on the nonlinear refractive index n_2 which is assumed to be constant for a certain nonlinear crystal (e.g. $\sim 4 \times 10^{-20} \frac{\text{m}^2}{\text{W}}$ for BBO). Obviously, it also depends on the intensity distribution in time and space, $I(x, t) =$

$2\varepsilon_0 c n(f_x, f_t) |E(x, t)|^2$, whereas the first-order refractive index in the equation is a function of the optical and spatial frequencies.

In order to implement this intensity dependent phase in the Fourier split-step algorithm, the derivation of the complex optical field with the additional nonlinear phase, $E(x, t) \exp(-i\phi_{\text{SPM}})$, over a propagation step dz is given by $\frac{\partial E(x, t)}{\partial z} = -i\phi_{\text{SPM}} E(x, t)$. The spatial and optical frequency dependent variables and the constants can now be combined to a variable $\kappa_{\text{SPM}}(f_x, f_t) = 2\pi\varepsilon_0 n_2 n(f_x, f_t) f_t$ which can be taken into account in the spectral domain and the term $|E(x, t)|^2$ and the complex electric field distribution need to be handled in the spatiotemporal domain. In conclusion the implementation of the SPM is realized by adding only one additional computational step in the split-step algorithm:

$$E(f_x, f_t, z + dz) = E(f_x, f_t, z) + \kappa_{\text{SPM}}(f_x, f_t) \mathcal{F} (i |E(x, t)|^2 dz E(x, t)). \quad (2.14)$$

Thus, in combination with the propagation algorithm in the model, this equation includes also the spatial and temporal Kerr effect as well as the self-steepening of all involved pulses [Agr00, DeM67]. In particular, the implementation of the self-focusing helps to identify the onset of a filamentation process and to estimate the upper limit peak intensity of the driving pulse in order to avoid - besides the linear and nonlinear absorption - a damage of the crystal.

The defocusing effect that takes place for intensities high enough to generate free electrons, which prevents such a filament to have a non-physical spatial collapse, is not implemented in the model. Although the treatment of this plasma effect could be handled with few additional computational steps, which take care of the intensity and time dependent free-charge and recombination rate, resulting in the defocusing phase contribution [Cou02], no quantitative results can be expected within this model. This is caused by Rayleigh-restrictions of the (2+1) dimensional algorithm due to the two-dimensional energy distribution and the corresponding linear connection between beam width and peak intensity which would lead to an underrated clamping peak power. However, this non-parametric filamentation process shows a very sharp threshold behaviour. Thus, since the parametric interaction processes should always stay below this threshold to avoid for a damage of the nonlinear crystals, this restriction does not matter for the investigations which are scope of this work.

2.3.2 Interpretation of simulation data

As shown in the previous sections, the (2+1)D simulation enables a careful analysis of the interplay between temporal, spatial, and cascaded effects and their impact on the nonlinear parametric conversion of ultrashort pulses. Since the model includes all possible mixing products in the two coupled equations it is very crucial to understand the underlying physics for the identification of the individual process leading to a certain feature. Therefore, specific processes can be separated by identifying the corresponding "quantum" path as illustrated in Fig. 2.2, which can be done by suppressing all other paths and their regarding summands in Eq. (2.8).

Furthermore, in order to be able to compare simulated and experimental data, the two orthogonal optical fields $E_o(f_x, f_t)$ and $E_e(f_x, f_t)$, containing all the data from the simulation, are separated again into the particular pulses as they can be measured in the experiment. The separation of the respective, pump, signal and idler pulses, as well as all their mixing products (e.g. SFG, SHG, DFG), can be done either by their polarization, the optical spectrum, or by the spatial frequency which can also be expressed as the direction of propagation. To explain this concept, in the following the different illustrations and representation of the obtained simulation results will be explained at the example of a non-collinear parametric amplification process.

An illustrative way of interpreting the data can be obtained by plotting the optical fields in the Fourier domain against the optical frequency axis and the relative propagation angle calculated by Eq. (2.6) as shown in Fig. 2.10 (a). The figure maps both the ordinary and the extraordinary simulated spectral data from a typical non-collinear amplification process in the PVWC-geometry in 5 mm BBO. The crystal is pumped by a strong, extraordinary polarized 500 fs-pulse at 515 nm and seeded by an ordinary broadband signal pulse in the "magic" non-collinear angle of 2.5°.

Considering the underlying physical concepts, e.g. phase-matching, conservation of energy, etc., as described in the previous sections, each spectral and angularly resolved spectral feature can be attributed to their corresponding pulses as they are observed in the experiment.

In the example, the broadband phase-matching condition is fulfilled by setting the main propagation direction z and the propagation direction of the pump ($\alpha = 0^\circ$) under the phase-matching angle of 24.35° to the optical axis of the crystal. The phase-matched frequency components with respect to the propagation direction can be also calculated analytically from the simple non-collinear phase-matching picture (see section. 2.2.1). The result of the DFG-process, for the chosen crystal orientation, pump direction and wavelength, is indicated by the black double curves in

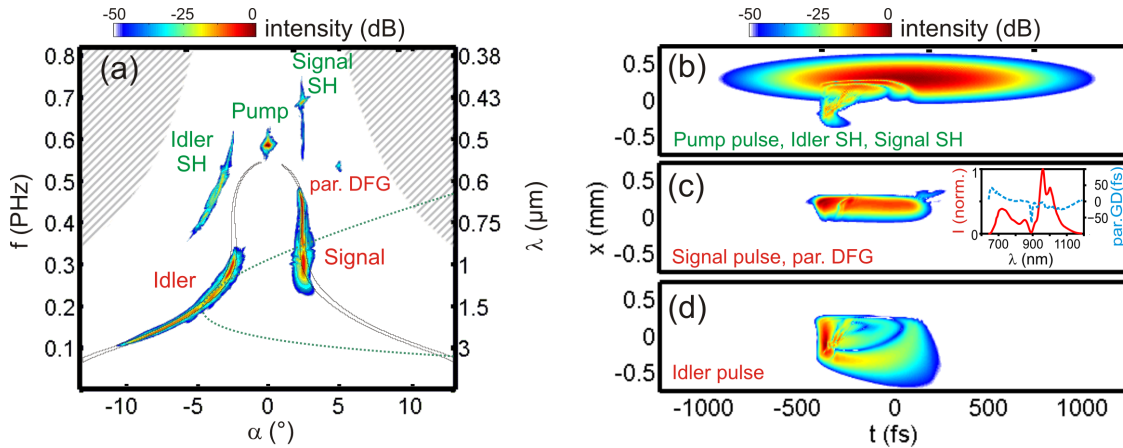


Figure 2.10: Left: Simulation data from both, the ordinary field with idler, signal and parasitic DFG, and the extraordinary field with pump, idler-SH, and signal-SH normalized to the maximum ordinary peak intensity. Phase matching is indicated by the DFG (black double) and collinear SH phase matching curve (green dotted). The graphic representation with respect to a propagation angle instead of a spatial frequency leads to non-rectangular borders of the window indicated by the shaded area. **Right:** Normalized intensity in time and space of: (b) pump pulse together with signal-SH and idler-SH, (c) signal pulse with the power spectrum and parametric group delay in the inset and (d) angularly dispersed idler pulse.

Fig. 2.10 (a). The green dotted curve represents the phase-matching for the SHG in general.

The results from the numerical simulation of the example can be separated in ordinary (red labeled) and extraordinary (green labeled) features. It can be seen, that the amplified signal spectral components at 2.5° and the strongly angularly chirped idler components at negative angles agree perfectly with the analytically calculated DFG-phase-matching curve. Also the signal and idler second harmonic generation fits to the analytically calculated SHG-phase-matching curve. Since the efficiency of the DFG-process is very sensitive to the phase relations between the pulses, this exact agreement, even for parts of the idler which are propagating at very large angles, give strong evidence about the appropriateness of the approximations⁷ that have been made in the numerical model. Furthermore, beside these obvious identifiable spectral components, also other non-obvious phase-matched mixing products, e.g. the difference frequency generation (DFG) signal at $550\text{ nm}/5^\circ$ which is pumped by the parasitic signal-SH and seeded by the idler wave at negative angles, can be addressed in this angularly resolved spectral representation.

⁷The propagation equation used in the model is based on the paraxial and slowly varying envelope approximation.

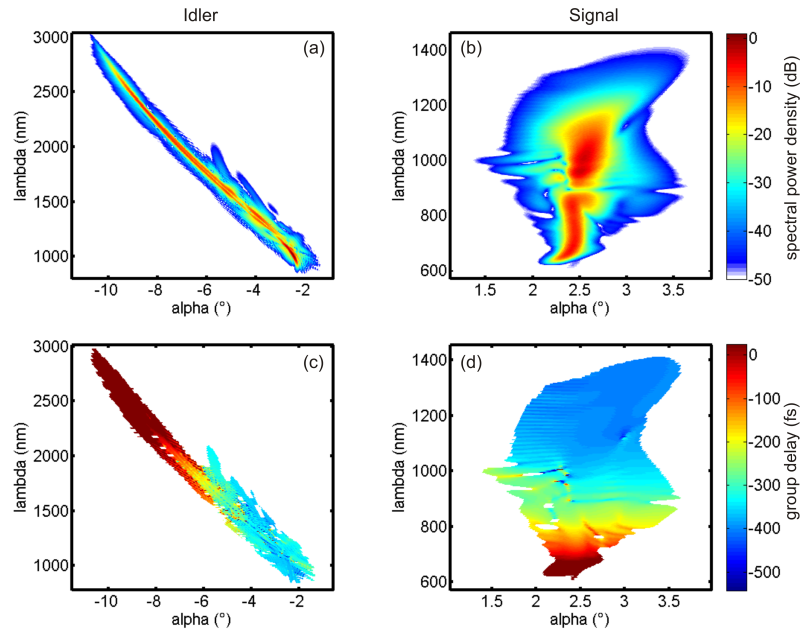


Figure 2.11: Spectrally and angularly resolved timing map for the optical parametric amplification in a Poynting vector walk-off compensation geometry (PVWC). The upper part shows the corresponding power spectrum.

The identified sections in the spectral domain can now be extracted and transformed back to the spatiotemporal domain, in order to obtain the pulse profiles of the pump, signal and idler in time and space separated from each other⁸. Fig. 2.10 (b) shows the back-transformed spatiotemporal representation of the pump pulse and the second harmonic of signal and idler in the extraordinary spectral field. The particular back transformation of the ordinary field is done for positive and negative angles separately. Fig. 2.10 shows the corresponding signal pulse together with the parasitic DFG in (c) and the angularly dispersed idler pulse in (d). This representation of the simulation results is ideally suited to show the spatiotemporal effects of the process, e.g. the stronger amplification in the leading part of the signal pulse caused by the respective self-compression of idler, as explained in detail in Sec. 2.2.3, which can be seen clearly for the signal and idler components for times around -400 fs. Besides the spatially stretched angular dispersed idler, also the strong spatial localization of the signal pulse in the PVWC-geometry, as explained in Sec. 2.2.2, can be observed in the spatiotemporal beam profile. Thereby, the separation of the involved pulses can also be done for a specific spectral and angular range. For example, in such a way the second harmonic of the signal pulse could

⁸Actually, all pulses are overlapping in time and space at the crystal-output surface. However, they can be separated by their particular polarization, propagation direction and spectrum.

be shown isolated from the pump pulse. In Fig. 2.10 (a) this signal-SH is not visible since it is completely superimposed by the stronger pump pulse⁹.

As the two described representations are showing either the spatial and temporal or the angular and spectral effects together they can not be directly connected. For example it is hard to see that the high power densities of the signal in the spectral domain at 2.5° and $1\ \mu\text{m}$ (also shown by the red curve in the inset in Fig. 2.10 (c)), correspond to the compressed leading part of the signal pulse around $-400\ \text{fs}^2$ in the spatiotemporal domain (shown also in (c)). Therefore a third representation is introduced as shown in Fig. 2.11. The figure compares the angularly and spectrally resolved intensity distributions of the idler (a) and signal pulses (b) to the relative timing of the spectral and angular components to each other (c-d). In this representation it can clearly be seen, that e.g. the short-wave signal spectral components are strongly positively chirped, whereas the nearly constant group delay for spectral components close the degeneracy indicates a compression of corresponding components in time. The same can be observed for the negatively chirped idler pulse. Additionally, it can be seen that for signal wavelengths and angles which are phase-matched to be frequency doubled around $860\ \text{nm}$ (see Sec.2.2.1), the timing of the particular spectral components is not independent of the respective propagation direction anymore. In the experiment this can be observed as a spatial chirp in the far field and a poor beam profile and M^2 -value for the corresponding wavelengths.

It needs to be pointed out, that the conclusions that have been made are very specific for the chosen example and strongly depend on the initial beam parameters, e.g. the beam width, the pulse duration, and the chosen phase-matching geometry. In fact, the introduced simulation allows for a quantitative evaluation of possible geometry and beam parameters which are ideally suited for a particular experimental requirement. In the following chapter this questions will be examined more closely by comparing the results from several in-house experiments - covering a large range of initial parameters - to the simulation of different ultra-broadband parametric amplification setups.

⁹In contrast to the signal-SH, the second harmonic of the self-compressed idler pulse can be seen clearly at negative x -values. Also the circular structures in the pump pulse, caused by the cascaded back and forward conversation, can be seen clearly in Fig. 2.10 (a).

Chapter 3

Temporal and spatial effects in ultra-broadband parametric amplifiers

In recent years, the limits in terms of peak power and pulse duration concerning the generation of ultrashort pulses with high repetition rates have been pushed dramatically, especially driven by the development of chirped pulse optical parametric amplifiers (OPCPAs). In particular, due to the ongoing progress in novel high power pump sources, e.g. thin-disk based regenerative amplifiers [Sch10] or rod-type fiber amplifiers [Rot10], OPCPA-systems delivering pulses with peak powers up to the GW-regime and MHz-repetition rates have been demonstrated [Rot12]. The enormous peak power, the high repetition rates and the pulse durations in the range of only few optical cycles - an unique combination which can be exclusively reached by OPCPAs - are becoming increasingly popular for a variety of applications, e.g. high harmonic generation with high photon flux, generation of attosecond pulses, and nonlinear spectroscopy.

The importance of this field of research, mainly pushed by the demand of the mentioned laser pulses, can also be attributed in the numbers of related scientific publications in the recent year. However, there are various open questions about the quite remarkable effects and unexpected results observed in experiments, which are not completely understood yet.

The scope of this work is to gain the understanding of the rich and complex spatiotemporal dynamics and to answer open question concerning experimental observations in parametric amplification processes. An ideal tool to reach this goal is the novel (2+1) dimensional numerical simulation model which has been developed in this work and is introduced in detail in the previous chapter.

Therefore, in this chapter, a wide range of ultrashort pulse OPCPAs will be carefully studied to clarify the mentioned effects and features observed in several in-house experiments. This can be done by the conclusion and insights which rise from the

comparison of the results from the numerical simulation with the observations and measurements in the experiments. Thereby, the conclusions will help for a reliable verification of the simulation model, which opens the possibility to predict the behaviour of the parametric amplification process in a huge parameter space. Together with a intuitive illustration of results which are hard to access in the experiment, new ideas and novel experiments have grown, e.g. the sub-sequential pump-depletion in a multi-pass OPCPA-system or the cw-seeding of narrowband OPAs for the generation of high energy fs-pulses in the mid-infrared spectral region, the nonlinear cavity dumping of parametric oscillators and high power laser systems, etc.

In the following three sections, by means of the simulation model, several multi-stage OPCPA are investigated. Finally, in the next chapter, the expertise generated by the investigation of all those systems will be the basis to understand the quite complicated processes in a broadband phase-matched non-collinear optical parametric oscillators which are scope of the second part of this work.

3.1 Double stage high power OPCPA-system

In this section, a state-of-the-art OPCPA-system will be analyzed, which was developed in a cooperation between the VENTEON GmbH, the Department of Physics of Lund University together with the theoretically investigations done by LUH, which are also shown in this work [Mat13].

The specifications of the system were determined according to the goal of the efficient high harmonic generation from the CEP-stabilized few-cycle pulses provided by a compact and reliable double-stage OPCPA operating at high repetition rates. Thereby, by means of the simulation model important information regarding the design of the OPCPA-system could be evaluated. Notwithstanding, that the quantitative comparison to the experimental results, shown in the next section, confirmed the given predictions. Furthermore, quite remarkable observations that have been made in the experiment could be also reproduced and explained by an extensive parameter scan in the simulation which will be discussed in in Sec.3.1.2.

3.1.1 Experimental verification of the numerical model

Experimental Setup

Fig. 3.1 shows the schematic setup of the OPCPA-system. The front-end of the system is based on an ultra-broadband commercial Ti:sapphire oscillator (VENTEON | PULSE: ONE OPCPA SEED) with a repetition rate of 80 MHz and 2.5 nJ of pulse

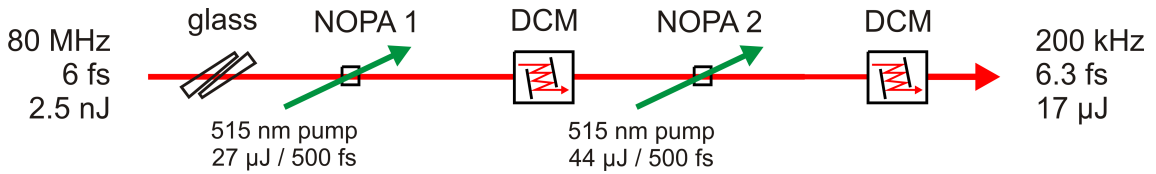


Figure 3.1: Schematic setup of the double stage OPCPA-system [Mat13]: Pump: optically synchronized and frequency doubled rod-type amplifier system; Seed: octave spanning commercial Ti:sapphire oscillator (VENTEON | PULSE: ONE OPCPA SEED); NOPA: non-collinear optical parametric amplifier stage; DCM: double-chirped mirror pairs for pulse compression

energy. The primary spectral output of the oscillator supports sub 6 fs pulses which are used to seed the first stage of the OPCPA-system. Because of the large spectral bandwidth of the oscillator, the spectral power density at the infrared edge of the output spectrum at 1030 nm is sufficient to be fiber-coupled to seed a fiber amplifier system. The two frequency doubled outputs of this fiber amplifier system at 515 nm with pulse energies of 27 μJ and 44 μJ and pulse durations about 500 fs [Mat13], are ideally suited to pump the two OPCPA-stages. Except for slow thermal drifts in the different optical paths, these pump and seed pulses are intrinsically optically synchronized since the fiber amplifier and the OPCPA are seeded from the same laser source.

As shown in Fig.3.1 for the first amplification stage, the 6 fs seed pulses are stretched by the optical path in air, the glass wedges and in the first BBO-crystal to 400 fs in order to get a sufficient temporal overlap with the 500 fs pump pulses. The parametric amplification then takes place under the relative angle of about 2.43° between pump and signal beams in the 5 mm BBO crystal and the PVWC-geometry. The crystal is cut and oriented to fulfill the non-collinear broadband phase-matching condition - as it is explained in detail in Sec.2.2.1. Furthermore, the 27 μJ pulses pumping the first stage are focused to a diameter of 350 μm ($1/e^2$) resulting in a peak intensity of about 110 GW/cm^2 in the crystal. According to the beforehand performed numerical simulations it turned out that the parametric amplification process - especially in the case of a large enhancement factor - is not sensitive to the beam diameter of the seed beam. This will also be explained later in Sec.3.3. Accordingly, the waist of the seed in the experiment, with diameters of about 110 μm , was chosen to be slightly smaller than the pump focus. In the next step, the preamplified pulses were slightly recompressed from about 420 fs to 270 fs by double-chirped mirrors and refocused into the second amplification stage. This stage, operating under the same phase-matching conditions as explained before,

was pumped by 44 μJ and 500 fs-pulses. The pump beam was focused to 540 μm which results in a slightly smaller peak intensity of 75 GW/cm^2 in the second 5 mm BBO. Finally, the amplified signal pulses after the two amplification stages, are recompressed by 12 reflections on doubled chirped mirror pairs.

Quantitative comparison of experimental and simulated results

It was mentioned that for a first approximation of the appropriate parameters of the planed OPCPA-system e.g. the beam waist of the seed and pump, the system was modeled by means of the (2+1)D simulation. Since after the experimental realization of the system by Matyschok *et al.* [Mat13] well defined experimental data are available, the system is ideally suited for a verification of the simulation model. In the following, the results from the simulated system are compared quantitatively to the experimental results from the first and the second stage of the realized OPCPA-system. Therefore, the start parameters for the numerical calculations were carefully chosen to match the experimental conditions as close as possible. In particular, the phase-matching angle of 24.35° in the experiment can be found quite accurately by analyzing the spectral localization of parasitic SHG in the measured signal spectrum.

The shapes of the measured and the simulated spectra of the amplified signal after the first and the second amplification stages are compared in Fig. 3.2 (a). The quite remarkable agreement between measured (red shaded - first stage / grey shaded - second stage) and the simulated (respectively light-blue / blue) amplified spectra is achieved by simply choosing the right pump-seed pulse overlap in time¹ without any further fitting parameter. This excellent agreement even for the second stage is especially notable, since the simulated output of the first stage is used for seeding the second stage. Therefore, this seed pulse is recompressed by adding a negative dispersion, which is modeled to be similar to the dispersion of the double-chirped mirrors between the two stages in the experiment.

For the extraction of the signal pulse energy from the two dimensional electric field distribution, as it is calculated by the (2+1)D simulation, the beam waist in the third unconsidered dimension has to be considered. However, since the non-collinear propagation and walk-off effects in this unconsidered dimension are negligible, this beam waist can be assumed to be similar to the one of the pump pulse in the case of a strong pump depletion. By doing so, the output-energy-slopes of both amplification stages are shown by the blue unfilled circles on the right hand side

¹As it will be shown later in Sec. 3.1.2, the simulation also reproduces very accurately the change in the amplified spectrum by scanning the pump-seed pulse delay.

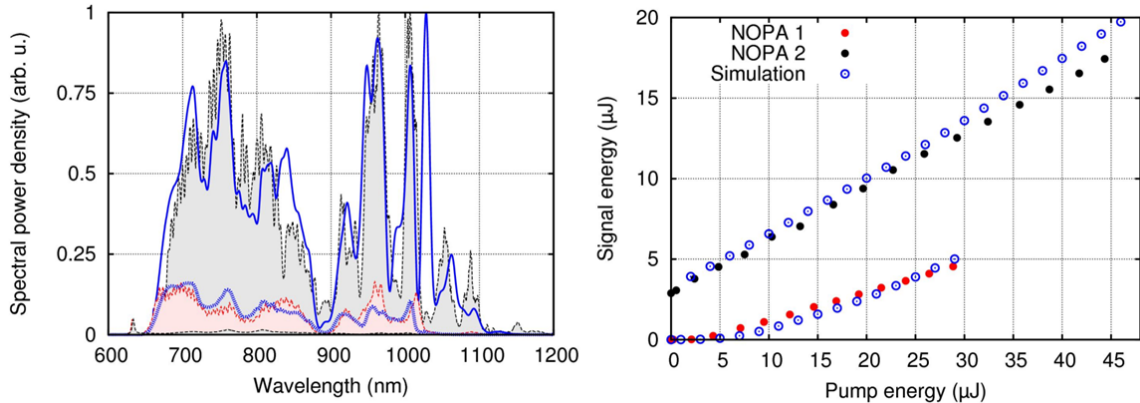


Figure 3.2: Comparison of simulated and experimental results of the double stage high power OPCPA. **Left:** Measured spectra of the amplified signal pulse after the first stage (red shaded) and for the further amplified signal pulse after the second stage (grey shaded); calculated spectra from the numerical simulation (blue lines), respectively. **Right:** Measured and simulated pulse energies after the first and the second stage [Mat13].

in Fig. 3.2. The respective measurements of the output-energy-slopes from the first (red dots) and the second stage (black dots) are in a very good agreement with the numerical results.

This example demonstrates that the (2+1) dimensional algorithm enables quite remarkable quantitative predictions for multi-stage OPCPA-systems with strong spatial, temporal and parasitic effects. As demonstrated for both highly efficient sub-sequential amplification stages, the rather complicated spectral power distributions can be calculated almost exactly considering the uncertainties in the experimental data. In addition to the obvious impact of the parasitic SHG of the signal, the modulation in the signal spectrum caused by the idler SHG and the cascaded nonlinear contributions themselves are quantitatively included. Besides these experimental validations of the approximations which are made in the model (see Sec. 2.1.1) and the fact that all essential physical effects are included correctly, the simulation enables a quantitative statement about the efficiency of the parametric amplification process. Moreover, a good approximation of the pulse energies can be given, since the behaviour in the spatial dimension unconsidered by the model is quite predictable. In other words, in the unconsidered dimension the beam profile can be assumed to be symmetric, whereas the complicated spatial evolution due to the walk-off and non-collinear propagation only takes place in the spatial dimension which is fully included in the model. Depending on the efficiency of the processes the beam diam-

eter of the amplified signal pulse in this unconsidered dimension will either be $\sqrt{2}$ smaller than the pump pulse in case of negligible pump depletion, or similar to the pump in case of strong pump depletion.

Consequently, the exclusion of one dimension, drastically reduces the required computing power which enables extensive parameter scans without a loss of the accuracy. This opens the possibility of finding the optimum experimental conditions for specific requirements on the OPA-system by utilizing extensive parameter scans with the (2+1)D simulation. Furthermore, experimental observations in high power OPCPA-systems, such as additional mixing products and unexpected spectral features which are strongly dependent on one or more parameters, can be systematically investigated, which is shown in the next section.

3.1.2 Fundamental properties and phase relations of cascaded mixing products in high power OPCPAs

As it can be already seen in the example of the first stage of the OPCPA-system above, the parametric gain in such an OPA stage can be extremely high with a single pass amplification of several thousands. Therefore a variety of nonlinear mixing processes can take place during the nonlinear interaction between pump, signal and idler pulses. Whereas some of these mixing products are already documented since they are obvious in the superfluorescence cone of such high power OPCPAs, their origin and fundamental properties are often unknown. Furthermore, a very specific "finger-print-like" change of the generated mixing products is induced by a change of the temporal overlap between pump and seed pulses. This already insinuates, that all these features originate from complicated cascaded DFG and SFG-mixing processes initially starting from the interaction between pump and signal pulses or the superfluorescence. Besides the fact that the most prominent of these processes, e.g. the signal and idler SHG, can influence the efficiency and the dynamics of the amplification process, some of these mixing products carry very interesting additional information about the process and the involved pulses. For example, the mentioned specific change in the spectral and angular characteristics of the cascaded mixing products ("finger-print") could be used for a stabilization of the system. Moreover, some of these mixing-signals could give rise to the phase of the signal pulse which will be explained later.

However, in order to make use of these additional information, the origin and the properties of these mixing processes have to be well understood. Since the simulation includes all possible 2nd order effects, all these mixing products are automatically in-

cluded in the simulation, as it was presented in the previous section. In the following the experimental observations of the dependency of the angularly and spectrally resolved mixing products in the OPCPA will be compared to the simulation results of this first stage for different pump-seed delays. Whereas the relative delay introduced by changing one optical path in the experiment can be measured very precisely, the absolute delay between pump and seed pulses is not easily accessible. Therefore, all measured relative time delays between pump and seed pulses are fitted to the absolute time delay between the two pulses defined in the simulation.

In Fig. 3.3 (c) a series of photographs is presented, showing the visible output of the first stage of the OPCPA-system by varying the temporal overlap between seed pulses from the Ti:sapphire oscillator and the high power pump pulses from the amplifier system [Mat12]. For example the first photograph at the bottom of Fig. 3.3 (c) shows a section of the unseeded superfluorescence cone for a time delay where pump and seed pulses are not overlapping. Since the green pump pulse would saturate the picture, it is eliminated by passing through a hole in the middle of the screen. The non-amplified broadband seed pulse and its parasitic second harmonic (SH), however, is clearly visible by the white overexposed spot on the right hand side of the photograph. Also the strong superfluorescence on the left hand side of the photograph can be clearly seen as an orange stripe. The strength of this signal and the obvious unbalance for positive and negative angles are already discussed in Sec. 2.2.2².

However, by following the series of photographs from negative to positive delays, beside the inset of the parametric amplification of the signal, also the generation of a strong idler pulse is indicated by the eye-catching idler-SH spanning from green to red spectral components at negative angles. The orange superfluorescence, however, vanishes for delay times of about 300 fs corresponding to the most efficient signal amplification. Besides this obvious and well known signals also additional quite unclear mixing products can be observed for certain time delays. The origin of some of these mixing products can be understood by analyzing the possible phase-matching conditions for each observed feature individually. However, the parameter space which needs to be scanned is quite large since all possible parametric mixing processes have to be considered separately for each observed feature. Furthermore, some of the generated signals can have an additional continuous parametric phase con-

²Not going into details about this effect, it should be just kept in mind that long-wave idler components, which are phase-matched at propagation directions larger than the pump-walk-off, co-seeding very efficiently the corresponding short-wave signal spectral components. In case of the efficiently amplified vacuum noise floor this effect is visible by the strong orange superfluorescence on the TPG-side of the photograph.

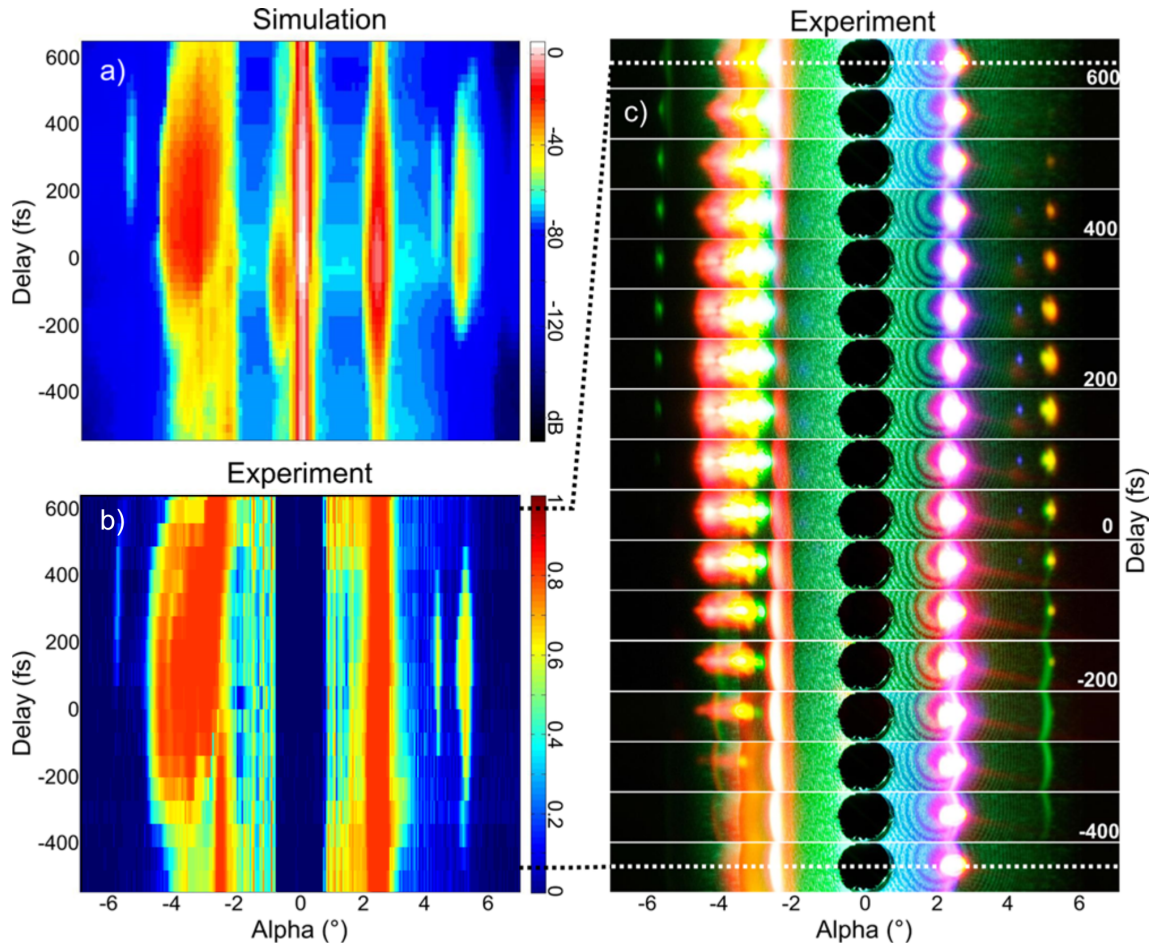


Figure 3.3: Angular variation of the intensity distribution with respect to the delay between pump and seed pulse: a) Mapped angular power distribution integrated over the visible spectrum as calculated by the numerical simulation for different delays. b) Mapped spatial brightness distribution extracted from the center line of each picture in (c) taken from an illuminated screen after the first amplification stage for different delays. [Mat13]

tribution leading to new phase-matching possibilities which cannot be analytically predicted at all. However, by means of the simulation results and the possibility to suppress specific spectral components and quantum paths as explained in Sec. 2.3.2, it is possible to clearly address each mixing product to its specific cascading path.

For a better comparison between the partly overexposed photographs with the simulation results, the RGB-values of the center line in each photograph are summed up and mapped into a 2D-plot with respect to the time delay between pump and seed pulse as depicted in Fig 3.3 (b). The angularly resolved visible part of the integrated power spectrum from the numerical results under the same conditions is also shown for different time delays in Fig 3.3 (a). It can be seen that the agreement between the

two figures is quite remarkable. Even the dynamics and the propagation direction of small and completely unexpected mixing products can be reproduced for the first time; e.g. the green mixing-signal at -6° for time delays between 200 fs and 400 fs or the blue mixing-signal at 4° at 200 fs. Therefore no fitting parameters are necessary. The only parameter which was chosen freely for the simulation was the amount of noise for the implementation of the superfluorescence which can be seen for time delays smaller -400 fs and for negative angles. However, this parameter does not have any influence on the mixing products which may carry important information as they will be discussed in the following. Furthermore, since the effort to measure such angular / time delay resolved spectra is quite low, it can be used for specifying the experimental parameter, e.g. the present phase matching conditions or temporal overlap, together with the information from simulation. Also by analyzing only two mixing products which depend differently on the seed-pump pulse delay, an active stabilization of the time delay could be realized which is insensitive to intensity fluctuations.

Since the representation of the results as described above was chosen to illustrate the dependency of the time delay between pump and signal pulses, the picture gains no information about the spectrum and the phase relations of the particular mixing products. Therefore, in the following the spectrally and angularly resolved simulation results will be discussed. The top of Fig. 3.4 compares the angular representation of the ordinary (red) and the extraordinary (blue) calculated power spectra (as explained in detail in Sec. 2.3.2) with the photograph showing only the visible output of the parametric process for an efficient parametric amplification of the signal. It can be impressively seen that each mixing product visible on the photograph can be clearly assigned to a nonlinear mixing process in the simulation shown by the intensity map. The color represents both the state of polarization and the spectral power density normalized to the maximum ordinary polarized power density on a logarithmic scale.

The detailed information about the respective polarization, spectrum, and propagation direction, as well as, about the group delay as explained later, makes it possible to address each mixing product to its specific cascading path. Therefore also a first suggestion about the origin of a specific mixing-signal, based on physical considerations, e.g. on phase-matching conditions or on the conservation of energy, can be tested in the simulation. This can be done by suppressing the nonlinear interaction of the fundamental spectral components, which are suspected to cause a certain mixing signal, as mentioned before.

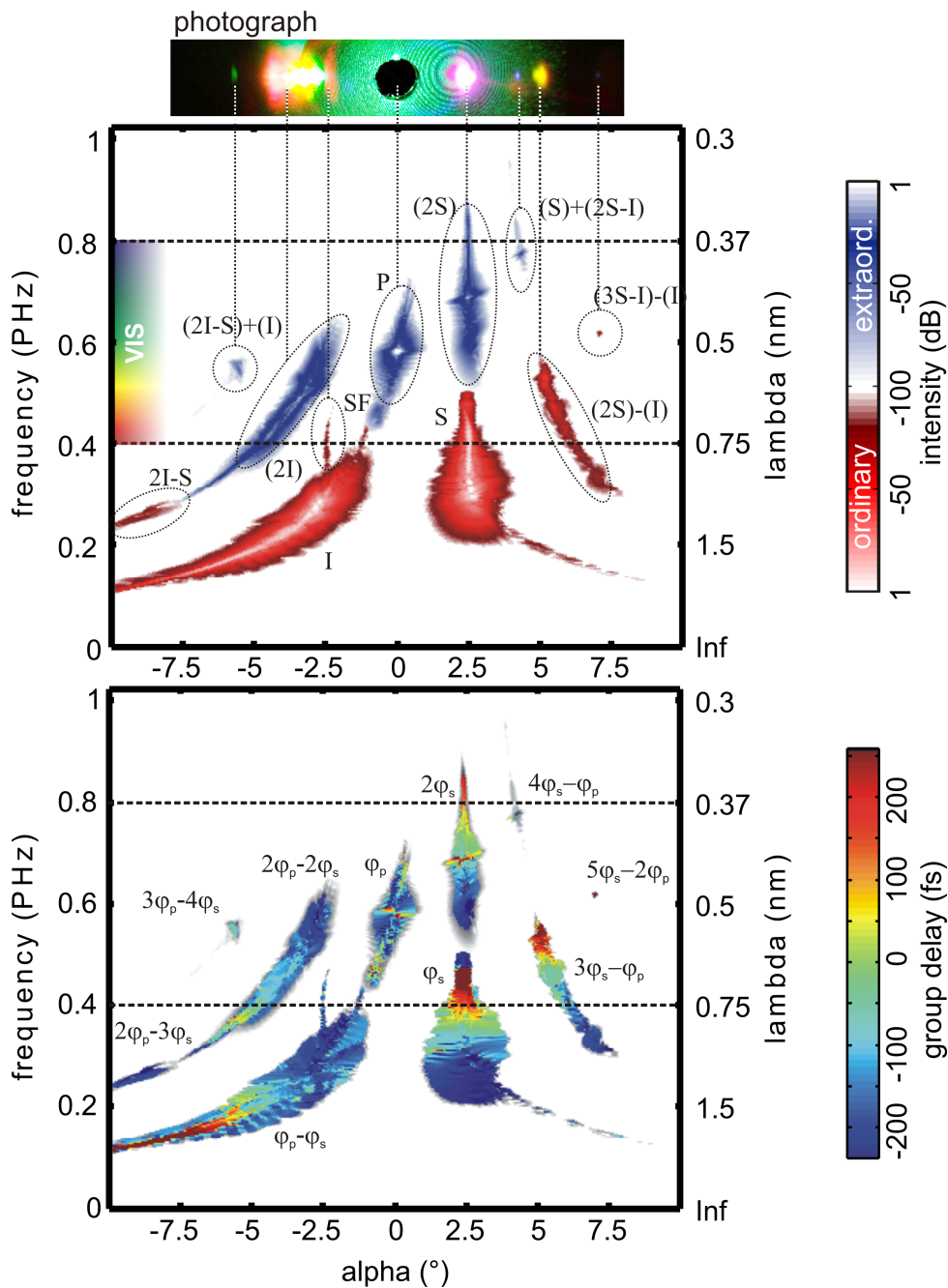


Figure 3.4: Illustration of the spectral, angular and temporal distributions of all visible and non-visible mixing products occurring in a high power OPCPA with optimum pump / signal overlap: **Top:** Identification of the specific features visible in the photographs (see also Fig. 3.3 (c)) of a screen illuminated by the signal (S); idler (I); superfluorescence (SF) and the additional mixing products, i.g. idler second harmonic (2I); signal second harmonic (2S); which are further cascaded to the parasitic DFG signal (2S-I) pumped by (2S) and seeded by (I); SFG of signal and parasitic DFG ($S + 2S-I$) and so on. The high intense pump beam (P) is passing through a hole in the middle of the screen. **Bottom:** Mapping of the relative group delay of each angular resolved spectral component which is addressed to their relative phase in respect to the phase of pump and signal pulses.

With this technique each component could be assigned to its cascaded mixing path starting from pump, signal and idler spectral field components as labeled by (P), (S) and (I) in the top of Fig. 3.4. Furthermore, since the phase of each spectral component is directly accessible in the simulation, the spectrally and angularly resolved group delay of each mixing product can be calculated as shown in the bottom of Fig. 3.4. For example, in this representation the strong positive chirp of the signal can be seen as it was given by the experimental conditions. From the same picture, however, it can be derived that the corresponding idler pulse is strongly negatively chirped for wavelengths beyond the point of zero dispersion in BBO (see also Sec. 2.2.3), whereas the constant group delay for idler frequency components below this point at $1.5\ \mu\text{m}$ indicates a compression of the respective components.

Since the pump pulse in the PVWC-geometry cannot be depleted completely³ a high intense part of it can drive the spontaneous amplification of the vacuum noise floor and randomly scattered photons along the direction with the highest parametric gain. As it was already explained above, in the photographs this effect can be observed by the orange stripe at -2.5° . Similar to the amplification of the seed pulse this parametric superfluorescence also generates a weak corresponding angularly chirped idler field at positive propagation angles.

The first and most important parasitic effect of a series of consecutive cascaded effects is caused by the second harmonic generation (SHG) of the idler and signal pulse, especially in the PVWC-geometry⁴. The result can be observed in the experiment and in the simulation (signed as feature (2S) and (2I) in Fig. 3.4). Besides the spectral hole-burning in the affected parts of signal and idler⁵, this parasitic SHG causes strong spatial and spectral modulations of the group delay due to the parametric phase induced by the back and forward conversion of the related spectral components [Ros02]. This leads to self compression effects and strong modulations in the temporal intensity distribution of the chirped signal and idler pulses which in turn influence the efficiency of the parametric process for different spectral components. In other words, the stronger the parasitic SHG, the higher the parametric phase contribution and spectral intensity fluctuations which consequentially will lead to residual satellites in a final pulse compression.

³The restricted pump depletion in the PVWC-geometry is explained in Sec. 2.2.2 and depicted for the specific case in Fig. 3.8 (c)

⁴Fig. 2.4 illustrates the angular dependence of the SHG-phase-matched frequency components in comparison to the phase-matching curve of the major parametric process. It can be seen that for wavelengths around $870\ \text{nm}$ this SHG-phase-matching curve crosses the signal spectrum. For negative angles the same is true for a broad part of the idler spectrum between $1.2\ \mu\text{m}$ and $1.5\ \mu\text{m}$.

⁵The conversion efficiency of the parasitic SHG as extracted from the simulation results is $\sim 2\%$ for signal SHG and $\sim 8\%$ for the idler-SHG.

Nevertheless, for some particular applications, the mentioned parasitic features can also be of use. For example, for the generation of isolated attosecond pulses by high harmonic generation (HHG) of high intensity few-cycle IR laser pulses, the carrier-envelope phase (CEP) of each pulse has to be stabilized [Man09]. This is usually realized by a feedback loop to the laser oscillator using a f-2f interferometric CEP-measurement which needs a portion of the available pulse energy to achieve a necessary spectral broadening after the amplification. Another possibility is shown by Hädrich *et al.* [Hae12]. They demonstrated the direct measurement and stabilization of the phase (CEP) by a f-2f scheme using the parasitic second harmonic of the broadband amplified signal pulses in the tangential phase-matching geometry (TPG). However, as it will be discussed in Sec. 3.3, especially for smaller pump pulse diameters, necessary for moderate pump pulse energies, the TPG shows important disadvantages in terms of compressibility of the pulses and quality of the beam profile compared to the PVWC-geometry. In this work a similar simple technique, as it was used by Hädrich *et al.* in the TPG, shall be proposed for the PVWC-geometry. This is only possible with the deep understanding of the origin of each mixing product, shown in Fig. 3.4, which will be described in the following.

For the given PVWC-example, the phase, polarization, timing, and direction of propagation of each mixing-signal is easily accessible since the complete series of the cascaded mixing processes can be reproduced numerically. Thereby, the cascaded path of the generation of each mixing product can be reconstructed. This is indicated by the labeling of the different features in the top of Fig. 3.4: namely the parasitic DFG signal (2S-I) pumped by signal second harmonic (2S) and seeded by the idler (I); the SFG of signal (S) and parasitic DFG (S + 2S-I); the parasitic DFG (3S-I - I) pumped by the cascaded SFG and seeded from the idler, etc. Furthermore, additional mixing products, not visible in the photograph (Fig. 3.4), can be proposed by the simulation.

This understanding of the complete process enables the derivation of the CEP of each mixing product with respect to the phases of the pump and the seed pulse. The result is shown by a label of each feature on the bottom of the Fig. 3.4, in which each phase results from the cascading path leading to the particular feature. The easiest example of course is the phase of the DFG-generated idler pulse, namely the difference of the phases of pump and signal ($\phi_p - \phi_s$). For all other components the phase can be derived from the signal and the pump phase in a similar way.

In order to find a method for a direct access to the signal-CEP, two cascaded mixing products with overlapping spectral components need to be found in which the pump phase is cancelled out in the f-2f interferometric measurement. In fact,

there are two angles where a simple analysis of the spectral fringes - caused by the interference of two overlapping mixing products - should enable for a measurement of the signal-CEP. Firstly, for the spectral overlap at 1 μm wavelength of feature (2I-S) and the infrared part of the second harmonic of the idler (2I) for an angle of -7.5° . Secondly, for angles around -1° right next to the propagation direction of the pump pulse, the spectrally broadened pump pulse - caused by the back conversion of signal and idler - overlaps with the very shortwave edge of the idler. Also for the interference of the frequency components around 750 nm the pump phase is canceled out which should lead to interferometric fringes in the optical spectrum directly connected to the CEP of the signal pulse.

In conclusion, by means of the (2+1)D simulation, all mixing products which are observed in a state-of-the-art OPCPA-system could be assigned and explained in detail for the first time. Based on this deep understanding and the possibility to simulate the whole process including the angular and spectral dynamics, an OPA-system can be well specified. For example, this can be done by just measuring some key mixing products under consideration of the angular and time delay dependent "finger prints" as explained above. Another possibility is to use specific mixing products with different time-delay dependencies for an active intensity insensitive stabilization of the system. Furthermore, by the analysis of the phase relations of each mixing product, a novel possibility is proposed for the direct measurement of the carrier-envelope phase for the signal pulses in the PVWC-geometry.

3.2 Two-color pumped sequential OPCPA-system

In the previous section an OPCPA-system was investigated, which consists of two stages pumped at the same wavelength. The goal of this system was to scale the pulse energy without changing the spectral bandwidth. The parametric amplification window of an OPA, however, can easily be shifted to different spectral ranges. This opens the possibility to enhance the amplification bandwidth of a multi-stage NOPA system by the combination of different amplification windows pumped at different wavelengths. This can be done either in a parallel setup or a sequential setup. For the parallel setup the different spectral components of an ultra-broadband seed, mostly a white light supercontinuum source, are amplified in different optical paths which need to be synthesized afterwards [Kra09a, Hua11]. The amplification in each stage is performed individually and does not differ from the example already given in the previous chapter. Whereas in the subsequent concept, which will be scope of this section, an ultra-broad seed spectrum is amplified in one path by means

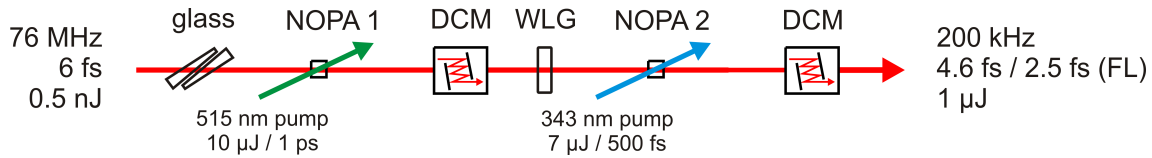


Figure 3.5: Schematic setup of the two-color pumped OPCPA-system [Har12]. NOPA 1: Optically synchronized frequency doubled pump pulses; NOPA 2: frequency tripled pump pulses both from a thin-disk regenerative amplifier; Seed: octave spanning commercial Ti:sapphire oscillator (VENTEON | PULSE: ONE); DCM: double-chirped mirror pairs for pulse compression; WL: white light generation in 3 mm BaF₂.

of two NOPA-stages pumped at different wavelengths. This sequential setup does not require an interferometric superposition of the pulses afterwards. Moreover, the nonlinear effects especially in the overlap region of the amplification windows are nontrivial.

In this section an in-house developed two-color pumped subsequential OPCPA-system is investigated by means of the (2+1)D simulation. As shown by Harth *et al.* the system was able to generate high energy pulses with an extremely broad spectrum supporting single-cycle Fourier limited pulse durations smaller than 3 fs [Har12]. Besides the fact that the critical part of the combined ultra-broadband spectrum could be compressed in the experiments, it also turned out that the amplification bandwidth of the individual amplification stages is much broader than it was expected by the simple phase-matching picture (see Sec. 2.2.1). Furthermore, contrary to the spectral gap which was expected in the overlap region of the two amplification windows, the experimental data have shown even a stronger parametric amplification. This section will clarify the origin of the surprising observation and explain the spatial and temporal effects behind it.

3.2.1 Experimental conditions

The experimental setup is shown in Fig. 3.5. Similar to the previous experiment the front-end of the system is a commercial Ti:sapphire oscillator delivering an octave spanning spectrum in a sub-6 fs pulse train with a repetition rate of 76 MHz. Very close to the previous concept, the infrared edge of the oscillator spectrum contains sufficient energy to directly seed a regenerative amplifier system at 1030 nm [Sch10]. The amplified output of this system is frequency-doubled in a first step to provide the pump pulses for the first amplification stage with a wavelength of 515 nm, a pulse energy of 10 μJ with a duration 1 ps. In addition, the third harmonic is generated

by a SFG to provide the 500 fs pump pulses for the second stage with a pulse energy of 7 μJ at 343 nm.

The remaining spectrum of the Ti:sapphire oscillator still supports sub 6 fs pulses which are stretched by air, glass, and the propagation within the BBO to approximately 260 fs. Both the pump and the seed beam are focused to a diameter of approximately 100 μm ($1/e^2$) into the 5 mm BBO crystal to provide a good conversion efficiency even for the rather low pump pulse energy. The crystal is oriented to operate in a broadband non-collinear PVWC-geometry in order to preserve a good spatial beam profile (see Sec.2.2.2) and to support a broad phase-matching bandwidth spanning from 680 nm to 1 μm as it can be calculated by the simple phase-matching considerations explained in Sec. 2.2.1 and is illustrated by the green shaded area in Fig 3.6 (a). In the experiment the signal pulses could be amplified by a factor of 2000, from 0.5 nJ to 1 μJ in this first NOPA-stage. In the next step, this amplified signal pulses are recompressed by 16 bounces on double-chirped mirrors close to the Fourier limit to drive a filament for the white light generation in 3 mm BaF₂ [Har12]. The generated supercontinuum, plotted by the blue line in 3.6(a), spans down to 430 nm and provides the seed photons for the next subsequent ampli-

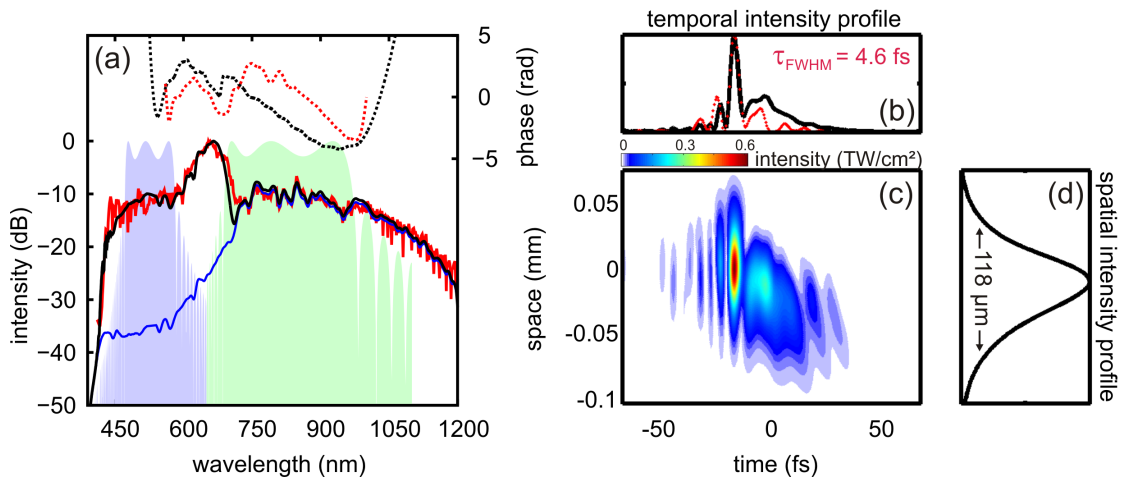


Figure 3.6: Simulation and experimental results of the sequential two-color pumped OPCPA-system [Har12, Lan13] : **a)** spectrum and phase measured after the two amplification stages (red) and as it is numerically calculated by the (2+1)D algorithm (black) for the same parameters, theoretical phase-matching bandwidth of the green pumped first stage (green shaded) and the blue pumped second stage (purple shaded), seed spectrum of the second stage after the white light generation (blue line); **b)** reconstruction of the compressed pulse shape from a SPIDER measurement and simulated spatially integrated pulse profile (black); **c)** spatiotemporal visualization of the simulated pulse; **d)** temporally integrated spatial pulse profile.

fication process. The weak visible part of the supercontinuum can now be amplified in the blue pump NOPA-stage which is phase-matched for the visible spectral range in PVWC-geometry. It is quite remarkable that the actually measured amplified spectral bandwidth, as shown by the red line in Fig. 3.6 (a), is significantly broader than the theoretically predicted gain bandwidth from the simple phase-matching picture (see Sec. 2.2.1), illustrated by the purple shaded area. Furthermore, for wavelengths in the overlap region of the two stages where actually no parametric amplification was expected, a prominent one order of magnitude higher amplification has been observed in the measured spectrum. However, the measured spectrum supports sub-3 fs-pulse durations with pulse energies of about 1 μ J. Although Harth *et al.* could prove the compressibility of the critical spectral overlap region between the two stages, there are many open questions about the performance of the system and the observations that have been made in the experiments. The next section will discuss the most prominent questions which could be explored by means of the (2+1)D simulation.

3.2.2 Unexpected amplification bandwidth and spectral features

In order to understand the origin of the enormous parametric amplification in the spectral overlap region and also the surprisingly broad spectral bandwidth of the blue pumped second stage, the nonlinear process is carefully analyzed by means of the (2+1)D simulation. Especially the modulations in the spectral phase around this intensity peak can only be understood by revealing the temporal and spatial pulse shaping dynamic during the parametric amplification process [Lan13].

In the following the simulation results of the system will be presented to clarify the most prominent and unexplained observations in the experiment. Firstly, it should be mentioned that the results from the simulation are again in very good agreement with the experimental results. Thus, the energy of the simulated signal pulses after the second stage of 1 μ J and the pulse durations of 4.3 fs are comparable to the measurement. Both results are obtained under similar conditions, after a compression of an essential part of the spectrum between 500 nm and 1000 nm by 23 bounces on DCMs and the CaF₂-wedges. For the simulated results this has been done by adding the respective dispersion as it can be calculated employing the design curves of the DCMs and the Sellmeier coefficients of the used material. Also the spectral phase of the simulated compressed pulses (Fig. 3.6 (a), black dashed) shows qualitatively the same characteristic features as the measurement (red dashed) using a SPIDER apparatus. Fig. 3.6 (b) compares the temporal pulse shape of the measured and the simulated compressed pulses. Therefore the spatiotemporal intensity distribution of

the simulated pulse is spatially integrated. In the full picture, however, it can be seen that the small pedestal oscillations in the leading part of the temporal pulse profile are homogeneously spatially distributed, whereas the broader ripples in the trailing part are clearly displaced to one side. Considering the uncompressed spatiotemporal pulse profile (shown later in Fig. 3.7 (c)) together with the residual phase contributions of the compressed pulse (shown in Fig. 3.6 (b)) this homogeneously displaced trailing part of the pulse can be attributed to the positive dispersive long-wave edge of the prominent intensity peak. Nevertheless, the overall time-integrated spatial pulse profile (Fig. 3.6 (d)) shows a good Gaussian-like profile.

The simulated spectrum (black solid) is also in a remarkably good agreement with the measured spectrum (red solid) (Fig. 3.6 (a)). Thereby, the prominent strong parametric amplification and the modulations for wavelengths between 600 nm and 700 nm as well as the enlarged phase-matching bandwidth can be well understood by considering the temporal and spatial evolution of the involved pulses. Fig. 3.7 shows the angularly resolved spectra of the idler (a) with respect to the related signal (b) spectral components (long-wave idler photons correspond to the short-wave signal photons) and their spatiotemporal pulse shapes (c-d) right after the crystal. It can be seen that the generated idler-pulse is strongly angularly chirped, whereas the signal pulse propagation is unidirectional with an angle of 4.5° relative to the wave vector of the pump. Since the Poynting vector walk-off angle of the pump pulse (4.45°) is similar to this non-collinear angle of the signal, the good overlap of the two pulses leads to a good spatial beam quality even for the small spot sizes (90 μm) and the rather long crystals (5 mm). In contrast, the large angles of the idler - up to 15° for long-wave spectral components - lead to a very short spatial overlap with the related signal photons which are in co-propagation with the pump. The result is a shortened effective interaction length and a suppressed back conversion, especially for long idler wavelengths and the related short signal wavelengths. Consequently, the phase-matching bandwidth is enlarged, compared to the phase-matched spectral range calculated by the simple phase-matching picture as explained in Sec. 2.2.1. This effect is also visualized by comparison of the simulated (black line) and measured (red line) bandwidths with the theoretical amplification bandwidth (blue shaded) in Fig. 3.6 (a). Unfortunately, besides the larger phase-matching bandwidth due to the absence of idler photons, the overall signal gain for the blue edge of the spectrum is limited for the same reason. This effect can not explain the prominent intensity peak between 600 nm and 700 nm, since the idler non-collinear angles in the degeneracy of the blue-pumped amplification stage are relatively small.

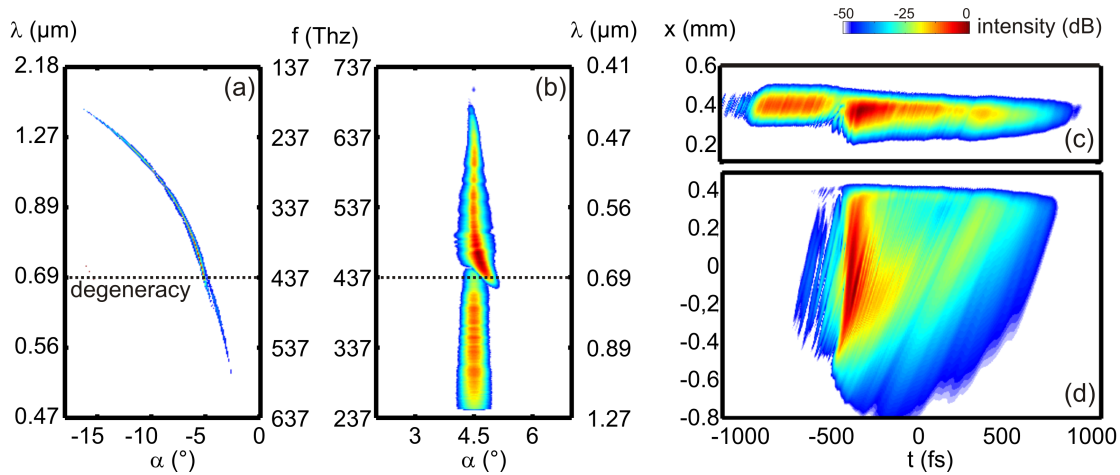


Figure 3.7: Simulation results of the angularly resolved signal (a) and idler (b) optical spectrum (the scaling of the wavelength is chosen in a way that the corresponding spectral signal and idler components are on the same height) and the spatiotemporal power distribution of the signal (c) and idler (d) pulses.

At this point another effect shall be discussed which can explain this strong parametric amplification in the spectral overlap region of the two amplification windows. Whereas the positively chirped signal pulses in Fig. 3.7 (c) are stretched in time, the idler pulses (d), generated with the opposite chirp (see Sec. 2.2.3), are compressed and localized in time at relative group delays around -400 fs. This reduces the temporal overlap between the compressed idler pulses and chirped signal components not located around these group delays. Due to the equal group velocity of signal and idler near degeneracy, the high intensities of the compressed idler are located at a temporal/spectral position of the dispersed signal pulse between 600 nm and 700 nm. Consequently, the strong co-seeding by the compressed idler pulse leads to the higher parametric amplification of the signal in this spectral range. Furthermore, this high parametric gain also causes a strong pump depletion and cascaded back- and forward conversion, which is responsible for the modulation of the spectral phase around 700 nm.

In conclusion, quite surprising experimental observations in a novel two-color pumped OPCPA-system can be explained for the first time by analyzing the spatiotemporal pulse shaping dynamics occurring during the parametric amplification in the two subsequential NOPA-stages. As explained in the next section, the first green-pumped amplification stage was operated with a remarkably high amplification factor at a rather low pump pulse energy. As observed in the experiment, as well as, indicated by the onset of the self-focusing in the simulation, the pump beam

was close to initiating a filamentation process in the BBO crystal. This is caused by the combination of the enormous peak intensity required for a sufficient parametric amplification and the extreme pump focus necessary to reach these intensities for the rather low pump pulse energies. As it will be classified in the next section, this system becomes a good example for an operational regime of OPAs working at the lower limit in terms of pump pulse energy and pump beam waist.

3.3 Limits of the non-collinear phase-matching geometries

In the previous sections, two OPCPA-systems, each with two subsequential non-collinear parametric amplification stages representing different regimes, have been analyzed concerning the available pump pulse energy and the related spot size of pump and seed. As discussed in the last example, especially for long crystal lengths and small spot sizes, spatial effects play an important role for the spectral and temporal evolution of the amplified signal pulses. Contrary to this, the analyzed high-power OPCPA-system represents a different situation with more relaxed beam diameters and higher pump pulse energies. An additional regime can be introduced considering a recently published work by Demmler *et al.* considering short crystal lengths with a rather soft focusing and enormous pump energies. In this work a (1+1)D simulation, excluding spatial effects, has shown an excellent agreement with the experiment [Dem12]. Hence, the importance of spatial effects in ultra-broadband parametric amplifiers is strongly connected to the available pump energy and consequently to the optimum focusing and the right choice of the phase-matching concept (PVWC or TPM).

This section gives an overview of the different OPCPA-systems, differ in their combinations of pump energies and optimum waist diameters and the chosen non-collinear phase-matching geometry. The analyses concerning the efficiency, beam quality and the compressibility / peak power of the amplified signal pulses, will allow to classify these systems in three different regimes and to formulate guidelines for designing future OPA systems [Lan13].

Regime of strong spatial and cascaded effects

The first scenario forms a good example for a regime with strong spatial and cascaded effects in OPA systems. In this regime the cost-efficient and compact pump laser system provides only moderate pump pulse energies at high repetition rates.

Nevertheless, in order to achieve a sufficient efficiency of the parametric conversion process, these pump pulses need to be tightly focused in the nonlinear crystal of the OPA. The lower limit of this regime is given by the damage threshold of the crystal. Since the peak intensity for a sufficient parametric amplification is comparable for all regimes (about 100 GW/cm^2), the damage of the crystal in this regime is mainly caused by the onset of the self-focusing of the pump pulse which consequently leads to the generation of free electrons and the absorption of the pump. A perfect example operating at the lower edge of this regime is the green pumped amplification stage of the previously presented two-color OPCPA-system in Sec. 3.2.1. This NOPA-stage is pumped in the PVWC-geometry by 1 ps pulses with a pulse energy of $10 \mu\text{J}$, tightly focused to $50 \mu\text{m}$ of beam radius ($1/e^2$). The experimental results (red), as well as the extracted signal spectrum (black solid), parametric group delay (black dashed) and the angular resolved spectral and spatiotemporal power distribution as calculated by the (2+1)D numerical model are illustrated in Fig. 3.8 (a). The parameters for the simulation, such as the phase-matching angle of 24.65° and the non-collinear angle of 2.65° , can be extracted precisely from the experiment by comparing the phase-matching of the parasitic SHG to the gap in the signal spectrum and the prominent minimum in the parametric group delay at 855 nm .

As it can be seen in Fig. 3.8 (a), by simply using the same parameters as used in the experiment, the strong modulations in the measured output spectrum (red shaded) and the induced parametric group delay (red dashed) due to the parasitic SHG of the signal and idler, can be simulated in quantitative agreement. Within the limits due to the unconsidered dimensions as explained in Sec. 3.1.1, the pulse energy calculated from the simulation data is also in good agreement with the measured signal pulse energy of $1 \mu\text{J}$. In contrast to the experiment, all information about the spatiotemporal and the spectral pulse evolution in the parametric amplification process are easily accessible. So, besides the angular distribution of the particular spectral components in the inlet, also the spatiotemporal shape of the depleted pump and the generated signal and idler are shown in Fig. 3.8 (a). In this first scenario it can be seen, that a major part of the amplified signal spectrum is propagating unidirectional with an angle of 2.65° relative to the propagation direction of the pump. Even though the infrared spectral components beyond $1 \mu\text{m}$ show a slight variation of this main propagation direction of the signal pulse, the good overall beam profile of the signal in the focal plane is ensured by the spatial localization effect in the PVWC-geometry as described in Sec. 2.2.2. This also results in a good M^2 -value, independent from the initial beam waist of the seed pulse, at least for a

major part of the spectrum as it can be seen in Fig. 3.9 (a). The bad M^2 -value in the spectral gaps is caused by the distortions due to the parasitic SHG of the signal and idler pulses in the PCWC-geometry. Anyway, these spectral components do not contribute to the overall pulse profile.

For a better comparison of the different examples and to give a more precise description of the compressibility of the simulated pulses by the use of commercially available doubled chirped mirrors (DCMs), a compressor is modeled with regards to the experimental conditions and the designing curves of DCMs. By using 5 bounces on each of the DCMs, the simulated signal spectrum integrated within an angular range of 1 mrad (centered along the red line) is compressed to a maximum peak power of $100 \text{ kW}/\mu\text{J}^6$. However, the result of the mentioned compression strongly depends on the third order dispersion (TOD) of the used DCMs which in principle can be designed freely to compensate for the TOD of the used nonlinear crystal or even for the TOD induce by the parametric process itself [Ros02]. Therefore, in Fig. 3.10 the spatiotemporal pulse profile is depicted as simulated and compressed by using an optimal combination of negative GDD and TOD values to maximize the peak intensity of the amplified signal pulse. For the first example it can be seen in the PWVC-geometry, that the good beam profile and the good compressibility to 6.7 fs leads to a peak intensity of $1.3 \text{ TW}/\text{cm}^2$ in case of an one-to-one imaging of the output surface of the crystal.

In order to compare the two phase-matching geometries for the different regimes, the parametric process is simulated under the exact same conditions but with a negative non-collinear angle for the tangential phase-matching geometry (TPG). Unfortunately, no carefully measured data of the green pumped first stage of the two-color pumped OPA system in the TPG is available. However, during the experiments in the lab, rough measurements of the first stage in the TPG qualitatively show much higher pulse energies and a red-shifted output spectrum. This experimental observation is in good agreement with the changes of the output spectrum shown in Fig. 3.8 (b) and show three times higher efficiency as it is simulated. The explanation of these strong differences between the two geometries is given in Sec. 2.2.2. Especially the strong pump depletion (see Fig. 3.8 (b) - pump) supports the "mirrorless-co-seeding theory", as explained in Sec. 2.2.2, for the stretched long-wave idler components at large non-collinear angles and the related short-wave signal components. Nevertheless, the higher conversion efficiency in the first example, predicted by the simulation and qualitatively observed in the experiment,

⁶Note, in the related publication [Lan13] this and the other two examples were mistakenly reported in being able to compress the pulse in order to get peak powers in the range of $\text{GW}/\mu\text{J}$.

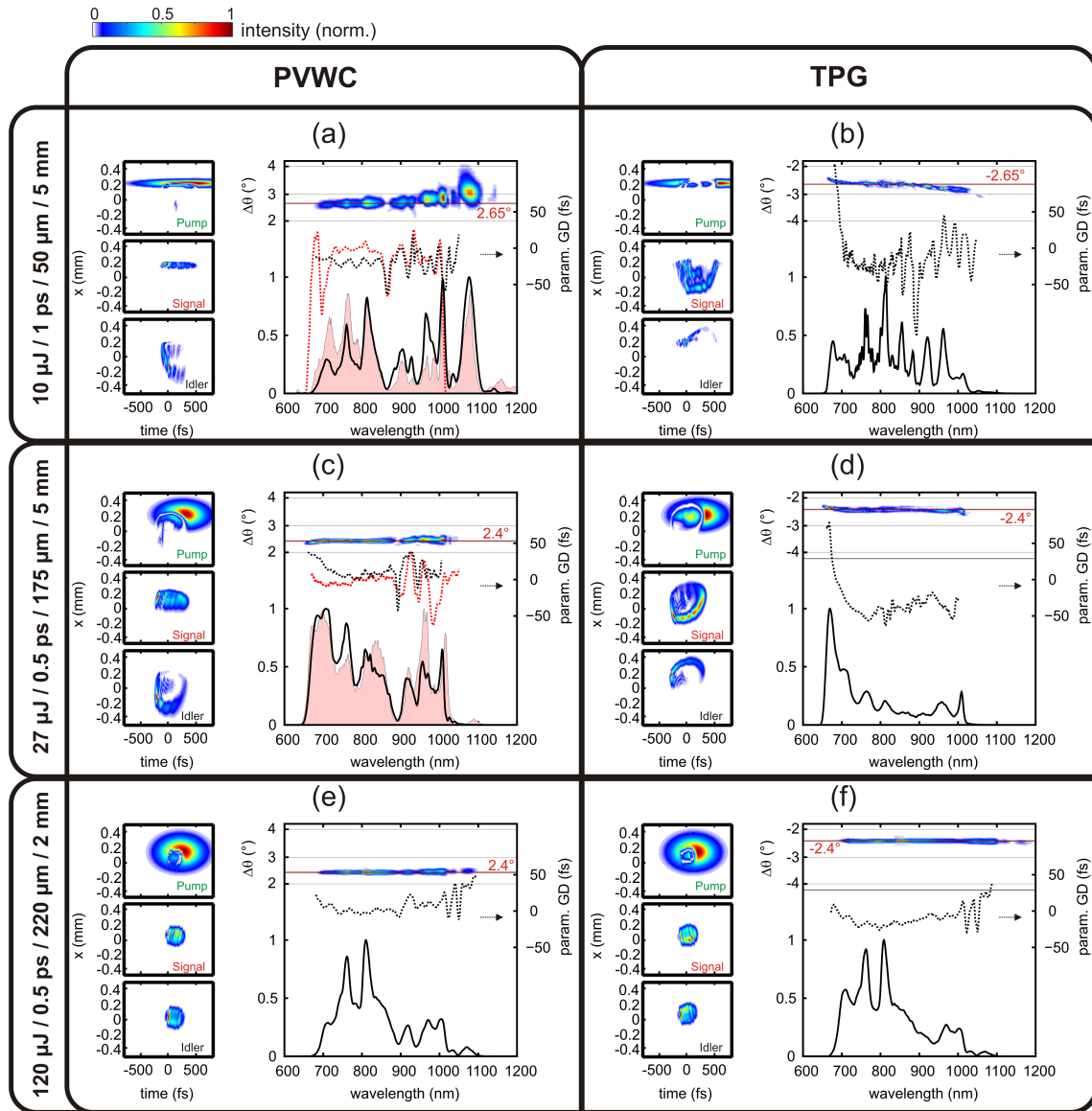


Figure 3.8: Comparison between the two non-collinear phase-matching geometries, Poynting Vector Walk-off Compensation (PVWC) and Tangential Phase-matching Geometry (TPG), with different pulse energies, durations, pump spot sizes ($1/e^2$ radius) and crystal lengths. Simulated beam profiles of pump, idler, and signal pulses in time and one transversal dimension in the principle phase-matching plane of BBO. The diagrams show the simulated signal-spectra (black solid) as well as the measured spectra (red shaded) and the measured parametric GD (red dotted). The simulated parametric GD (black dotted) is evaluated along the red line in the colored map on top of each example illustrating the non-collinear angle distribution of the signal spectral intensity. The evolution^a of each scenario with respect to the position along the crystal clarifies the interplay between all pulses and the origin of spectral and temporal changes in the seed pulse.

^aPlease find the animated movie illustrating the propagation through the crystal and the temporal evolution of all the different scenarios online in Media 1 [Lan13]

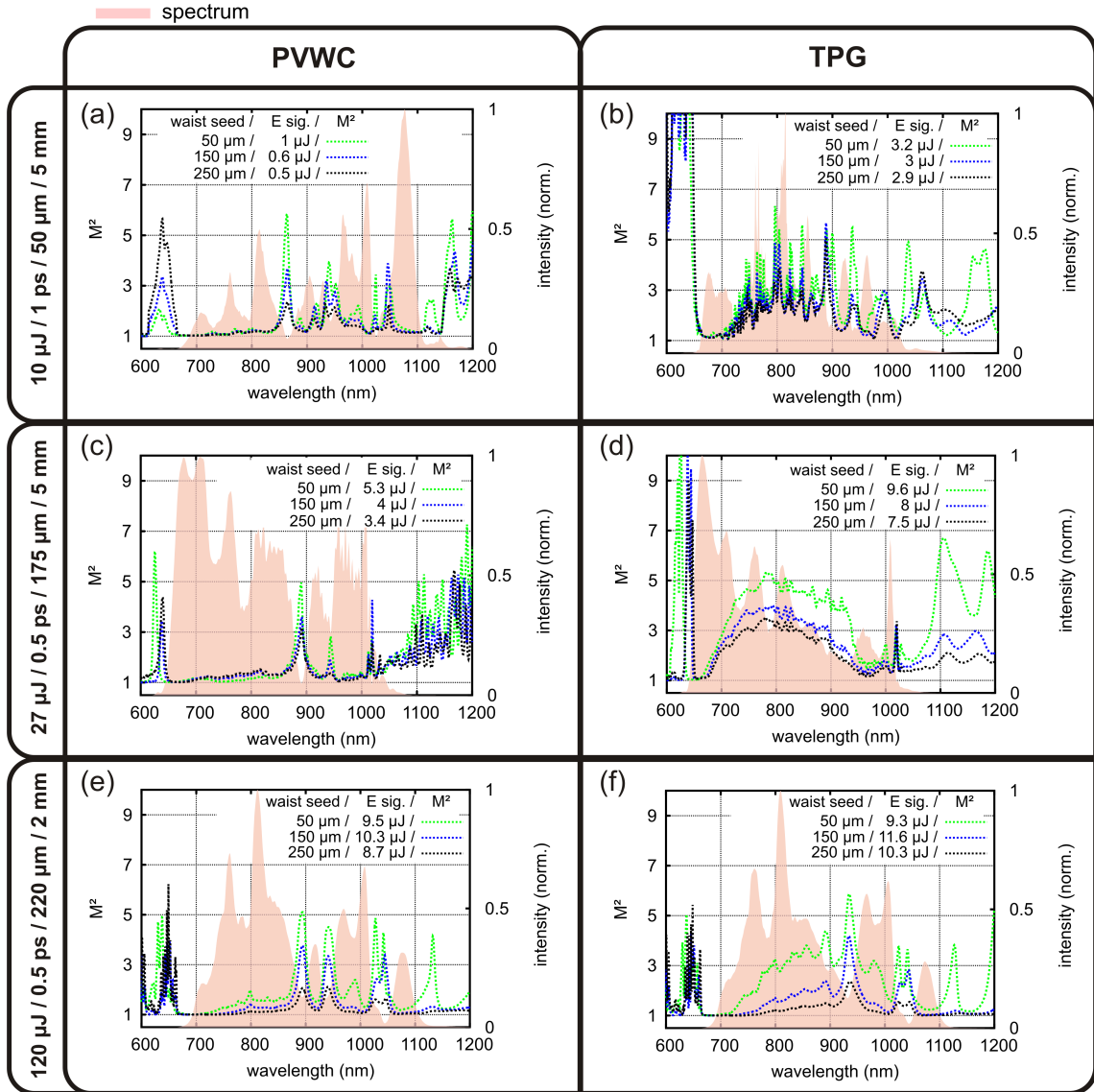


Figure 3.9: Comparison between the two non-collinear phase-matching geometries, Poynting Vector Walk-off Compensation (PVWC) and Tangential Phase-matching Geometry (TPG) with different pulse energies, durations, pump spot sizes ($1/e^2$ radius) and crystal lengths. The figure shows the wavelength dependent beam quality factor $M^2(\lambda)$ (dotted) with respect to the angular integrated signal output spectrum (red shaded) as it is calculated by the (2+1)D simulation algorithm. The quality factor is calculated with the second momentum of the spectrally resolved angular $\Theta(\lambda)$ and spatial $w_0(\lambda)$ power distribution at the output surface ($z_0 = L_{\text{crystal}}$): $M^2 = \frac{\pi}{\lambda} (\Theta(\lambda) \cdot w_0(\lambda))$.

cannot compensate for the poorer beam profile. The resulting bad M^2 -value (see Fig.3.9 (b)) and bad compressibility as shown in Fig.3.10 (b) lead to a smaller peak intensity in the focal plane at the output surface of the crystal. Furthermore, the better focusability of the Gaussian like beam profile and the good beam quality factor M^2 in case of the PVWC, at least for the intense spectral components as shown in Fig.3.9 (a), have to be taken into account for the evaluation of the two geometries.

In conclusion, this first scenario, as an example for OPAs pumped by tightly focused low energy pulses, show a much better performance in the PVWC-geometry. This is especially obvious from the beam quality factor M^2 for different seed waists compared to the TPG. Whereas the PVWC-geometry, even for the smallest seed waist, the overall beam quality factor is close to one, the TPG always shows a poorer beam quality. Here, only for the shortest signal spectral components a good beam quality can be obtained. For this shortwave narrowband signal components the TPG benefits from the extremely strong and highly efficient pump depletion (explained by the co-seeding effect in Sec.2.2.2). Accordingly, with a sufficient crystal length, the pump beam could be almost entirely transferred to a signal band around 680 nm and the related idler at 2.1 μm , still preserving a good beam quality for this narrow spectral range.

Regime of medium and minor spatial and cascaded effects

In contrast to the examples in the regime with strong spatial and cascaded effects, the next two examples represent OPCPA-systems pumped with much higher pulse energies and more relaxed beam waists. However, especially the second example, which was discussed in detail in Sec.3.1, still shows strong differences between the two phase-matching geometries. Even though Fig.3.8 (c-d) show significantly smoother power spectra in both geometries, the differences in the spatial and spectral power distribution are still obvious. The smoother spectrum can be attributed to the significant reduction of the back- and forward conversion due to the softer focus of 175 μm ($1/e^2$ - radius). Nevertheless, the rather long crystal length (5 mm) still leads to a strong spatial distortion of the signal pulse in the TPG-configuration. Furthermore, the typical stretching of the idler spectral components beyond the zero-dispersion point of BBO goes along with a strong induced parametric group delay as illustrated by the dotted line in Fig.3.8 (d). Thus, as shown in Fig.3.10 (d), the compressibility in the TPG is rather poor and, as indicated by the long tail in the compressed spatiotemporal profile, the highly efficient amplified red peak in the TPG-spectrum cannot be compressed at all. It should be noted, that the waist of the seed pulse used for the simulation, as it is determined by the experimental setup

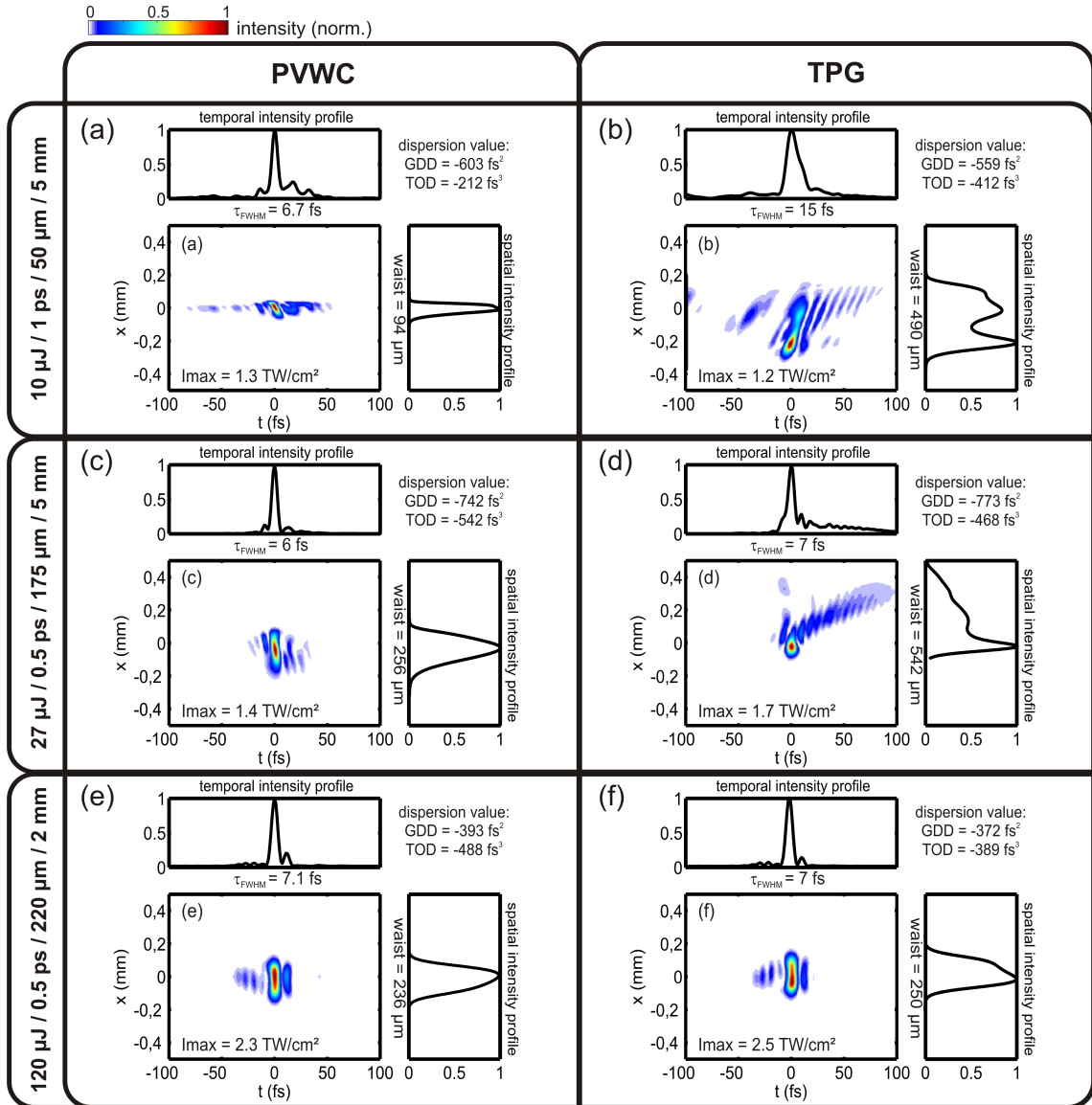


Figure 3.10: Comparison between the two non-collinear phase-matching geometries, Poynting Vector Walk-off Compensation (PVWC) and Tangential Phase-matching Geometry (TPG), with different pulse energies and durations, pump spot sizes ($1/e^2$ radius) and crystal lengths. The figure shows the spatiotemporal signal pulse profile after the best possible compression by using first and second order negative dispersion in order to maximize the peak intensity (I_{\max}). The beam size is similar to one-to-one image of the crystal surface.

(see Sec. 3.1), was much smaller than the pump pulse waist. Since the beam quality of the amplified signal pulse in the TPG strongly depends on the seed / pump waist ratio, the M^2 -factor is plotted in Fig. 3.9 (d) for three different seed waists. It can be seen, that even for seed waists much larger than the pump waist, the beam quality factor of the signal is rather poor for the important intense part of the output spectrum. In contrast, in the PVWC-geometry the good spatial beam quality and M^2 -value of the intense spectral components of the amplified signal pulse promises an excellent further focusability, even in the case of a tight seed focus for a higher efficiency.

Consequently, even with almost twice the output pulse energy of $9.6 \mu\text{J}$ in the TPG, the maximum compressed peak power in the focal plane at the end of the crystal is comparable to the one in the PVWC (see Fig. 3.10 (c-d)). Additionally, due to the better beam quality and focusability, the PVWC-geometry should be the method of choice even for high power OPCPAs with medium pump focusing, as given in the example two.

The third scenario, which is a very good example of a regime with less spatial influences, is inspired by a recently published high-power OPA system [Rot12]. Here, the simulation of the two phase-matching geometries is done under the same parameters as used before in scenario two, but with $120 \mu\text{J}$ of pulse energy and an almost unfocused pump beam in just 2 mm of BBO. As it is shown in Fig. 3.8 (e-f) the spectra of both geometries do not strongly differ anymore. Only the dip in the spectrum and the phase around 900 nm caused by the parasitic SHG of the signal pulses for PVWC makes a small difference. Because of the mentioned seed-waist dependence of the beam quality in the TPG this last example is also calculated for three different seed pulse diameters in both geometries. As illustrated in Fig. 3.9 (e-f), whereas in the PVWC-geometry the beam quality only shows a small dependency on the seed focus, in the TPG at least for seed diameters larger than the pump focus a good M^2 factor can be preserved. Also in the spatiotemporal plots, the tangential geometry provides a reasonable beam profile, and a good compressibility due to the moderate parametric GD of the short signal wavelengths in the 2 mm short crystal.

In contrast to scenarios one and two, this case marks the transition from the regime where spatial effects play an important role for the choice of the geometry of the parametric process, to a regime in which the walk-off between the pulses is quite small compared to their spot sizes. In this regime the tangential geometry can show advantages, since the absence of the parasitic SHG-effect of the signal leads to a slightly lower phase distortion and a higher achievable output energy - also reported in [Bro11].

To give a compact summary: the first regime includes very compact OPCPA systems with low pump energies of about $10\ \mu\text{J}$. In this regime spatiotemporal, parasitic and cascaded effects dominate the parametric amplification process leading to strong modulations in the spectral intensity and phase. Due to the necessary tight focusing of the pump beam to less than $100\ \mu\text{m}$ and the rather long nonlinear crystal of about $5\ \text{mm}$, only the PVWC-geometry can preserve a good beam quality. The second regime was defined for OPCPA systems which are still quite compact, however, a higher effort in the pump laser system or a reduction of the repetition rate lead to higher pump pulse energies of about $30\ \mu\text{J}$. In this regime spatial, cascaded and parasitic effects still play an important role but, due to the moderate pump beam waist of less than $200\ \mu\text{m}$, the influences are significantly reduced. Nevertheless, also in this regime, the beam quality and the compressibility in the TPG is not practical. The last regime was defined for systems with hardly focused pump and seed beams and pump energies beyond $100\ \mu\text{J}$. Here spatial effects do not influence the parametric amplification process anymore and the TPG can be preferred, since the SHG effect is shifted into the IR-edge of the amplified signal beyond $1\ \mu\text{m}$.

3.4 Conclusion

In this chapter the spatial and temporal pulse shaping dynamics of a non-collinear ultra-broadband optical parametric amplification processes were carefully studied. Therefore, a variety of different OPA experiments were investigated with aid of a novel (2+1) numerical simulation model, including all spatial, temporal, and cascaded effects as well as every parasitic second order nonlinear processes in such systems. It could be shown that the results of simulation algorithm are in a very good agreement with the experimental observation, even though the different systems operate in a strongly varying parameter ranges.

Because of the insights given by the comprehensive access to the complete nonlinear process and the possibility to distinguish and evaluate each of the convoluted effects, a deep understanding of the physics behind well known observations in high power OPA systems could be achieved. Furthermore, the behaviour of future OPCPA-systems and second order nonlinear effects in general can be predicted without the use of large computer clusters due to the moderate requirements for computing power.

Since every cascaded mixing product during the non-collinear parametric interaction is automatically included in the model, a new possibility can be proposed to directly measure the carrier-envelope phase of the signal pulse in state-of-the-art

high power OPCPAs operating in the PVWC-geometry. Especially for applications such as the generation of isolated attosecond pulse by the high harmonic generation process at high repetition rates, OPCPAs are going to be the future working horses for the generation of the high intense few-cycle IR driving pulses [Mat13, Rot10]. These experiments would benefit from a direct measurement of the CEP also in the PVWC-geometry.

Last but not least, the knowledge about the complicated processes during a single pass through an ultra-broadband nonlinear gain medium is the first step to understand the complex pulse dynamics in a non-collinear optical parametric oscillator (NOPO) which will be the topic of the next chapter.

Chapter 4

Ultra-broadband phase-matched Non-collinear Optical Parametric Oscillators

The scope of the previous chapter was to understand the various effects taking place in high power octave spanning OPCPAs. These systems are quite impressive since they can provide μJ -pulse energies by reaching 1 MHz repetition rates [Rot12, Mat13, Sch10]. However, the technical effort and the cost of these systems are quite high since besides the amplification systems that are necessary for the strong pump pulses a broadband seeder has to be provided.

However, for many applications, these high pulse energies are not necessarily required, instead much higher repetition rates directly from an oscillator would be beneficial. For most of these applications, e.g. femtosecond stimulated Raman spectroscopy [Hof13] or in vivo spectroscopic life-time measurements on biological samples [Liu02], etc., the higher repetition rates would contribute to a higher photon flux and an increased statistics.

Most of the mentioned features together with an excellent noise behaviour and octave spanning spectral bandwidths are provided by commercial Ti:sapphire oscillators. However, the pulse energies, available directly from these oscillators, are restricted mainly by one fundamental limitation, namely the unavoidable heat load in the laser crystal. Consequently, even though octave spanning Ti:Sapphire oscillators are very well established, the available average output power is restricted to several hundreds of milliwatts. Especially applications which require narrowband rapidly tuneable ultra-short light pulses suffer from the rather low spectral power density smaller 2 mW/nm of these ultra-broad lasers. Even though, narrowband tuneable Ti:sapphire oscillators can reach higher spectral power densities, the tun-

ing speed of these systems is quite low (e.g. TS:fast from HighFinesse GmbH reaches $< 100 \text{ mW/nm}$ with a tuning speed of 2 nm/ms between 680 and 1000 nm).

Although nowadays Ti:sapphire oscillators are the working horses in many applications, higher average powers and higher pulse energies are desirable. To overcome these power restrictions, and, in addition to reach spectral ranges beyond the amplification window of Ti:sapphire, femtosecond optical parametric oscillators (OPOs) represent an advantageous alternative. In the recent years OPOs have become more and more interesting, especially for frequency-comb spectroscopy of atoms in the UV-spectral range or for molecule spectroscopy in the mid-IR and the IR spectral region. In contrast to the different laser materials, the gain window of the parametric process is only restricted by the transparency range of the nonlinear crystal and the chosen phase-matching conditions. As a result, tuneable OPOs were demonstrated covering almost the whole spectral range from the UV up to the far infrared [Rei98, Bhu09, Row11, Gho08]. Furthermore, by using broadband phase-matching concepts OPOs are able to generate sub-100 fs pulses. The shortest pulses, down to 15 fs, from an OPO shown so far, were demonstrated by Gale *et. al* by using self-compression effects in the PVWC configuration and a prism-based dispersion management [Gal98]. However, for pumping these systems, mainly commercial narrowband Ti:Sapphire lasers with pulse duration around 100 fs are used, providing pump powers up to 3.5 W. Consequently, the mentioned lack of power scalability of the Ti:Sapphire oscillators became the main limitation for these systems in terms of output power, which typically is in the lower mW-range. Therefore, the applications of OPOs were mainly restricted to wavelength regions where no other laser source is available.

Due to the fact that no energy is stored in the nonlinear crystal during the optical parametric process it is ideally suited for a further power scaling. Moreover, in contrast to Ti:sapphire which is usually pumped by commercial cw-DPSS-lasers, the parametric gain in a fs-OPO strongly depends on the intensity and the temporal overlap of the pump pulses. Therefore, especially with the recent power scaling of Yb-based thin disk fs-laser sources [Sar12a, Pal08, Pro11], high power optical parametric oscillators have been demonstrated with several Watts of output power [Lam09, Heg11, Adl09]. Nevertheless, these systems mainly use quite long QPM-periodically poled crystals¹ pumped at the fundamental laser wavelength of about 1 μm . Consequently, their operational spectral range is restricted to the mid-IR with a rather narrow phase-matched bandwidth of some tens of nanometers for a constant

¹Quasi-phase-matching geometry (QPM): The nonlinear susceptibility of the crystal is modulated periodically in order to compensate for the phase-mismatch of the involved electrical fields due to dispersion [Yam91].

poling period and temperature of the crystals. This limits both shortest available pulse durations and a fast tuneability.

The goal of this work was to develop a non-collinear optical parametric oscillator (NOPO) which combines the broadband gain bandwidth by use of a non-collinear phase-matching concept and a state-of-the-art dispersion management by using double-chirped mirrors pairs. Furthermore, a significant increase in the output power and an operation in a spectral region similar to Ti:sapphire oscillators, will be reached by applying a modern pumping concept by using a frequency doubled high power thin-disk laser.

Accordingly, the broad gain bandwidth can either be used to realize a high power widely tuneable NOPO system or for the generation of high energy few-cycle pulses with high repetition rates directly from the oscillator. Both concepts will be discussed in detail. The first section will introduce some theoretical considerations which help to understand the following rather complex mode-locking processes and tuning behavior as observed in the experiments. In Sec. 4.1 the experimental realization and the results from an ultra-wide and rapidly tuneable high power femtosecond NOPO are presented and discussed [Lan12]. In the second part in Sec. 4.2, aided by the acquired knowledge from the tuneable highly dispersive NOPO, the concept of an ultrashort-pulse NOPO with breathing pulse dispersion management and Kerr-lens mode coupling mechanism is introduced. The experimental setup developed for the generation of stable mode-locked sub-10 fs pulses directly from a high power NOPO will be discussed and the first results will be presented.

4.1 Widely tuneable femtosecond NOPO

Tuneable femtosecond optical parametric oscillators (OPOs) are an ideal source of ultrashort laser pulses with a high average power over a wide range of the optical spectrum. For applications like scanning imaging microscopy combined with non-linear spectroscopy, a high photon-flux and a wide tuneability is required [Zip03]. Especially the ultrashort pulse durations and the possibility to provide multiple optically synchronized pulse trains within one system² open the possibility to take advantage of the high peak intensities and temporal resolution for higher order non-linear spectroscopic applications, e.g. time-resolved coherent Anti-Stokes Raman scattering (CARS) [Hof13].

²Because of the instantaneous nature of the parametric conversion process, all pulses within an OPO-system are optically synchronized to the fundamental pump laser. For example: fundamental pump pulse \rightarrow second harmonic pump pulse \rightarrow OPO signal and idler pulses.

Such OPOs are well established and commercially available nowadays, but the drawback of all these systems is the concept to use a relatively long nonlinear crystal under narrowband phase-matching conditions. The tuneability of these OPOs is realized by a rather slow adjustment of the spectral gain window by changing the orientation or the temperature of the nonlinear crystal (in the range of some tens of seconds). Consequently, scanning imaging application would suffer from this slow tuning speed.

The broadband phase-matched non-collinear optical parametric oscillator (NOPO) presented in this work, for the first time, combines the ultra-broadband phase-matching concept, as described in Sec. 2.2.1, with the novel ultrashort-pulse and high-power pump laser technology. These lasers, which are mainly based on the thin-disk concept, can nowadays reach output powers up to 275 W [Sar12a], moreover no fundamental physical limitation for a further power scaling has been reached yet. By using these thin-disk lasers as a pump source for the NOPO, the whole power scaling ability can be easily transferred by adapting the beam diameters, since within the transparency window of the chosen nonlinear crystal, there is almost no heat-load due to the parametric amplification process.

Furthermore, because of the wide spectral transmission of the used nonlinear crystal, the gain window of the NOPO is only limited by the non-collinear phase-matching bandwidth which can reach almost one optical octave. Following the well established concepts of octave spanning Ti:sapphire oscillators [Rau08, Bin10], by the use of ultra broadband chirped mirrors, the NOPO supports an ultra-broad spectral bandwidth.

Due to the instantaneous nature of the parametric gain the tuneability of such a broadband phase-matched system is then only limited by the mechanics which are used to realize a temporal or spectral filter within the oscillator. Since fast optomechanics, for example galvo scanners are already well established and a dynamic performance in the kHz-range is commercially available, this ultra-fast and widely tuneable NOPO is a novel and ideal tool suited for nonlinear spectroscopy [Hof13] with very high photon-flux and an outstanding fast tuneability [Lan12].

4.1.1 Theoretical considerations

Femtosecond non-collinear optical parametric oscillators are in many aspects quite similar to broadband ultra-fast Ti:sapphire laser oscillators. Thus, they have to provide the broadband resonator conditions, dispersion management, a mode-locking mechanism, and, a proper gain medium, which supports the necessary bandwidth for required pulse durations. Accordingly, the oscillator design of an ultra-broadband

phase-matched NOPO is based on a synchronously pumped Ti:sapphire laser system as demonstrated by Binhammer *et. al* [Bin10]. However, the most obvious difference between a laser oscillator and a fs-OPO is the principle used to provide the gain. The NOPO is based on the non-collinear parametric amplification concept as it is described and discussed in detail in the previous chapters. Due to the instantaneous parametric amplification process and the fact that no pump energy is stored in the crystal, a number of specific aspects need to be considered to understand the behaviour of the NOPO.

Ti:sapphire oscillators are typically pumped by cw-lasers, since the gain medium can be inverted and energy can be stored within a lifetime of several microseconds. As seen in the parametric amplification stages from the OPCPA systems, here high intensities ultra-short pump pulses are required since the parametric process shows a strong intensity dependency. In a parametric oscillator the resonant signal pulse needs to be temporally overlapped with these pump pulses for each round-trip. Consequently, the resonator length of the NOPO needs to be synchronized to the pump pulse repetition rate.

Furthermore, especially in case of the broadband phase-matched NOPO, the generated signal wavelength strongly depends on the internal dispersion management. This can be understood by considering a broadband superfluorescence which is generated within each pump pulse passing through the nonlinear crystal. Each of these superfluorescence pulses are generated with a random phase until a sufficient back coupling due to the resonator (gain exceeds the losses) will efficiently amplify and shape one of these pulses to a resonant signal pulse. The spectral width and phase of this resonant signal pulse will benefit the most from the gain window within the pump pulse duration after the relaxation time in the range of the photon life-time in the resonator. In other words, which specific spectral components are efficiently amplified for a certain pump pulse width and repetition rate, depends on the respective round-trip time of each color defined by the internal group delay dispersion and the current resonator length. Fig. 4.1 exemplarily illustrates this dependency with respect to the particular round-trip group delay given by the overall dispersion. Therefore, the relative group delays after one resonator round trip in the standing wave resonator are plotted. The calculation considers all dispersive elements in the resonator with respect to the experiment as presented in the next section: namely 33 mm of glass, 2 mm BBO-crystal and the 15 reflections on the negatively double-chirped ultra-broad mirror pairs.

Since this dependency is vital for the understanding of the NOPO behaviour it should be exemplarily illustrated for two different cases: the resonator lengths of

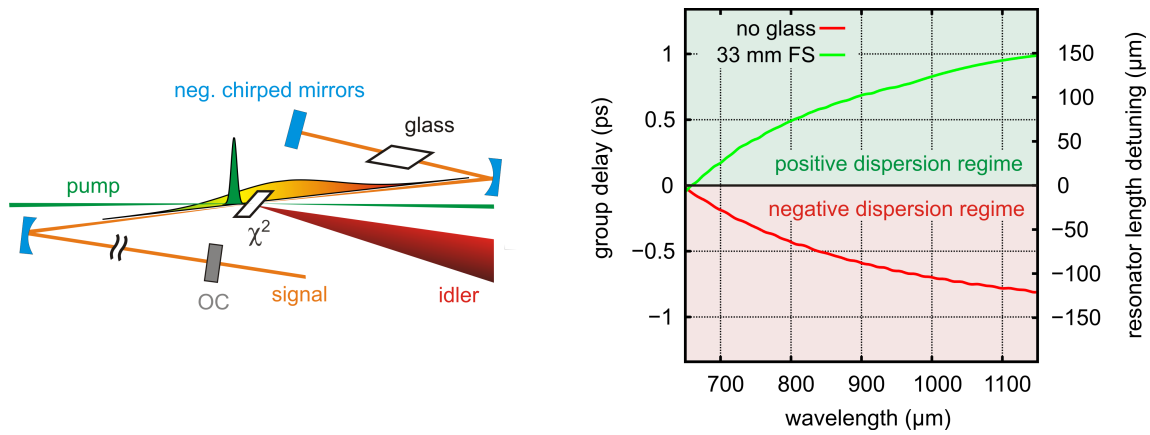


Figure 4.1: Simplified schematic of a synchronously pumped non-collinear optical parametric oscillator. **Left:** Schematic of the signal resonant oscillator with broadband negatively chirped mirrors, positive dispersive glass and the χ^2 -crystal. **Right:** Dependency between round-trip group delay dispersion and resonator length detuning for the synchronous operation of a certain wavelength. Due to the negative mirrors the oscillator without any glass operates in the negative dispersion regime.

both, the NOPO without additional glass, operating in a negative dispersion regime and the one with 33 mm of fused silica, are chosen so that the resonant signal pulses with a center wavelength of 650 nm are perfectly synchronized to the repetition rate of the pump laser. The respective group delay or the respective resonator detuning for other wavelengths in these two regimes are shown on the right hand side of Fig. 4.1.

For an efficient pulse amplification the signal and pump pulses need to overlap in time, so the signal pulse duration will be always adapted to the pump pulses. This means that shorter pump pulses or a higher dispersion can lead to a temporal overlap for a narrower signal wavelength range. For the pump durations of 500 fs, used in this work, it is therefore possible to tune the spectral width by adapting the internal dispersion as well as the center wavelength by changing the resonator length. Therefore, each wavelength with a certain group delay in the example in Fig. 4.1 is connected to a respective relative resonator length within the 500 fs gain window of the pump pulses in the example.

The pulsed pump and thereby the resulting gain provides an active mode-locking scheme which enables a stable signal pulse train under certain conditions. Since, the offered gain bandwidth supports much shorter pulses than the pump pulse duration, a spectral filter is required which is provided by the above described intra cavity dispersion. If the dispersion is lowered towards zero, chaotic pulsing can occur

which will be discussed in detail in Sec. 4.1.3. For negative dispersion also a soliton-like pulse formation is possible which is not discussed in the framework of this thesis. Fig. 4.2 schematically visualizes this chaotic pulse formation, from a clean dispersively stretched pulse to a pulse-burst like operation, over several round-trips in a NOPO with a broadband dispersion compensation and no further stabilization mechanism.

Since the clean pulse in Fig. 4.2(a) will not see a dispersive change during the first round trips, it can be efficiently amplified by the broadband parametric gain in the nonlinear crystal. Due to unavoidable inhomogeneities, e.g. the remaining oscillations in the reflectivity and phase of the resonator mirrors or the pump pulse depletion, the temporal and spectral intensity distribution of the formerly clean pulse will change after several round-trips. Subsequently, as shown in the figures (b) and (c), due to the coupling between the parametric gain and the present spatiotemporal intensity distribution as described in Sec. 2.2.3, these inhomogeneities are amplified by the parametric process which will lead to a burst-like chaotic pulse formation.

Last but not least, the two nonlinear geometries TPG and PVWC differ in terms of spatial overlap between pump, signal and idler pulses and regarding the parasitic conversion processes during the parametric amplification. All these effects, as described in detail in the previous chapters, also take place during the parametric amplification process in a NOPO. Consequently, the same variety of spectral, spatiotemporal interactions and dependencies can be observed in NOPOs as well.

The following sections will show the experimental conditions and discuss the results of the NOPO realized in this work. The system will be fully characterized and the differences in the tuneability and output power between the different non-collinear geometries will be discussed.

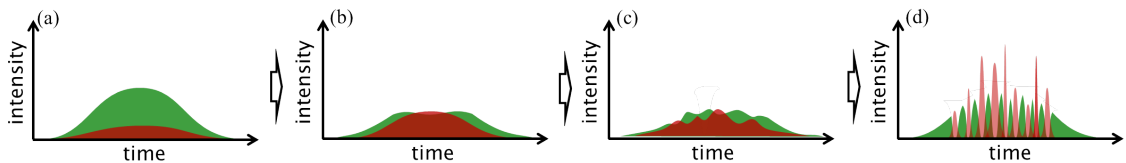


Figure 4.2: Illustration of the chaotic pulse formation in a broadly phase-matched NOPO without sufficient positive dispersion.

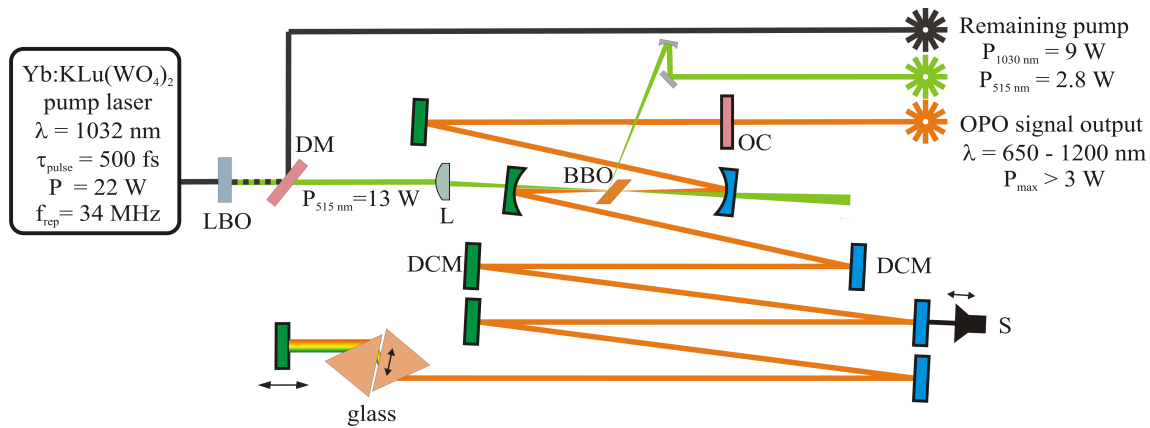


Figure 4.3: Schematic of the widely tuneable NOPO setup pumped by 13 W of the frequency doubled thin-disk laser system [Pal08]. The NOPO consists of the BBO: nonlinear crystal (2 mm), DCM: double-chirped mirror pairs, glass: fused silica or LaK₈-prism pair, L: focusing lens ($f=60$ mm), LBO: SHG crystal (1.6 mm), OC: output coupler ($T=15\%$), and S: rapidly movable translation stage.

4.1.2 Experimental setup

The NOPO is schematically illustrated in Fig. 4.3. The ultra-broadband non-collinear amplification scheme (see Sec. 2.2.1) can either be realized in TPG or PVWC-geometry. For pumping the system, a home-built frequency doubled Yb:KLu(WO₄)₂ thin-disk laser oscillator is used [Pal08]. This pump laser, operating at the fundamental wavelength of 1030 nm, delivers 22 W of average output power with a repetition rate of 34 MHz, which corresponds to a pulse energy of 0.6 μ J. By focusing the pump light with a 60 mm lens in a 1.6 mm long LBO-crystal, the second harmonic of the 500 fs fundamental pulses is generated with more than 60% conversion efficiency. The remaining 9 W of the fundamental radiation after the SHG is separated by a dichroic mirror and can be used as an optically synchronized additional pulsed light source for the application, e.g. SARS [Hof13].

After the dichroic mirror, 13 W of green power are available to pump the nonlinear process in a 2 mm BBO crystal in the NOPO. Therefore, the pump beam is tightly focused down to about 50 μ m by a 60 mm lens and passes through one of the focusing mirrors from the oscillator. Thus, one side of the used chirped mirror pairs show a high transmittance at the pumping window of 515 nm. Due to the tight focus on the crystal surface, the achieved peak intensity of more than 100 GW/cm² exceeds the damage threshold of any broadband anti-reflection coating; so the crystal is placed in a Brewster angle to avoid the Fresnel reflection of the oscillator mode. Although

the internal losses of the resonant signal pulse are minimized, this Brewster angle causes higher losses for the orthogonally polarized extraordinary pump pulses. Thus, the strong Fresnel reflection of 21.6% at the crystal entrance surface could be used as an additional output beam with a pulse duration of about 350 fs and more than 2.8 W of power for the intended application.

The signal-resonant ultra-broadband oscillator is realized by folding a 4.3 m long standing-wave resonator under the use of negative dispersive double-chirped mirror pairs (DCM) spanning from 600 nm to 1200 nm. The two focusing mirrors with 100 mm radius of curvature are set at an angle of incidence of 5° which compensates for the astigmatism introduced by the 2 mm BBO-crystal. Furthermore, the mirror pairs are designed in such a way that the remaining oscillations in the group delay dispersion, despite the impedance matching of the broadband chirped coating layers, respectively compensate each other's oscillations, resulting in a negative and flat dispersion curve [Kae01]. For the experimental results as discussed in the next sections, two slightly different experimental setups are realized. The only difference is given by the geometry of the optical path and the number of reflections on the DCMs. However, since this change does not influence the results and conclusions, which are presented in the following, only one setup is shown here. For the sake of completeness, it should be mentioned that for the results presented in Sec. 4.1.3 17 reflections on the DCMs were realized, as shown in Fig. 4.3. For the results presented in the next section one folding mirror was removed which results in only 15 reflections. However, in both setups the negative second and third order dispersion (GDD, TOD) can overcompensate the positive GDD and TOD introduced by the BBO-crystal. In Fig. 4.4 the wavelength resolved internal net dispersion, with 15 reflections on the DCMs, double pass through the 2 mm BBO and different amounts of glass for each round-trip is plotted. By adding positive dispersion, e.g. fused silica or the LaK₈ prism pair, the average internal net dispersion can be set continuously from slightly negative values around -400 fs^2 up to more than 5000 fs^2 at 800 nm. However, it can also be clearly seen that there are residual oscillations of the DCMs which become significant for the NOPO for a small amount of glass as well as for longer wavelengths due to the uncompensated third order dispersion.

As it will be shown in the next sections, these oscillations in the GDD, especially for small net dispersion values, cause the NOPO to have a sensitive behaviour, regarding a resonator length detuning with respect to the pump repetition rate. Thus, to guarantee a stable operation in terms of output power and wavelength, the synchronously pumped NOPO needs to be actively stabilized in length to the respective repetition rate of the pump laser. Therefore, the spectrum, measured

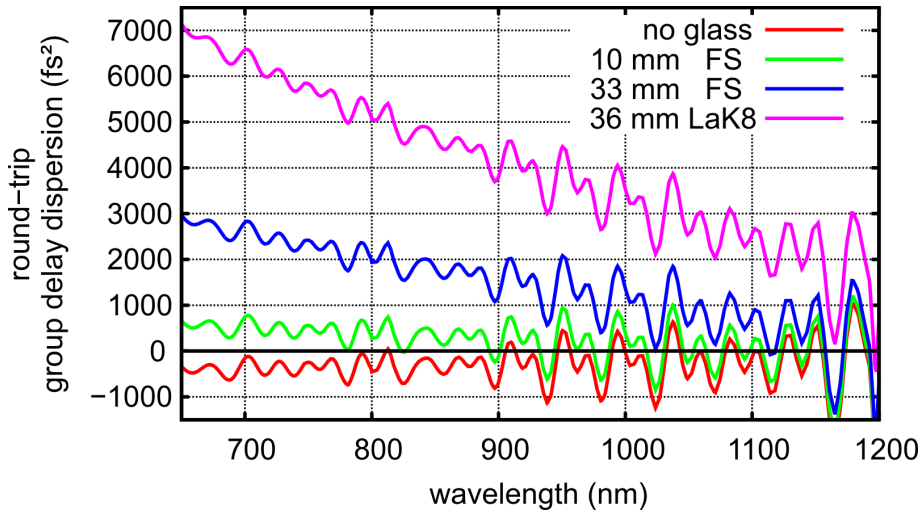


Figure 4.4: Calculated internal net dispersion for the double pass through different amounts of glass in the NOPO under consideration of 15 reflections on DCMs and the double pass in the 2 mm BBO-crystal.

by a grating spectrometer (Ocean Optics USB4000), is analyzed by a self-written computer code to actively compensate the thermal drifts of the resonator length with sub-wavelength step sizes by a controlled piezo stepper stage at one of the mirrors. Since this stepper is slow, for a fast sweeping of the resonator length, an additional loudspeaker is attached to a linear translation stage for a rapid movement of one of the folding mirrors. For stability reasons and to avoid contamination of the strong hygroscopic nonlinear crystals, the whole system is housed in a box, which is continuously flushed with dry air.

At this point the overall output performance in terms of power scalability, beam quality and long-term stability shall be shown in order to motivate and justify a closer and detailed investigation of the NOPO in the next sections.

By using a 15% output coupler mirror, a maximum output power could be scaled to more than 3 W. Thereby, as explained above, the NOPO is further scalable just by applying a stronger pump and adapting the pump waist. As shown in Fig. 4.5 (a), by locking the 70th harmonic of the repetition rate of the thin-disk laser oscillator to a 2.4 GHz RF signal generator, the NOPO in the presented experimental design shows an excellent long-term stability. The figure also shows the M^2 -measurement of the close to diffraction limited Gaussian signal beam. Furthermore, the optical pump-synchronized signal pulses are tuneable from 650 up to 1200 nm just by changing the resonator length very quickly, which will be discussed later in more detail. This specification already marks a significant milestone, especially regarding the tuning

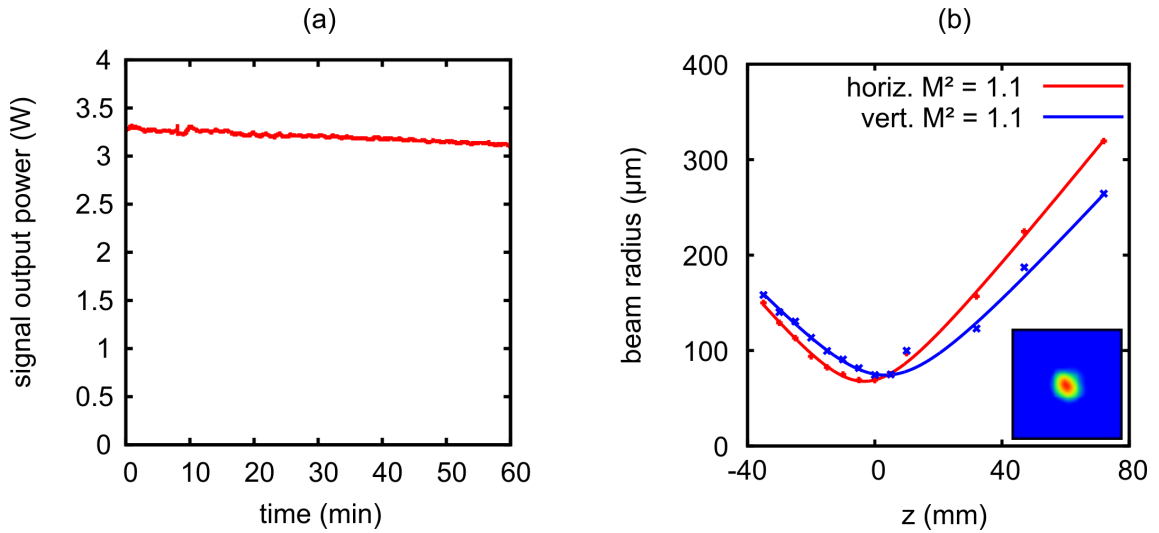


Figure 4.5: (a) Long-term stability of the NOPO signal output power. The pump thin disk laser was running with an actively controlled repetition frequency. The drop in the signal output power is related to the pump power. (b) M^2 -measurement of the signal output pulses.

performance and output power of state-of-the-art tuneable Ti:sapphire oscillators as mentioned above.

However, as observed for the parametric process in previously investigated OPC-PAs, also the NOPO can show complicated spatiotemporal and parasitic effects. Thus, the stability as well as the spectral bandwidth of the NOPO-output strongly depends on the internal dispersion. Furthermore, additional effects could be observed which can be addressed to parasitic nonlinear effects, especially in the PVWC-geometry. Moreover, the remaining spectral oscillation of the GDD from the DCMs can be clearly seen by analyzing the dependency between output spectrum and resonator-pump detuning. The next section presents a careful characterization of the performance of the system for different values of the resonator dispersion as well as non-collinear geometries and a discussion of the results regarding the output power, tuneability and stability.

4.1.3 Experimental results and discussion

Efficiency, output performance and first characterization of the NOPO

For a systematic characterization, the NOPO was first realized in the positive dispersion regime in the PVWC-geometry. Because of the excellent overlap of the signal oscillator mode with the 10 W pump beam in the BBO-crystal, more than 3 W of

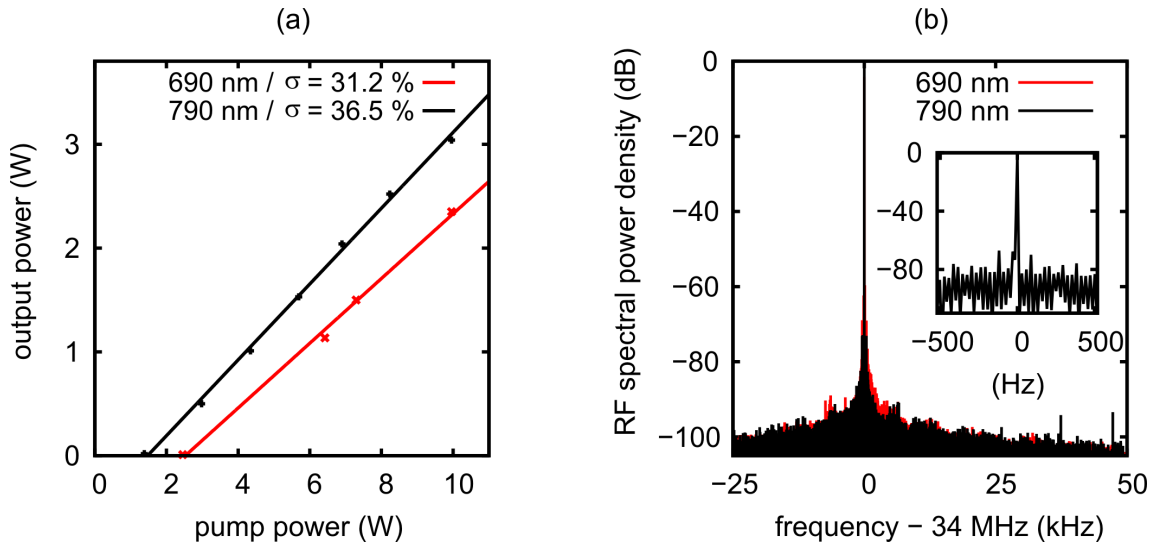


Figure 4.6: (a) NOPO signal output power vs. pump power (corrected for the 21.6% reflection losses) for two different signal wavelengths. (b) Radio-frequency analysis of the fundamental repetition frequency for two different signal wavelengths with 10 Hz resolution. The inset shows the zoom for 780 nm with 1 Hz resolution.

output power could be achieved. Considering of the Manley-Rowe relations [Man56] between the generated signal and idler photons at each round-trip, the 3 W of signal output power at 790 nm goes along with the generation of 1.6 W of idler power at 1.5 μm . This results in a total photon efficiency of 45%. The respective power slopes for two center wavelengths, with a slope efficiency of 36.5% at 790 nm (black curve) and 31.2% at 690 nm (red curve), are shown in Fig. 4.6 (a). The slight drop of the efficiency for the shorter wavelength can be mainly attributed to the higher non-collinear angle of the corresponding idler spectral components (as explained in Sec. 2.2.2). Also, the phase-matched angles of the signal spectral components below 700 nm start to deviate slightly from the "magic-angle" of 2.5° (as explained in Sec. 2.2.1). However, with an average internal dispersion of $\sim 400 \text{ fs}^2$, using 10 mm of fused silica, the two different output wavelengths could be obtained without any realignment just by a slight change of about 30 μm in the resonator length.

In order to ensure stable pulsing, a measurement of the radio-frequency spectrum with a bandwidth up to 25 GHz has been performed. Fig. 4.6(b) shows the RF-spectrum of the fundamental repetition rate of the output pulse train for a stable operation at the two different output signal wavelengths, respectively. The inset shows a zoom with 1 Hz resolution. More than 80 dB of noise suppression verify the stable operation.

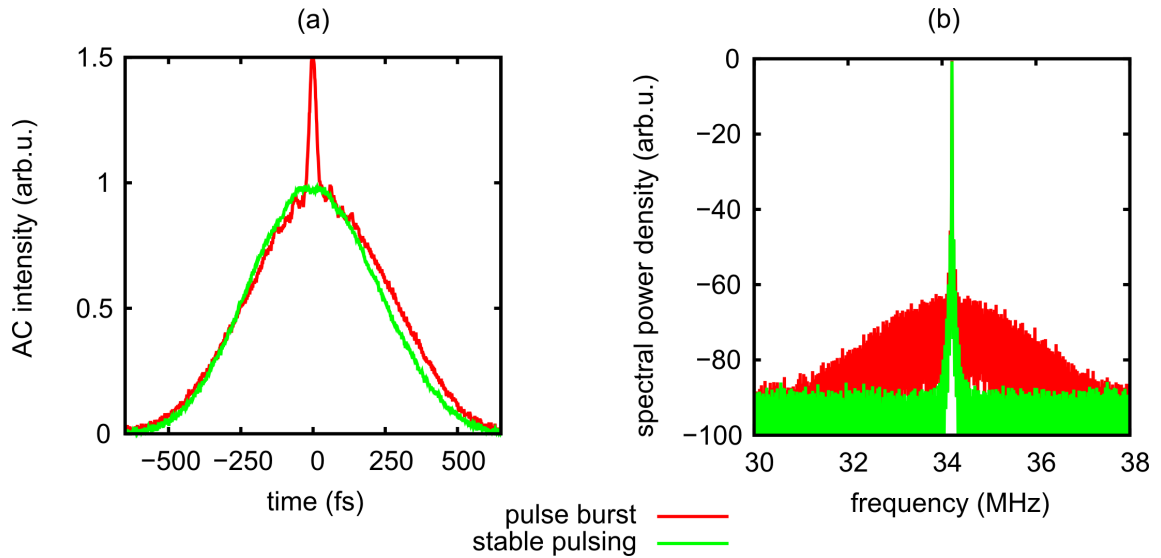


Figure 4.7: Identification of stable and unstable operation by using 10 mm fused silica in the resonator: (a) Intensity autocorrelation (IAC) with coherence-spike-on-a-pedestal shape (red) indicates a "pulse-burst"-like operation in contrast to the clean green IAC-trace. (b) Radio-frequency analysis of the fundamental repetition frequency under stable (green) and unstable (red) conditions.

As explained in Sec. 4.1.1, due to the instantaneous gain an active mode-locking is initiated and a stable pulse train is impressed. However, the mode-locking dynamics and thus the output performance of the NOPO strongly depends on the resonator length and the amount of glass used in the oscillator. Furthermore, because of the ultra-broad gain-bandwidth, supporting a few-cycle pulse dynamics, the narrow-band pulse formation of the resonant signal pulse in the oscillator can be rather complicated. Especially for an average internal net dispersion smaller than the remaining oscillations of the GDD (see Fig. 4.4) the output is very sensitive to any detuning of the resonator. In this regime a chaotic, or irregular operation, e.g. bifurcations or higher order solutions, can occur for certain resonator lengths, although for other resonator lengths the operation is stable.

Nevertheless, the unstable operation as explained in Sec. 4.1.1, can be clearly distinguished from a clean stable operation mode by the observation of the intensity autocorrelation as shown in Fig. 4.7 (a), where a chaotic unstable pulse dynamic is clearly visible by the occurrence of a coherence-spike³ which emerges on top of the pedestal. Since this unstable pulsing can be described as time-dependent phase fluc-

³As a pulse increases in complexity, the autocorrelation approaches a coherence-spike-on-a-pedestal shape, independent of the pulse intensity structure [Tre01].

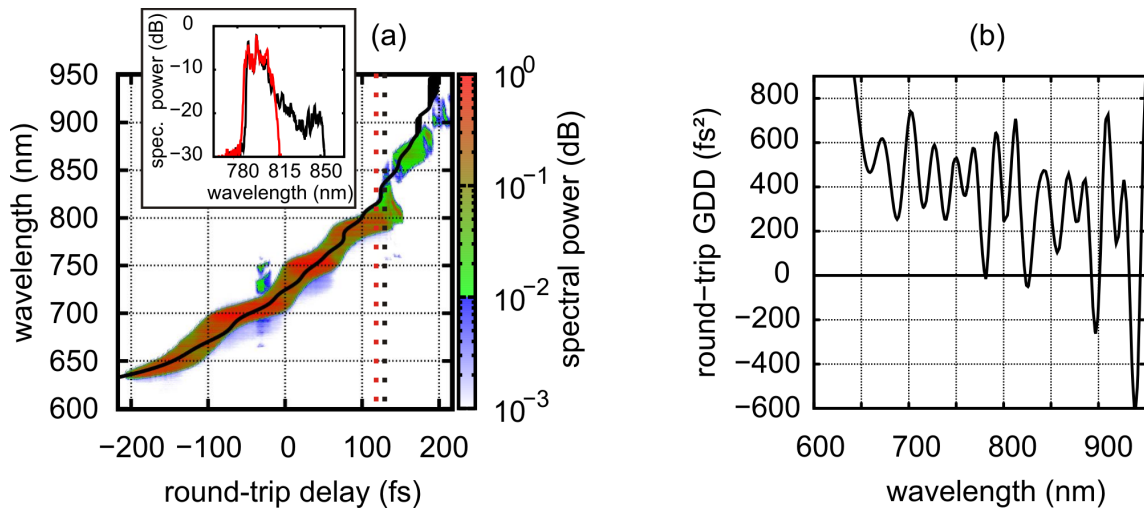


Figure 4.8: NOPO tuning behaviour with moderate dispersion. (a) A series of spectra taken by an Ocean Optics spectrometer (USB4000) for different resonator lengths are mapped over the respective round-trip time delay; inset: two exemplary spectra for different round-trip delays (red and black dotted lines); (b) The round-trip group delay modeled under consideration of the round-trip dispersion of 2 mm BBO, 10 mm fused silica and the used double-chirped mirrors (DCMs) (black curve) and the round-trip group delay dispersion under the same conditions.

tuations within the spectral modes, a corresponding increased noise floor is clearly visible in the RF-spectrum depicted in Fig. 4.7 (b).

In order to investigate the origin of these instabilities, the output characteristic of the NOPO was studied for comprehensive series of operating resonator lengths. In Fig. 4.8 (a) a series of measured signal output spectra is mapped, each one for a specific resonator length corresponding to a different round-trip time delay. The modeled round-trip group delay, plotted by the black curve in (a), considers 15 reflections on the used DCMs, the 2 mm BBO and 10 mm of fused silica. The respective theoretical group delay dispersion accumulated at each round-trip is shown on the right hand side in (b). It can be seen that for the chosen amount of glass, the output spectrum of the NOPO can be tuned continuously from 650 nm up to 850 nm. At 850 nm and beyond 900 nm, however, discontinuities can be clearly observed, which are associated with the mentioned unstable pulsing behaviour. By comparing the shown tuning curve with the wavelength resolved round-trip group delay dispersion, it is obvious that this behaviour sets in for wavelengths where the GDD-values become close to zero. Note, that the modeled GDD round-trip dispersion, shown in Fig. 4.8 (b), allows only for a qualitative statement about the position and height of the shown ripples, since they are based on the design curves of the used DCMs. Fur-

thermore, as extensively discussed in the previous chapters, at the examples of the presented OPA-simulations⁴, it also needs to be taken into account that, in the used PVWC-geometry, the parasitic second harmonic generation takes place at around 860 nm. Thus, an additional, strong, positive and negative contribution of the parametric group delay dispersion in this region is to be expected. Despite the dispersive ripples due to the DCMs, mainly the negative parametric contributions lead to the observed pulsing instabilities which can be addressed to a self-compression and a higher order soliton formation of the corresponding spectral components.

Consequently, to ensure a stable pulsing behaviour, a careful dispersion management needs to be considered which depends on the particular requirements regarding the tuneability, the spectral bandwidth and the pulse duration out of the system. In order to characterize the NOPO for a wider continuous tuning behaviour and to identify the limits regarding the generation of the shortest possible pulses, a parameter study with different internal dispersion values has been performed.

NOPO pulsing behaviour and spectral bandwidth in different internal net dispersion regimes

As already indicated by the experimental results with an internal net dispersion of about 400 fs², the NOPO shows strong differences in the output performance only by changing the resonator length. Whereas for resonator lengths leading to wavelengths shorter than 850 nm a stable operation with a well defined tuning behaviour was observed, a more complicated pulsing behaviour was identified for wavelengths beyond 850 nm. This "unstable regime" could be mainly attributed to an interplay between linear and nonlinear effects. The linear effect is caused by the decreasing dispersion due to the high TOD of the used glass. Under the use of 10 mm fused silica, the internal net dispersion falls short the remaining dispersive ripples of the DCMs for wavelength beyond 850 nm. On the other hand, the nonlinear effect is caused by phase contributions from the poorly phase-matched parasitic SHG for signal wavelengths around 860 nm. Not as obvious, also the nonlinear phase contributions of the broadband idler SHG, which are coupled back by the DFG to the signal phase between 780 nm and 950 nm, influence the spectral bandwidth and phase. Conse-

⁴The interested reader shall find the measured and simulated parametric group delay in Fig. 3.8 (a) showing a similar behaviour in a NOPA-system. The derivative of each curve is the respective spectrally resolved parametric GDD. This quite close example indicates that, around the parasitic SHG-phase-matched wavelength of 860 nm, a strong parametric contribution of the group delay dispersion can be expected in the NOPO as well - strongly negative before and strongly positive beyond 860 nm respectively. This can explain the relatively broad spectrum for a round-trip delay of 140 fs in Fig. 4.8 (a) compared to the smaller spectral bandwidth for center wavelengths between 860 nm and 900 nm which are similar to the behaviour below 800 nm.

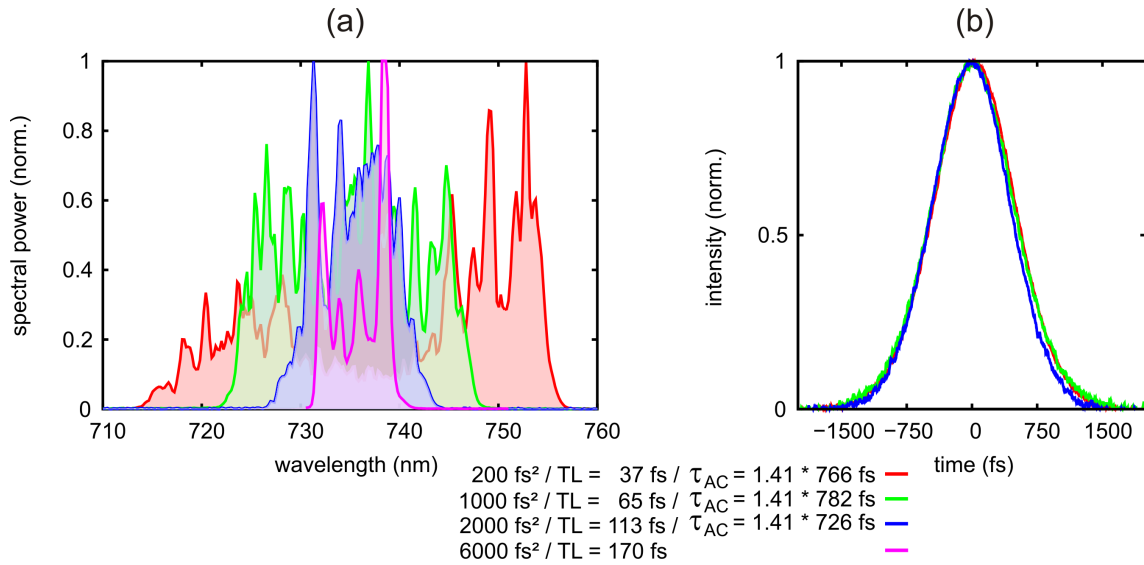


Figure 4.9: (a) NOPO output spectra for different amounts of glass: fused silica (6.4 mm (red), 16 mm (green), 28.3 mm (blue)) and LaK8 36 mm (purple), TL: transform limited pulse duration; (b) Corresponding uncompressed intensity autocorrelation trace.

quently, the wavelength range of the NOPO, which shows a stable positive dispersive pulsing, depends on the significance of the mentioned effects compared to the first and second order total internal dispersion for a given amount of glass.

To understand the influences of the dispersion to the pulse forming dynamics in the NOPO without strong influences of the above mentioned linear and nonlinear effects, the following considerations shall be restricted to a spectral range below 850 nm. As it can be seen in Fig. 4.9 (b), in this spectral range even a strong variation of the internal dispersion value from 200 fs^2 to 6000 fs^2 shows no significant change in the pulse duration of the NOPO-output. This can be understood by the instantaneous gain window defined by the pump pulses as explained in Sec. 4.1. In contrast to this uncompressed pulse duration, the spectral bandwidth of the different NOPO-output spectra, as illustrated in Fig. 4.9 (a), obviously becomes broader for less internal dispersion. Notwithstanding, the NOPO has shown a stable pulsing behaviour for the measured spectra plotted in Fig. 4.9 (a), this was not the case for the broadest spectra close to the zero-dispersion, which are not shown here. For this unstable pulsing of the zero-dispersive NOPO spectra of more than 100 nm could be generated. However, the shortest stable pulses from the presented NOPO could be measured with an internal dispersion of 200 fs^2 similar to the red spectrum in Fig. 4.9 (a) for a slightly different center wavelength of about 780 nm, with a compressed pulse duration of 39 fs. The compression was done by a SF10-prism sequence with an

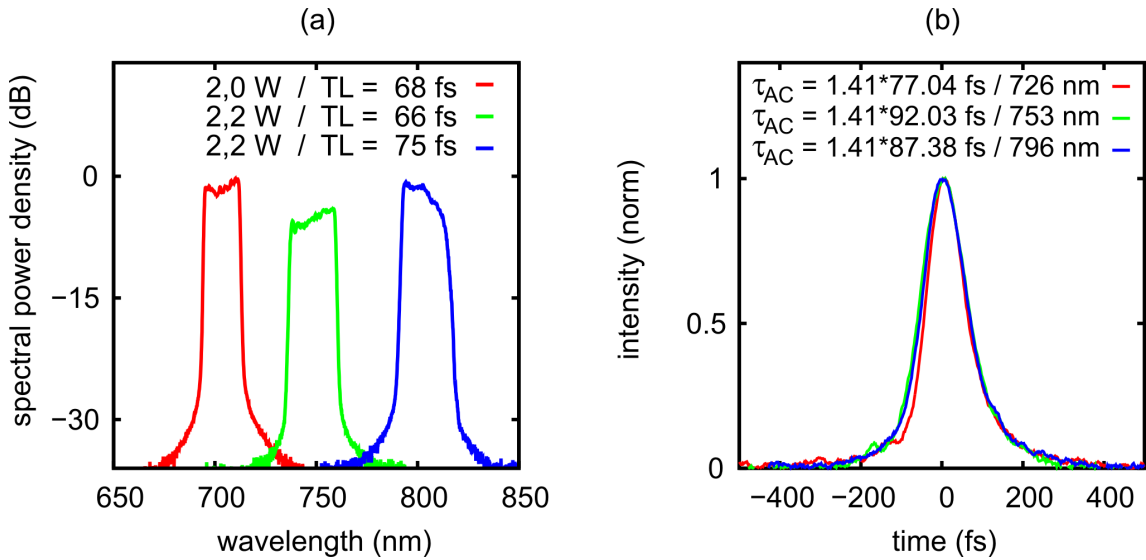


Figure 4.10: (a) Selected continuously tuneable signal spectra by varying the resonator length. The inset shows the calculated Fourier limit and optimized average output power, respectively. (b) Intensity autocorrelation traces of the compressed pulses corresponding to the spectra shown in (a).

apex distance of 70 cm, and the pulses were measured by an SHG-FROG showing a good agreement between measured and the retrieved FROG-images⁵. However, due to the discrepancy between the long pump pulses and the short transform limit of this pulses, the active mode-locking caused by the instantaneous gain is quite weak. Consequently, the NOPO with this small internal dispersion is extremely sensitive to the resonator length and shows only a stable behaviour for very selected center wavelengths. Thus, this marks the limit of the NOPO in terms of the shortest pulses for the setup presented here without an additional mode-locking mechanism. For the generation of shorter pulses the reader is referred to Sec. 4.2.

Although it turned out that with the NOPO in the presented design the goal of the generation of sub-10 fs pulses can not be realized, by increasing the dispersion to 1000 fs^2 a clean tuning behaviour over a wide range from 650 nm to 850 nm has been obtained with a moderate spectral bandwidth. The measured spectra with different center wavelengths and a transform limited pulse duration smaller than 80 fs are shown in Fig. 4.10 (a). For each center wavelength the pulses could be compressed by a SF10 prism sequence to sub-80 fs as shown by the autocorrelation traces in (b). By doubling the dispersion to 2000 fs^2 , the spectrum narrows further with a comparable factor from 24 nm down to 13 nm. However, a further strong increase of

⁵Note, a strong remaining TOD was observed which could be mainly attributed to the compressor itself.

the dispersion, three times larger than before, to 6000 fs^2 , only narrows the spectral width from 13 nm to 8 nm. This effect can be mainly attributed to the spectral broadening driven by the self-phase modulation caused by the enormous intensities in the BBO-crystal. As shown later in Fig. 4.12 (b), by reducing the NOPO output power the spectral bandwidth can be further reduced down to 1.8 nm. The transform limited pulse duration of these pulses with 300 fs is already in the range of the temporal amplification window defined by the pump pulse duration.

In summary, the study of the NOPO with a wide range of different internal dispersion values could mark an upper and a lower limit of the possible signal pulse duration under stable conditions. The lower limit in a spectral region with no parasitic effects and small oscillations of the DCM-dispersion could be found with an internal dispersion of 200 fs^2 and pulse duration of about 40 fs. The limiting factor at this point is the strength of the active mode-locking mechanism given by the duration of the pump pulses. The same is true for the upper limit, which was found to be caused by both the duration of the pump gain window and by the spectral broadening due to SPM for higher output powers.

Consequently, there are only two possibilities to push the lower limit. Either to shorten the pump pulse duration or to implement an additional fast mode-locking mechanism. To realize the one or the other is quite challenging and makes it necessary to modify the experimental design either of the NOPO (see. Sec. 4.2) or the pump laser.

On the other hand, pushing the limit regarding the spectral resolution of the NOPO is relatively straight forward. Nevertheless under the presented conditions, 500 fs pump pulses and high internal net dispersion, the NOPO shows very useful results. Especially for applications which benefit from the spectral resolution, the highly dispersive and tuneable NOPO is a powerful tool. Therefore in the next section, the tuneability of the NOPO in the whole phase-matched gain bandwidth shall be closer analyzed.

Tuneability of a highly dispersive NOPO

In this paragraph, the NOPO tuning behaviour in the PVWC-geometry for different amounts and types of glass in the oscillator is discussed. Fig. 4.11 (a) shows an overview of the tuning curves with respect to the resonator-length-detuning as described in Sec. 4.1.1. Therefore, each curve represents an extensive series of measurements for different resonator lengths, showing the spectral power density on a logarithmic scale indicated by the color map. The respective theoretical tuning curve, calculated by the modeled group delay (explained in Sec. 4.1.1), is plotted

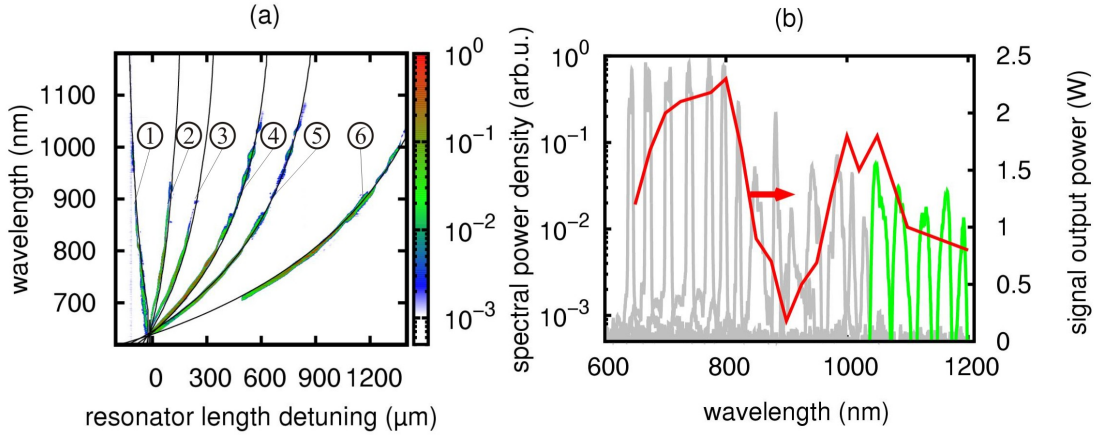


Figure 4.11: Tuneability of the signal wavelength by changing the resonator length of the NOPO without any realignment. (a) Signal spectra for different amounts of internal net dispersion. The black curves reveal the calculated internal group delay (1) -800 fs^2 no glass, (2) 800 fs^2 FS, (3) 2000 fs^2 FS, (4) 2000 fs^2 LaK8, (5) 3500 fs^2 LaK8, (6) 5000 fs^2 LaK8 - approximate values at 800 nm (b) Signal spectra of curve (4) measured by a CCD based spectrometer (grey) and a scanning spectrometer (green) and the corresponding signal output power (red curve).

by the black solid line. This procedure is done in the negative dispersion regime without any additional glass in the resonator, and for a wide range in the positive dispersion: 800 fs^2 and 2000 fs^2 of internal dispersion realized by introducing fused silica plates and 2000 fs^2 , 3500 fs^2 and 5000 fs^2 set using LaK8 material.

It can be seen, that for all measurements the calculated tuning curves are confirmed. However, as it was shown before in Sec. 4.1.3, for fused silica with a moderate net dispersion, no wavelength beyond the parasitic gap around 900 nm can be addressed. In contrast, by using LaK8, which shows a higher zero-dispersion value for internal net dispersion above 2000 fs^2 , the tuning range enlarges across the whole phase-matched spectral width up to 1200 nm . Even though, for the highest amount of glass, a gap around the parasitic-SHG phase-matched wavelengths can be observed in the PVWC-geometry. This phenomenon can be seen more clearly in the measured NOPO output power while tuning (red solid) and in a series of selected output spectra in Fig. 4.11 (b). The spectra shown by the grey solid lines are cross sections from curve (4) with spectral widths of approximately 20 nm for a center wavelength smaller than 800 nm . Since the sensitivity of the used CCD based spectrometer at longer wavelengths is very low, spectra beyond $1 \mu\text{m}$ are measured by a scanning spectrometer (green solid).

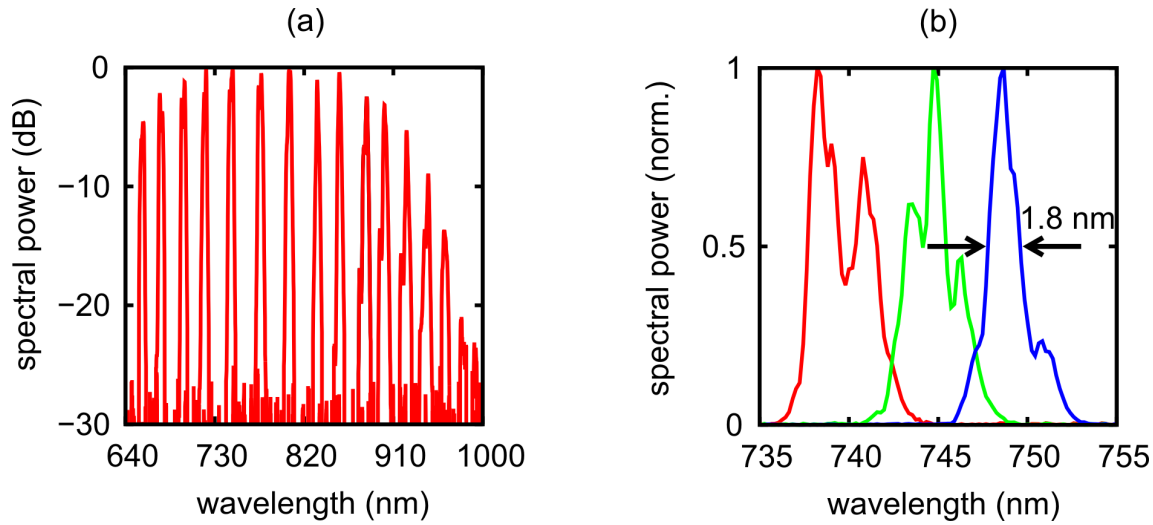


Figure 4.12: PVWC-NOPO optimized for wide and smoothed spectral tuneability with 36 mm of LaK8 and at lower output powers around 1 W: (a) Signal spectra for different resonator lengths measured by a CCD based spectrometer. (b) Zoom of three picked spectra showing the spectral bandwidth.

In order to fully exploit the limits in terms of the smoothest and mostly narrow-band tuneability in the presented experimental setup, the phase-matching angle was slightly adapted to shift the gap to longer wavelengths beyond 900 nm. Together with the use of 36 mm of LaK8, which shows a higher zero-dispersion wavelength, the spectral tuning range under clean pulsing conditions could be enlarged from 640 nm up to 950 nm as shown in Fig. 4.12 (a). Furthermore, to avoid spectral broadening due to self-phase modulation, the output power has been restricted to 1 W which results in the smallest spectral resolution of 1.8 nm, as shown in Fig. 4.12 (b).

NOPO dynamics and fast spectral ramping

As already mentioned, the presented large tuning range is achieved just by a detuning of the resonator via a linear translation at one of the folding mirrors. This is possible without the necessity of any realignment of the resonator or slow adaption of the phase matching angle due to the use of the broadband non-collinear phase-matching concept. Furthermore, because of the absence of any long-term memory in the nonlinear crystal, in contrast to the relatively long relaxation times in lasers, the system allows a high speed sweeping of the central wavelength. Because of the short photon lifetime in the oscillator of about 0.15 μs , the tuning speed is mainly⁶

⁶Although, for the given experimental setup, the life-time of a photon can be calculated to correspond to approximately 6 round-trips. Preliminary simulation results have shown that for a stable pulsing the NOPO usually reaches a steady state after approximately 50 round-trips.

restricted by the achievable mechanical movement. Since, as discussed above, a high internal dispersion is crucial for the widest and most narrowband tuning behaviour, the necessary resonator length detuning by the movement of one folding mirror is roughly half a millimeter. However, by using a state-of-the-art galvo scanner a fast tuning over the whole spectral range in the kHz-range is feasible.

For a first proof of these theoretical considerations, a high speed sweeping of the NOPO output center wavelength has been performed, by using a standard translation stage connected to a simple mid-range loudspeaker. Limited by the spring-mass system the loudspeaker could be driven up to 1 kHz. By doing so no indications of detrimental influence on the NOPO-dynamics could be observed. However, to show a wide wavelength sweep over the full tuning range the sweeping frequency was reduced. The left hand side of Fig. 4.13 (a) shows a stroboscopic spectral measurement with a CCD based spectrometer. This was necessary since the computational data acquisition of the spectrometer is not fast enough to temporally resolve the change of the NOPO output spectra in real-time. Nevertheless, the hardware read-out of the CCD-chip of the camera, which was set to the smallest possible integration time of approximately 1 μ s, is clocked much faster with 131.6 Hz. Therefore, in order to realize a very slow beating between this read-out frequency and the frequency of the NOPO wavelength ramping as well as to ensure the 1 mm resonator detuning, the frequency of the loudspeaker was set to 65.8 Hz. Since the NOPO wavelength ramping corresponds to just half of the frequency of the data read-out from the CCD for each subsequent read-out, every 7.6 ms the center wavelength of the NOPO is ramped one-time over the full spectral tuning range. Consequently, similar to the Nyquist-Shannon sampling theorem an artificial duplicate of each measured spectrum is visible, which is shifted about half a period. Furthermore, since the loudspeaker movement can be assumed to be sinusoidal, the observed unsymmetrical tuning curve indicates the different tuning speed for long and short wavelengths due to the uncompensated TOD in the NOPO. However, the measurement shows a very smooth spectral shift between 650 nm and 950 nm within 7.6 ms which corresponds to an average tuning speed of 40 nm/ms. This number clearly tops the fastest tuneable Ti:sapphire oscillator with a similar tuning range. As mentioned above, the limits regarding the NOPO-dynamics lay in the order of 50 round-trips for the relaxation of the signal pulse which corresponds to a time of 1.5 μ s. Therefore, new concepts to push the limit of the mechanical movement of the resonator length are currently under investigation. However, for using the NOPO in ultra-fast pump-probe experiments the temporal timing jitter of the signal pulse while the rapid ramping of their wavelength is important, too. Since the NOPO is intrinsically optically synchronized

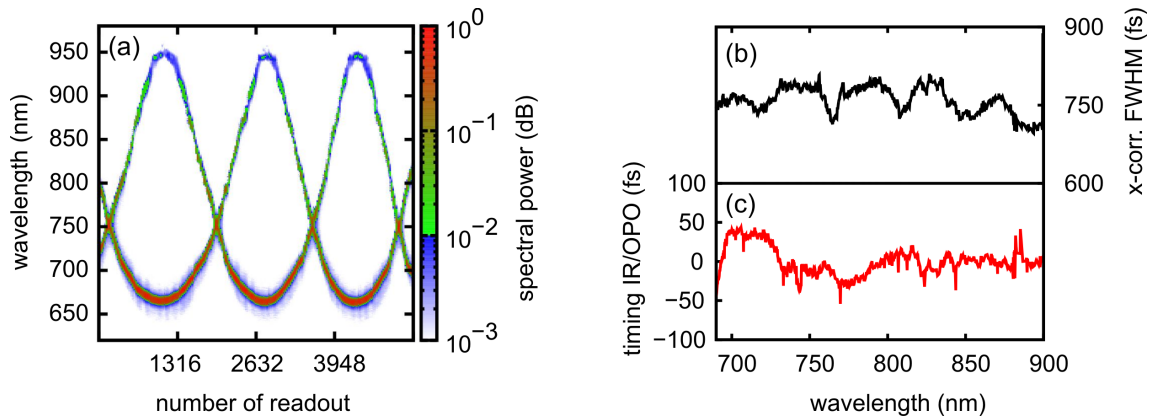


Figure 4.13: (a) 2D-mapping of a stroboscopic spectral measurement of the NOPO output pulses while spectral ramping with 65.8 Hz between 650 nm and 950 nm. The readout of the CCD-based spectrometer is clocked with 131.6 Hz leading to the artificial additional tuning curve; Cross-correlation trace (b) and the relative timing (c) between the tuneable NOPO output pulses and the fundamental IR-pulses (see Fig. 4.3).

with the fundamental and the second harmonic pump pulse train no additional effort needs to be taken into account for the temporal overlap between the pulses.

As illustrated in Fig. 4.3, the NOPO provides two more optically synchronized outputs, the pass-through of the remaining 9 W of the transform limited 500 fs fundamental IR-beam from the thin-disk pump laser and the 2.8 W Fresnel reflection of the frequency doubled NOPO pump pulses. As mentioned above, the NOPO shows the outstanding feature that the timing of the signal pulse train out of the NOPO is fixed to the timing of these pump pulses even while quickly changing the center wavelength by a rapid detuning of the resonator length. Fig. 4.13 (b) shows the temporal width of the cross-correlation measurements between the fundamental IR-pulses and the NOPO-output while tuning from 680 nm to 900 nm. Furthermore, the position of the cross-correlation traces, with respect to the known difference of optical paths, depends on the current timing jitter of the NOPO pulse trains. As shown in Fig. 4.13 (c), this position can be mapped to a relative timing between the fundamental IR pulse train as provided by the pump laser and the NOPO output pulses while tuning. Considering the cross-correlation width of about 750 fs as indicated in (b), the timing jitter of about 55 fs (rms) between the two pulse trains even while tuning the NOPO over a wide range is very low.

The three narrowband pulse trains, at 515 nm, 1030 nm and quickly tuneable between 650 nm and 950 nm, provided from the highly dispersive NOPO with a fixed timing to each other, are ideally suited for spectroscopic pump-probe-experiments.

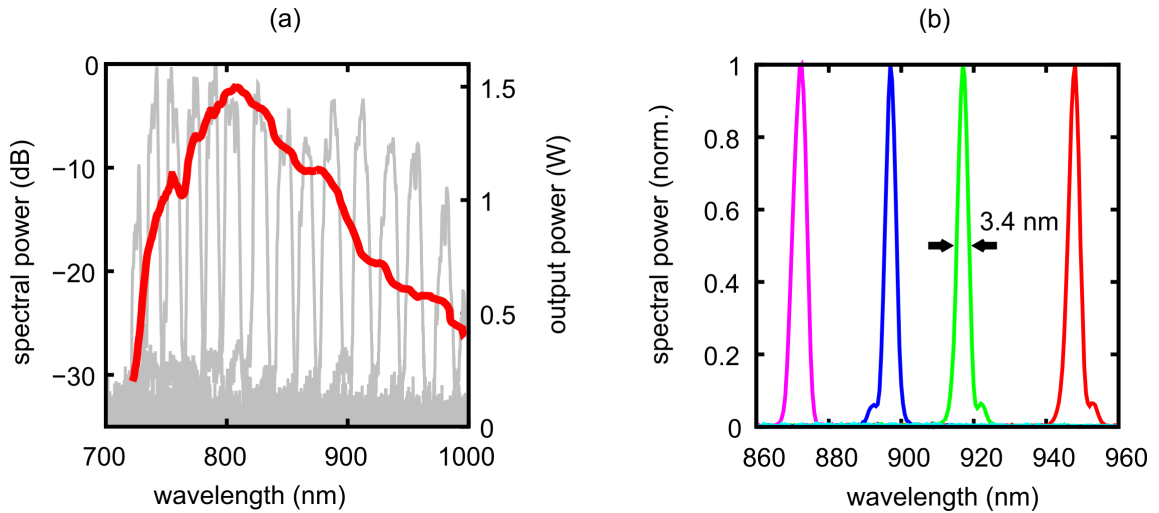


Figure 4.14: TPG-NOPO optimized for wide and smoothed spectral tunability with 36 mm of LaK8: (a) Signal spectra for different resonator lengths measured by a CCD based spectrometer; NOPO output power while tuning (red solid) (b) Zoom of three picked spectra showing the spectral bandwidth.

Especially the high spectral power density of more than 500 mW/nm of the tuneable NOPO-output spectrum, enables coherent nonlinear spectroscopic measurements with a high photon-flux. Whereas traditional spectroscopic experiments suffer from the low spectral power densities of broadband light sources (Ti:sapphire: < 2 mW/nm) and the long integration times of the related spectroscopic detectors, the NOPO allows for a fast and sensitive spectral data acquisition. This is possible since the narrowband output spectrum of the tuneable NOPO pulses provides a sufficient resolution to replace rather slow spectroscopic filters or spectrometers, as used in this traditional setups, by a single fast photo diode. For example, by doing so a fast acquisition of broadband Raman spectra covering a larger spectral range of 3400 - 960 cm^{-1} via SRS could be demonstrated [Hof13]. However, this experiment was affected by the spectral gap caused by the parasitic SHG of the NOPO in the PVWC-geometry. Consequently the non-collinear phase-matching geometry of the NOPO was changed to the TPG. The results will be shown in the next section.

Widely tuneable narrowband pulses from a TPG-NOPO

In order to achieve a smoother tuneability of the NOPO output pulses in the wavelength-range between 850 nm and 1 μm the non-collinear phase matching geometry of the NOPO was changed to the tangential phase matching geometry (TPG). As explained in the theory chapter, by doing so the parasitic signal and idler SHG

can be avoided. However, because of the more critical spatial overlap between the resonant signal and pump pulses in the BBO (see Sec.2.2.2), the NOPO in the TPG is less efficient and more sensitive to any misalignment. Fig. 4.14 (a) shows the output power of a series of measured spectra while tuning. With about 5000 fs^2 of internal dispersion and by the absence of the parasitic effects as they were observed in the PVWC-geometry, the TPG-NOPO is smoothly tuneable from 740 nm up to 1 μm . Fig. 4.14 (b) shows a zoom into the former critical wavelength region, which was the case in the PVWC-geometry.

These preliminary results are very promising when thinking about the limitations of the NOPO tuneability caused by the parasitic effects. Especially for higher pump powers with more relaxed beam diameters, the overlap between the pulses in the nonlinear crystal is less critical. However, the TPG-NOPO is currently under investigation to clarify open questions, e.g. why is the tuning range for shorter wavelengths reduced and how the decreasing output power for longer wavelengths is caused.

To answer these questions concerning the TPG-NOPO and to further investigate the dynamics of the pulse formation in the PVWC-geometry especially for the "unstable regime", both are subject of ongoing research. Therefore, the proven (2+1)D numerical algorithm was adapted for the simulation of the spatiotemporal interaction in the NOPO. However, this preliminary investigation shall not be included in this work. Instead, based on the insights gained by numerical simulations of parametric processes in Chapt.3 and the experimental work done by the investigation of the tuneable NOPO, in the next section an advanced NOPO-setup will be presented. This setup shall allow for the generation of ultra-short pulses in an ultra-broadband NOPO pumped by the long pump pulses as presented in this section.

4.2 NOPO with KLM mode-locking and breathing pulse dispersion management

In the previous section an ultra-broadband phase-matched NOPO was presented, which allows a rapid tuning over a wide spectral range without adapting the phase-matching conditions. This was possible under the use of a substantial amount of positive dispersion in the oscillator in order to maintain a stable pulsing behaviour within the whole tuning range.

For small internal net dispersion values close to zero, however, broader output spectra with spectral widths of more than 100 nm could be observed. In the previous NOPO-design such broad spectra were always connected to unstable pulsing behaviour as observed by a coherence-spike-on-a-pedestal shape of the intensity auto-

correlation. The reason for this behaviour can be found in the active mode coupling mechanism initialized by the rather long 500 fs-pump pulses, which is a typical value for the Yb-based high power pump lasers (see also Fig. 4.2). In another broadband NOPA [Gal98] much shorter pump pulses of ~ 90 fs have been used, as they are easily provided by a Ti:Sapphire oscillator. Thus, pulse durations down to 12 fs has been demonstrated out of an optical parametric oscillator with a prism based zero-dispersion management. However, mainly caused by the lack of power scalability of broadband Ti:Sapphire lasers, the output power of this system was restricted to the lower mW-range. Although with new laser materials, such as Yb:LuScO₃ and Yb:CALGO which supported sub-100 fs pulse durations, high output powers up to 12.5 W could be obtained [Gre12, Sar12b], but still the scalability of these systems is not as promising as for standard thin-disk oscillators with longer pulse durations and substantially lower nonlinearities. Here, output powers of 275 W and pulse durations of 583 fs have been reported just recently [Sar12a]. For the generation of few-cycle pulses with sub-10 fs pulse durations in an ultra-broadband NOPO, these pump pulses are not sufficient for a stable pulsing without an additional mode-coupling mechanism.

To overcome these limitations, in this work, an ultra-broadband NOPO design was developed which combines both the advantages of the power scalability of the parametric amplification concept together with the high power sub-ps thin-disk pump lasers and a strong mode-locking mechanism with a novel breathing pulse dispersion management scheme for the generation of ultra-short pulses in a NOPO.

In the next section this concept will be presented and discussed together with the first and most promising experimental results. Furthermore, an outlook about the next steps towards high energy few cycle pulse out of a NOPO will be given.

4.2.1 Experimental setup

The new non-collinear parametric oscillator concept is designed with two foci which provide an efficient parametric amplification of a strongly chirped resonant signal pulse in one focus and a soft-aperture Kerr-lens mode coupling by the compressed pulse in the other focus. A schematic of the experimental setup is illustrated in Fig. 4.15. The presented setup is ideally suited to investigate a KLM-assisted ultra-short NOPO in the case of an unpumped Ti:sapphire crystal used as Kerr-medium in the second focus⁷. As shown in the figure, the design also allows for a hybrid operation: either as an optical parametric oscillator using BIBO or as a laser with

⁷Please find more information about the Kerr-lens mode-locking mechanism in the literature [Lee05, Hea93].

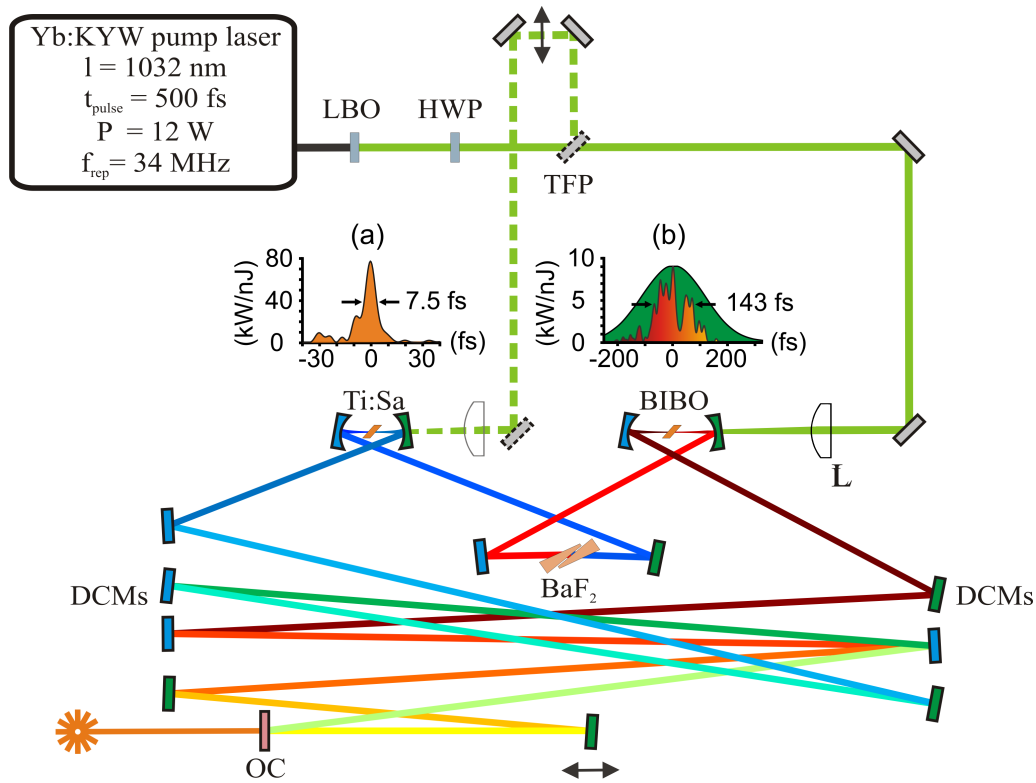


Figure 4.15: Schematic setup of two-foci NOPO with KLM-mode coupling and breathing pulse dispersion management: Type-I 2.2 mm LBO-crystal; HWP: lambda half-wave-plate; TFP: thin film polarizer; L: focusing lens ($f=100$ mm); The synchronously pumped ring-cavity consists of: - first focus: BIBO-crystal between 100 mm rad. of curv. DCMs - second focus: Ti:Sapphire crystal between 75 mm rad. of curv. DCMs; - BaF₂-wedges in a short path and the 0.5% output coupler (OC) in the long path. The color of the oscillator beam indicates the current pulse duration during one cavity round-trip (red - chirped, blue - compressed). Inset (a): calculated pulse profile after one round-trip with modeled dispersion and measured spectrum; Inset (b): calculated pulse profile after BIBO-crystal.

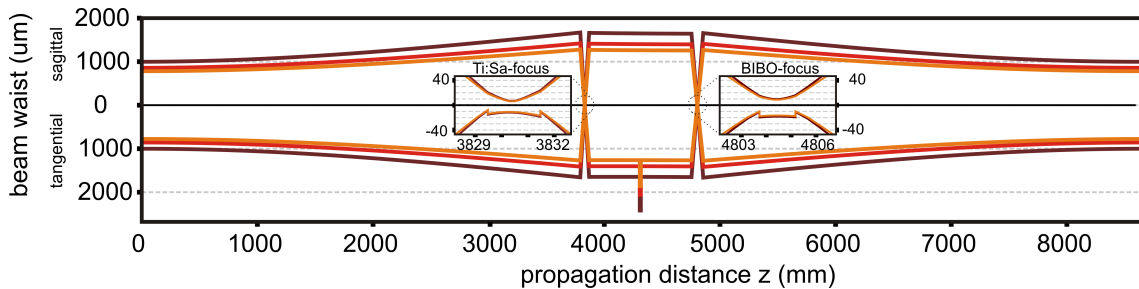


Figure 4.16: Calculated beam radius in the two-foci NOPO for a wavelength of 650 nm (orange), 800 nm (red) and 1100 nm (dark-red) in sagittal and tangential orientation with a stability factor of 0.35. Insets are showing the zoom into both foci.

the Ti:sapphire in the Kerr-focus. Therefore, both crystals can be synchronously pumped with a repetition rate of 34 MHz and an overall pump power of 7 W provided by the frequency doubled Yb:KYW thin-disk laser. Since this possibility of an additional laser operation does not require any extra effort in the experimental setup of the NOPO, it enables a straightforward pre-alignment of the cavity. Furthermore, this opens the possibility for experimental investigations on the behaviour of a synchronously pumped hybrid laser NOPO system which could combine advantages from both concepts, e.g. the excellent stability of Ti:Sapphire oscillators with the power scalability and a combination of different gain windows of the NOPO.

However, in the following only the NOPO operation will be discussed. In Fig. 4.16 the tangential and the sagittal signal beam waist with respect to the 8.6 m NOPO ring cavity is plotted as it can be calculated by an ABCD matrix formalism for the propagation of a Gaussian beam for different wavelengths (650 nm (orange), 800 nm (red) and 1100 nm (dark-red)). The 7.6 m long optical path between the two foci is folded without additional focusing mirrors. As shown by the respective insets, the waists in both foci can be calculated to approximately 20 μm (full width $1/e^2$ -max) in the Ti:Sapphire crystal and 25 μm in the BIBO crystal. In order to realize a tight overlap to the signal beam waist for the soft-aperture Kerr mode-locking in the 1.33 mm BIBO, by using a lens with a focal length of 200 mm the focusing of the pump pulses is chosen to be approximately $\sqrt{2}$ larger for a optimum gain waist. The BIBO crystal is cut to enable a broadband phase-matched amplification ($\theta=17.3^\circ$, $\alpha=3.9^\circ$) in the PVWC-geometry in the YZ-plane. The purpose of the use of BIBO instead of BBO is mainly caused by the larger non-collinear angle and smaller walk-off angle. As explained in Sec. 2.2.2 this enables a more efficient amplification in the PVWC-geometry. Furthermore, the strong thermal dependency of the phase-matching angle in BIBO helps to carefully adjust the optimum phase-matching conditions without misalignment of the cavity by changing the crystal orientation. To minimize the losses for the resonant signal the BIBO as well as the Ti:Sapphire crystal are placed under Brewster angle between the focusing mirrors with the respective radius of curvature of 100 mm for the BIBO and 75 mm for the KLM-focus. The whole cavity is equipped with double-chirped mirror pairs (DCMs) to provide a flat spectral phase over a broad spectral range while compensating the positive dispersion by the 2 mm Ti:Sapphire crystal, the 11 mm BaF₂ material and the 1.33 mm BIBO. Even though the overall dispersion of the cavity is close to zero, a strong unbalance between the two foci is introduced in the setup. The negative dispersion of 12 DCM bounces in the long path and the positive dispersion in the short path with 11 mm BaF₂ and only 4 DCM bounces are intended to allow a strong

pulse breathing during one round-trip. Consequently, as indicated by the colors of beams in the schematic of the optical path in Fig. 4.15, a long positively chirped signal pulse as required for a good temporal pump overlap in the BIBO (red colored lines) is subsequently compressed by the DCMs in the long path to an ultra-short pulse in the KLM-focus (blue colored lines). Therefore an overall zero-dispersion for an ultra-broadband operation is preserved, whereas the breathing signal pulse enables a high peak power with an almost transform limited pulse duration in the Kerr-focus and a good temporal overlap of the long pump pulses with a strongly stretched signal pulse in the BIBO.

4.2.2 First experimental results

For simplicity the first experiments were performed with a low output coupler of 0.5% and a collinear alignment between pump and resonant signal beam in the BIBO-crystal. Consequently, also the phase-matched gain bandwidth was quite narrow. For pump powers slightly above the threshold of approximately 300 mW, a stable parametric oscillation with a spectrum between 823 nm to 870 nm was obtained. By increasing the pump power in the BIBO-crystal to the maximum power of 7.4 W, provided from the SHG, a maximum NOPO output power of 1 W could be obtained. However, for an optimization of the Kerr-lens strength by adapting the cavity mode the output power decreases to approximately 500 mW, but additionally a drastic spectral broadening due to SPM in the Ti:Sapphire crystal can be observed. As shown in Fig. 4.17 (b), this SPM-broadband output spectrum spanning from about 650 nm up to 1 μm is a strong evidence of a short pulse in the KLM-focus and consequently a long pulse in the BIBO-focus. A calculation of the temporal profile of this breathing intra-cavity signal pulse for both foci is shown by the insets (a) and (b) in Fig. 4.15. For this approximation of the temporal pulse form in (b), a phase corresponding to 4 DCM bounces, 11 mm BaF₂ and 1.33 mm BIBO, is added to a transform limited pulse of 6 fs, which is supported by the measured spectrum as plotted in Fig. 4.17 (b) black (curve). The comparison given in Fig. 4.15 (b) shows that the positively chirped signal pulse (red-orange) shows a good temporal overlap with the ~ 350 fs long pump pulse (green). Furthermore, considering all additional phase contributions in one round-trip, an efficient re-compression of the intra-cavity signal pulse to 7.5 fs can be calculated. The discrepancy between this value and the transform limited pulse duration is mainly caused by the uncompensated high-order dispersion as depicted by the net round-trip phase contributions in Fig. 4.17 (b) (blue line).

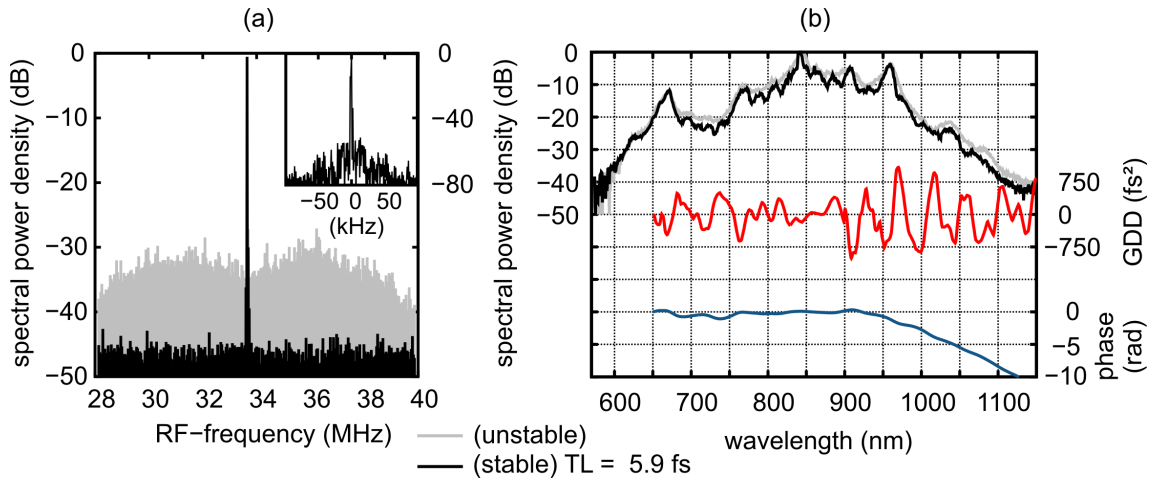


Figure 4.17: First results from the two-foci NOPO with optimized Kerr-lens action in the second focus for a stable and an unstable operation due to a slight change of the NOPO resonator length. (a) Radio-frequency analysis of the fundamental repetition frequency under stable (black) and unstable (grey) conditions. (b) Measured internal SPM-broadened OPO output spectrum with a narrowband collinear phase-matched bandwidth of about 50 nm with stable (black) and unstable RF-spectrum (grey); calculated accumulated phase (blue) and GDD (red) for one resonator round trip.

Although no optimization regarding the efficiency of the system was done so far, with the maximum pump power of 7.4 W and an optimized Kerr-lens strength, up to 500 mW of output power could be obtained with the 0.5 % output coupler mirror. Although no active stabilization of the synchronization between the pump repetition rate and the NOPO length was implemented in the experimental setup so far, the potential of a stable mode-locking behaviour with this concept is indicated by the clean radio-frequency spectrum of the signal output pulse train as shown in Fig. 4.17 (a) (black). This stable operation could be obtained with a slight detuning between the NOPO and the pump repetition rate. Since the parametric gain under zero-dispersion conditions is quite sensitive to any change in the resonator length, an active stabilization is necessary for a long-term, stable, broadband, operation. Without this stabilization, the thermal drifts between pump laser and NOPO repetition rates lead to an unstable pulsing as indicated by the grey RF-spectrum in Fig. 4.17 (a), whereas the corresponding optical spectrum, plotted by the grey line in (b), is almost unaffected.

In conclusion, the presented novel design can establish a stable pulsing with a spectral bandwidth supporting sub-10 fs pulses. As a next step, external pulse compression and measurement has to be implemented to confirm the few-cycle pulse

duration of this ultrashort NOPO operated in a novel breathing mode dispersion management. This most promising first result opens the door for few-cycle high energy pulse generation directly from a non-collinear optical parametric oscillator. Moreover, the full potential of the system has not been implemented yet, so many exciting questions are raised for future experiments, e.g. how broad the NOPO output spectrum can be made if fully exploiting the amplification bandwidth in a non-collinear scheme. To answer these questions the experimental setup is under ongoing investigation. Furthermore, the first numerical studies of an ultra-short pulse NOPO by means of the developed (2+1)D simulation model have been implemented to give a deeper understanding about the spatiotemporal dynamics within the system.

Chapter 5

Conclusion

The main objective of this thesis was to gain new insights about the spatial and temporal dynamics of parametric processes in ultra-broadband optical parametric amplifiers and oscillators in particular. In order to reach this goal, in the first part of this work comprehensive theoretical investigations of spatial, temporal, and parasitic effects in state-of-the-art OPCPA systems have been performed and compared to two in-house experiments. On the experimental side, the deep theoretical understanding of the spatiotemporal dynamics enabled the development of an ultra-broadband parametric oscillator with fast tuning capabilities. The studies on both parametric amplification and parametric oscillators show the potential of these processes for the generation of ultra-short pulses. Within this framework these novel concepts were established theoretically and experimentally and the main results are briefly summarized as follows.

Theoretical investigation of ultra-broadband state-of-the-art OPCPA systems

In the first part of this work a novel $(2+1)$ dimensional numerical model for the simulation of non-collinear parametric amplification processes has been developed. The model includes spatial, temporal, and all second order nonlinear effects of ultra-short light pulses propagating non-collinearly in one principle plane of a birefringent crystal. Therefore, dispersion, diffraction, non-collinear propagation, and the walk-off are implemented in the Fourier split-step model. Since the work on the simulations went hand in hand with the in-house experimental realization of different state-of-the-art OPCPA systems, it was able to give a first approximation of the appropriate parameters in the conceptional phase of the OPCPA development. On the other hand, the close interrelation with the experiments opened the possibility for quantitative and qualitative fundamental understanding of the specific processes leading to well known and formerly unidentified experimental observations in OPCPAs.

Furthermore, the excellent agreement between experimental and simulation results could impressively verify the model and the validity of the applied approximations.

This confirmation allows the (2+1)D model to be used for new predictions and to answer many open questions concerning these OPCPA systems, especially with respect to their different non-collinear phase-matching geometries (PVWC and TPG). Thereby, since all significant physical effects for ultra-broadband parametric amplification processes are included, even quantitative predictions about the efficiency, beam quality and compressibility can be made. Moreover, fundamental questions can now be answered: for example, about the origin and the fundamental properties of the cascaded mixing products as they are partly visible in the superfluorescence cone of seeded high-power OPCPA systems. Since all these mixing-signals and their phase relations could be clarified, it was possible to propose a new scheme for the measurement of the CEP of the amplified signal pulses without an additional spectral broadening for an f-2f measurement.

Furthermore, also the combination of different amplification windows in multi-color pumped subsequential amplification stages was studied aided by the (2+1)D simulation. Considering the spatiotemporal dynamics during the evolution of the different spectral components in this OPCPA system, quite surprising experimental results could be quantitatively simulated and explained for the first time.

This deep understanding of the investigated OPCPA-systems with different pump pulse energies and beam waists, allows a crucial analysis of the limits of the different phase-matching geometries (PVWC and TPG) regarding the beam quality and the compressibility of the amplified pulses in dependence of the available pump energy and hence the pump waist and crystal length. This analysis leads to the categorization of 3 different distinct regimes: low pump pulse energies ($\sim 10 \mu\text{J}$), moderate energies ($\sim 30 \mu\text{J}$) and high energies (beyond $\sim 100 \mu\text{J}$). In the first two, spatiotemporal effects play an important role, especially for the lower available pump pulse energies. The main difference is in the amount of beam distortions and modulations of the spectral and spatial intensity and phase. In these regimes only the PVWC-geometry yields a good beam quality and compressibility. The third regime, allowing a loose focus, has low spatial effects, leading to the preference of the TPG over the PVWC, as the parasitic SHG is shifted to higher wavelengths ($> 1 \mu\text{m}$).

Apart from the presented examples and design criteria, which were mostly performed for BBO and a spectral range from 600 - 1200 nm, the established model is more general and any kind of nonlinear crystal can be easily implemented. Thus, also different wavelength ranges (e.g. mid-IR) or exotic crystals can be applied to predict their potential OPA performance. Moreover, the model can be used for ev-

ery type of 2nd order effects to calculate e.g. spectral focusing or cascaded effects in frequency doubling or broadband sum frequency generation processes.

Experimental realization of an ultra-broadband NOPO

The second part of this work was dedicated to the investigation of an ultra-broadband non-collinear optical parametric oscillator. The goal was to combine the unique properties of ultra-broadband double-chirped mirrors, which are also the key components in state-of-the-art sub-6 fs Ti:sapphire oscillators, with the advantages of the parametric amplification scheme. In contrast to high power OPOs in other works, which use narrowband and slowly tuneable phase-matching concepts, in the presented system an ultra-broadband gain bandwidth between 640 nm to 1200 nm is provided by the non-collinear phase-matching concept. Therefore, the insights of the theoretical considerations from the first part of this work established the basis for the implementation of this phase-matching concept in the NOPO design.

Especially in wide tuneable highly dispersive NOPO, both TPG and PVWC-geometries could be successfully realized, showing a continuous and wide tuneability. This NOPO in the PVWC-geometry was tuneable over an ultra-broad spectral range, starting at 640 nm up to 1200 nm with a significant spectral gap at 900 nm due to parasitic effects. On the other hand, the TPG offers a smooth tuneability without this parasitic gap, but suffers from a more critical spatial overlap between signal and pump in the 2 mm long BBO crystal used in the NOPO. Therefore, the output power in this geometry was limited to about 1 W. However, in both geometries the presented system marks a record in tuneability and output power from a non-collinear parametric oscillator in this spectral range [Lan12]. Especially in terms of spectral power density this marks an important milestone regarding the goal of demonstrating the power scalability of the NOPO-concept by applying a frequency doubled high-power Yb:KLu(WO₄)₂ thin-disk laser as a pump source. Here, with an effective pump power of 10 W, more than 3 W of output power could be demonstrated with an excellent beam quality and long-term stability. Furthermore, by reducing the internal dispersion, the spectral bandwidth of the NOPO pulses could be increased and with a slightly reduced tuneability, compressed pulse durations of about 80 fs could be obtained. The shortest stable pulses that could be demonstrated with this setup were in the order of 40 fs. For broader bandwidth, supporting even shorter pulses, a chaotic pulsing behaviour set in, caused by the weak active mode-locking strength of the instantaneous gain from the 500 fs pump pulses.

Arising from these experimental results, the NOPO was redesigned for the goal of generating sub-10 fs few-cycle pulses. Therefore, an additional fast passive mode-

locking mechanism, a second focus for Kerr-lensing, was added to realize a breathing pulse, zero-net-dispersion NOPO. The BIBO crystal in the focus for the ultra-broadband parametric gain was synchronously pumped at 34 MHz with a pump power of 7 W from a frequency doubled Yb:KYW thin-disk laser. With this setup it was possible, for the first time, to demonstrate pulses with an ultra-broadband spectrum supporting sub-10 fs pulses directly from a NOPO. Thereby, a stable pulsing behaviour was indicated by the clean radio frequency spectrum of the NOPO output pulse train.

The presented experimental results of the developed highly dispersive NOPO makes it a unique and powerful tool for the nonlinear spectroscopy, microscopy, and pump probe techniques which benefit from the high photon-flux, outstanding fast tuneability and temporal resolution of the provided fs-pulses [Lan12, Hof13]. On the other hand, the first demonstration of a stable ultra-broadband parametric oscillation in the two-foci NOPO, with Kerr-lens mode-locking promises to open the door for the generation of few-cycle pulses from such a system in the near future. Considering the fact that no significant progress has been made in the development of ultra-broadband Ti:sapphire oscillators in the last decade, the NOPO could be a real alternative to these lasers, showing a significant potential as a new light source in the few-cycle regime. With its particular advantages, especially regarding the power scalability and the ultrabroad gain bandwidth (which is much wider than in Ti:sapphire), it offers many possibilities. For example, the free choice of the phase-matched gain window of the nonlinear crystal could provide few-cycle pulses from the UV to the IR-spectral range. Additionally, the higher gain of the parametric amplification process within one round-trip enables intra cavity conversion processes, e.g. for the high harmonic generation directly in an ultra-short pulse NOPO which were not achievable with current few-cycle Ti:sapphire lasers. The ultra-broadband NOPO with additional Kerr-medium operating in a breathing dispersion-management mode is a very novel concept, firstly demonstrated in this work. Thus, it is still at an early state of its development and opens the door for a variety of new experiments which can benefit from the advantages of the parametric process.

Chapter 6

Outlook

The close interplay of experimental and numerical investigations in this work has created a deeper understanding of the studied parametric processes which has been used to explain experimental observations and to develop new concepts for both parametric amplifier and oscillators. Many new ideas initiated by this work remain unexplored and open up a wide variety of new experiments ranging from intra-cavity harmonic generation from NOPOs, new nonlinear output coupling schemes to ultrabroad phase-matching of MID-IR OPCPA systems.

Some of these ideas are already a matter of ongoing experimental or theoretical investigations: as an example, the measurement of the signal carrier envelope phase directly in the PVWC-OPCPA as described in Sec.3.1.2 is currently investigated experimentally. Another project is dedicated to the generation of IR high energetic femtosecond pulses at $2\ \mu\text{J}$ from a parametric downconversion process in the TPG geometry, which is only seeded by a low cost cw-laser diode. Here, simulation results in BBO have shown that with $10\ \mu\text{J}$ pump pulse energy the efficiency of the TPG-amplification processes for short wavelengths around 680 nm is extraordinarily high, so that almost the complete pump energy can be converted to signal and idler pulses.

Among all the curious people of the world, no one has a greater interest in further experimental studies of the NOPO than the author of these humble lines. Beside the implementation of the fast scanning mechanism which is able to fully exploit the limits of the fast tuning possibility of ultra-broadband highly dispersive NOPO, the next step regarding the ultra-short pulse NOPO is the realization of a feedback loop for the resonator length synchronization. Since this was already done for the long-term stability measurements in the single-foci NOPO, this step in the two-foci NOPO should be straight forward. With long-term stable ultra-broadband pulses from the Kerr-lens mode-locked NOPO the demonstration of the sub-10 fs pulse could then be performed by, e.g. a FROG or SPIDER measurement or by the D-scan technique. In a next step, a state-of-the-art Yb-based thin disk laser,

which is currently under construction, is able to provide sufficient pump power to demonstrate the power scalability of this ultra-short pulse NOPO by adapting the beam waists in the nonlinear crystal. Moreover, an experiment is planned which could take advantage of the enormous intensity of the few-cycle signal intra-cavity pulse in the NOPO for the generation of high harmonics in a gas-jet.

One of the most important advantages of the presented simulation model, apart from its complete implementation of propagation effects, is the high speed with which the code can be run on standard desktop computers. This enables for the first time a simulation of the dynamics inside a parametric oscillator considering the full spatiotemporal complexity of the non-collinear parametric amplification process. As first results here are already very promising and further demonstrate the validity and agreement of the simulation with experimental data, a brief glance on the implementation and capacity of this concept shall be shown in the following. A short explanation of principle of a slightly enhanced (2+1)D model will be given and a few selected first results will be presented.

6.0.3 (2+1)D NOPO simulation

The principle of the (2+1)D split-step simulation algorithm, as it was explained (Sec. 2.3.1) and experimentally validate (Sec. 3.1.1) above, is shown by the inner single-pass through the crystal in Fig. 6.1. Additionally, in the enhanced (2+1)D NOPO simulation a further outer oscillator-loop is realized, which enables a signal feedback at each round-trip. In this feedback loop the amplified ordinary field $E_o(f_x, f_t)$ is applied by a filter function to implement all essential resonator conditions. This includes an angular filter with respect to the resonator aperture and a spectral filter which implements both the losses due to the transmission function of the output coupler and the accumulated round-trip phase. This phase is calculated under consideration of all DCM reflections, an additional unpumped pass through the BBO-crystal, the internal dispersion by the chosen amount of LaK8-glass and a certain round-trip delay relatively to the next pump pulse. Furthermore, this filter function includes the re-imaging of the signal pulse and the compensation for the non-collinear displacement in the crystal.

As it can be seen in the figure, at each round-trip loop a fresh pump pulse is provided in the extra-ordinary field. The pump pulse energy of 250 nJ, a pulse duration of 500 fs, and a beam radius of 20 μm matches closely the experimental conditions shown in Sec. 4.1.2. Accordingly, also the crystal length and the phase-matching conditions are chosen to be similar (PVWC). In contrast to the experimental NOPO the simulation does not start from the noise floor, but from a weak start pulse in

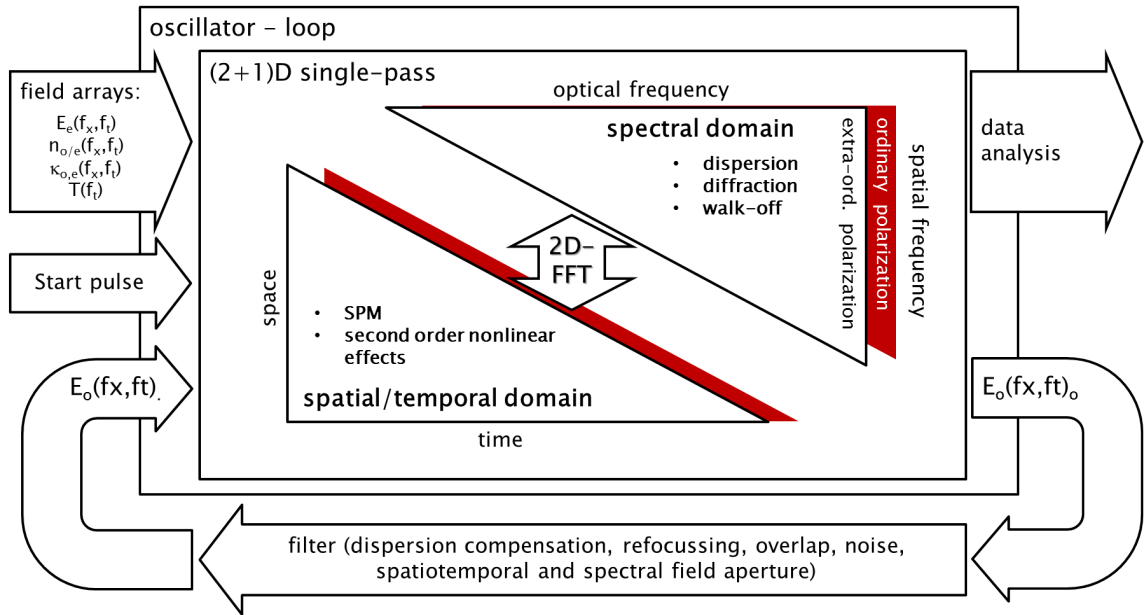


Figure 6.1: Principle of the adapted split-step numerical model, as described in Sec. 2.3.1, for the treatment in a non-collinear parametric oscillator.

order to save computing time. This is possible since previous test, not shown here, have indicated that resulting NOPO pulsing behaviour started from noise is similar to the one by simply defining low energetic initial start pulse.

Preliminary results

For a variety of internal dispersion values very plausible results haven been obtained with the (2+1)D NOPO simulation, the following calculations consider only the highly dispersive NOPO provided by 36 mm LaK8 material. Moreover, the preliminary results shown in the following shall only demonstrate the potential of the (2+1)D NOPO simulation model at the example of the rich spatiotemporal effects in the PVWC-NOPO, so not all visible effects will be explained in completeness here.

After starting the simulation algorithm, the weak initial broadband seed pulse exponentially increases in intensity, whereas the spectrum is rapidly narrowed around the center wavelength selected by the round-trip delay (as experimentally observed in Sec. 4.1.3). Fig. 6.2 (a) shows the signal spectra mapped for a large series of different round-trip delays, each shown after 80 round-trips. The simulated tuning map is in very good agreement with the measured spectra from the highly dispersive tuneable NOPO as presented in Sec. 4.1.3. For a better comparison, Fig. 6.2 (b) shows a corresponding tuning map created from the measured spectra shown in Fig. 4.12 (a).

This similarity of both theory and experiment without any fitting parameter is striking and gives even more confidence that also the complex temporal couplings with a NOPO can be well described. An interesting feature visible in both figures is shown by the spectral tuning behaviour for resonator detuning lengths beyond $300\ \mu\text{m}$. Beyond this point, the measured and simulated spectra are shifting towards smaller wavelengths while increasing the resonator length in contrast to smaller detunings. This behaviour can be explained by a crossing of signal and idler at the degeneracy wavelength, so that now actually the idler shows shorter wavelength as the signal. The signal for wavelengths beyond $1\ \mu\text{m}$ could not be measured in the experiment due to the use of a silicon-based spectrometer. The measured idler, however, indicates indirectly the further signal tuneability up to $\sim 1.2\ \mu\text{m}$. This is confirmed by simulation results, showing a similar behavior, whereas in this case the idler can be clearly distinguished by its angle of propagation within the (2+1) dimensional treatment in the NOPO simulation.

Fig. 6.3 illustrates a further analysis of the simulation results from this example. An approximation of the achievable NOPO output power is plotted in (a) (red curve). Assuming a repetition rate of $34\ \text{MHz}$ and a output coupling of 15% , the output power is calculated by the average signal pulse energy over the last 400 round-trips. So each red point stands for an average output power assuming a steady-state operation with a respective round-trip delay shown by the black curve. Comparing

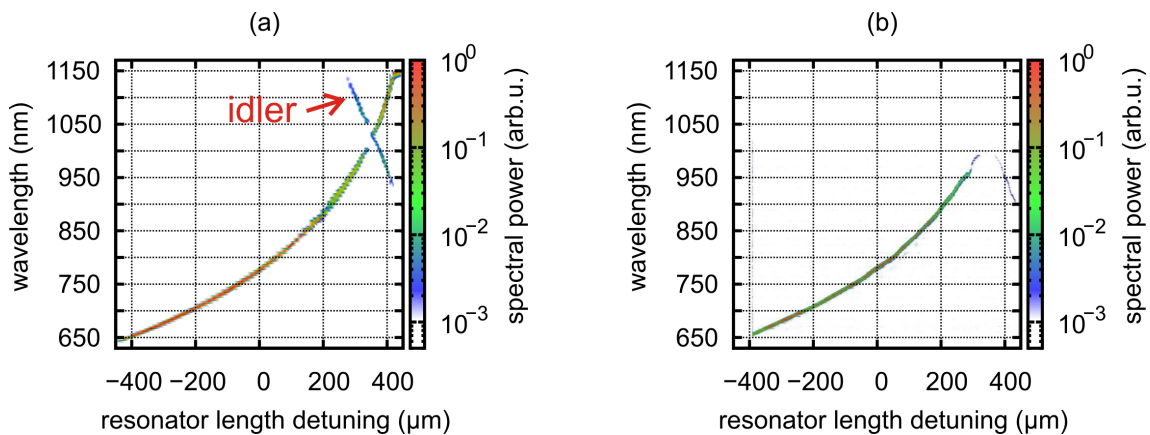


Figure 6.2: Comparison of experimental and simulated highly dispersive NOPO: (a) Simulated spectra for different round-trip delays mapped for the corresponding resonator length detuning and (b) mapped series of spectra measured by an Ocean Optics spectrometer (USB4000) for different relative resonator lengths, as shown in Fig. 4.12. The spectra which describe a negative slope with respect to the resonator detuning visible in both maps shows the idler which crosses the degeneracy.

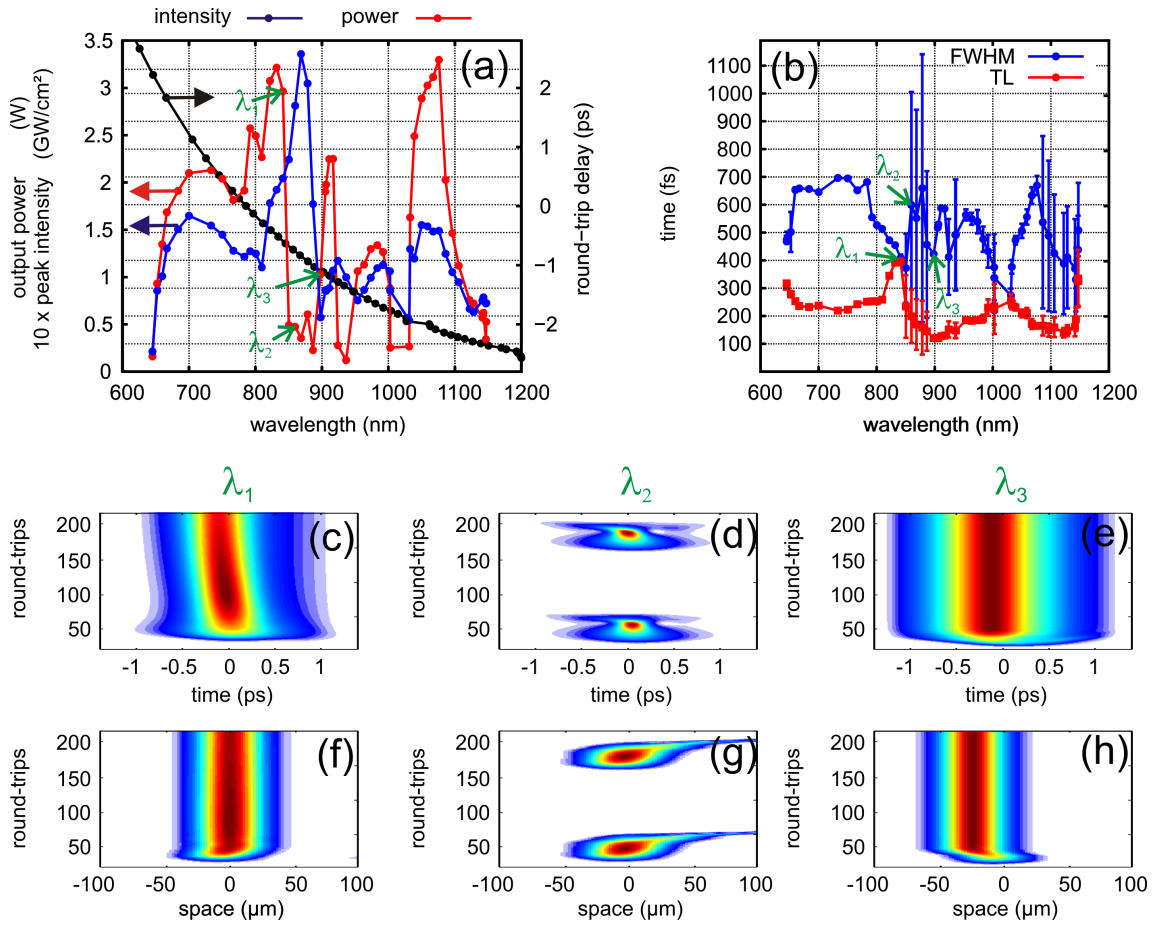


Figure 6.3: Analysis of the NOPO simulation results: (a) Average output power (red) and maximum peak intensity (blue) within the last 400 round-trips for different round-trip delays (black) mapped with respect to the corresponding center wavelength; (b) The respective maximum and minimum (indicated by the errorbar) signal pulse duration (blue) and transform limited pulse duration (red) within the last 400 round-trips. (c-h) Spatiotemporal signal pulse evolution for three different wavelength, λ_1 - 840 nm, λ_2 - 860 nm, λ_3 - 890 nm.

these results to the measured NOPO output power as shown in Fig. 4.11, a good agreement can be observed for wavelengths shorter than 850 nm. For wavelengths of ~ 860 nm, however, an irregular pulsing occurs. This is also indicated by the enormous maximum peak power of more than 30 GW/cm^2 for wavelengths close to the maximum parasitic signal SHG. Accordingly, a similar behaviour can be observed in 6.3 (b), showing the range of different pulse durations (blue) and transform limited pulse durations (red) within 400 round-trips with respect to the corresponding center wavelength. Here, the maximum peak intensity depicted by (a) shows a strong variance of the pulse duration, spanning from sub-200 fs up to 1.1 ps within the 400

round-trips. Also the second gap in the output power plot around 925 nm, caused by the parasitic SHG of the corresponding idler at 1180 nm, shows a strong pulse variation. In contrast, the situation is different for the gap around 1020 nm, which can be mainly attributed to the output coupler characteristics. However, the regions of parasitic effects are very interesting for further studies since quite complex pulse formation dynamic seems to occur here. A first deeper insight into this complicated pulsing behaviour can be seen in Fig. 6.3 (c-h), resolving the spatial and temporal signal pulse evolution for each resonator round-trip. This is shown for three different NOPO wavelengths. Within the wavelength range influenced by the parasitic effects a self-compression, which results in a bifurcation-like behaviour, can be observed. This behaviour continues periodically, at least within the simulated 500 round-trips. However, a closer analysis of these very interesting pulse dynamics cannot be subject of this outlook.

Nevertheless, these preliminary results and the additional insights in the spatiotemporal pulse forming dynamics of the NOPO demonstrate the potential of the model. Therefore, the next steps will be a validation of the simulation results by more detailed experimental measurements. Especially, the predicted opposite behaviour of the average output power and maximum peak power in the regions of parasitic effects should be experimentally verifiable. Also the shown spatial drift instabilities (Fig. 6.3 (g)) should be easily accessible in the experiment. The exact understanding of the interplay between spatiotemporal and parasitic mechanisms can help to avoid the shown effects or even to take advantage of them: e.g. highly repetitive ultra-short NOPO pulses within a well defined low-repetitive burst could be perfectly suited for a further high power amplification. On the other hand, concerning the further development of the (2+1)D NOPO simulation, the implementation of a fast passive mode-locking mechanism in the feedback loop will allow the simulation of the ultra-short pulse two-foci NOPO. Together with the ongoing experimental work this will help in a better understanding and further improvement of the mode-locked pulsing behaviour of the ultra-short pulse NOPO. Especially, further experimental and numerical investigations of the generated mode-comb will give insights into the limits regarding the phase noise and the CEP stability, particularly in comparison to the excellent noise properties of Ti:sapphire lasers.

Bibliography

- [Adl09] F. Adler, K. Cossel, M. Thorpe, *Phase-stabilized, 1.5 W frequency comb at 2.8 - 4.8 μm* , Optics letters **34**(9), 1330–1332 (2009).
- [Agr00] G. Agrawal, *Nonlinear fiber optics*, Nonlinear Science at the Dawn of the 21st Century 195–211 (2000).
- [Ari97] G. Arisholm, *General numerical methods for simulating second-order nonlinear interactions in birefringent media*, JOSA B **14**(10), 2543–2549 (1997).
- [Bhu09] K. V. Bhupathiraju, A. D. Seymour, F. Ganikhanov, *Femtosecond optical parametric oscillator based on periodically poled stoichiometric LiTaO₃ crystal*, Optics letters **34**(14), 2093–5 (Juli 2009).
- [Bin10] T. Binhammer, S. Rausch, M. Jackstadt, G. Palmer, U. Morgner, *Phase-stable Ti:sapphire oscillator quasi-synchronously pumped by a thin-disk laser*, Applied Physics B **100**(1), 219–223 (April 2010).
- [Boy08] R. W. Boyd, *Nonlinear Optics*, Nonlinear Optics Series (Elsevier Science, 2008).
- [Bro11] J. Bromage, J. Rothhardt, S. Hädrich, C. Dorrer, C. Jocher, S. Demmler, J. Limpert, A. Tünnermann, J. D. Zuegel, *Analysis and suppression of parasitic processes in noncollinear optical parametric amplifiers*, Optics express **19**(18), 16797–808 (August 2011).
- [Cer03] G. Cerullo, S. De Silvestri, *Ultrafast optical parametric amplifiers*, Review of Scientific Instruments **74**(1), 1 (2003).
- [Con10] M. Conforti, F. Baronio, C. D. Angelis, *Nonlinear envelope equation for broadband optical pulses in quadratic media*, Physical Review A (3) (2010).
- [Cou02] A. Couairon, S. Tzortzakis, L. Bergé, M. Franco, *Infrared femtosecond light filaments in air: simulations and experiments*, JOSA B **19**(5), 1117–1131 (2002).

- [DeM67] F. DeMartini, C. Townes, T. Gustafson, P. Kelley, *Self-steepening of light pulses*, Physical Review **164**(2) (1967).
- [Dem12] S. Demmler, J. Rothhardt, S. Hädrich, J. Bromage, J. Limpert, A. Tünnermann, *Control of nonlinear spectral phase induced by ultra-broadband optical parametric amplification*, Optics letters **37**(19), 3933–5 (Oktober 2012).
- [Dmi10] V. G. Dmitriev, G. G. Gurzadyan, D. N. Nikogosyan, *Handbook of Non-linear Optical Crystals*, Springer Series in Optical Sciences (Springer, 2010).
- [Fle76] J. a. Fleck, J. R. Morris, M. D. Feit, *Time-dependent propagation of high energy laser beams through the atmosphere*, Applied Physics **10**(2), 129–160 (Juni 1976).
- [Fle83] J. A. Fleck, Jr., M. D. Feit, *Beam propagation in uniaxial anisotropic media*, Journal of the Optical Society of America **73**(7), 920 (Juli 1983).
- [Fra61] P. Franken, A. Hill, *Generation of optical harmonics*, Physical Review Letters **7**(1), 118–120 (1961).
- [Gal98] G. M. Gale, M. Cavallari, F. Hache, *Femtosecond visible optical parametric oscillator*, Journal of the Optical Society of America B **15**(2), 702 (Februar 1998).
- [Gho08] M. Ghotbi, A. Esteban-Martin, M. Ebrahim-Zadeh, *Tunable, high-repetition-rate, femtosecond pulse generation in the ultraviolet*, Opt. Lett. **33**(4), 345–347 (Februar 2008).
- [Gre12] A. Greborio, A. Guandalini, J. Aus der Au, *Sub-100 fs pulses with 12.5-W from Yb:CALGO based oscillators* (Februar 2012).
- [Hae12] S. Haedrich, J. Rothhardt, M. Krebs, S. Demmler, J. Limpert, A. Tünnermann, *Improving carrier-envelope phase stability in optical parametric chirped-pulse amplifiers by control of timing jitter.*, Optics letters **37**(23), 4910–2 (Dezember 2012).
- [Har12] A. Harth, M. Schultze, T. Lang, T. Binhammer, S. Rausch, U. Morgner, *Two-color pumped OPCPA system emitting spectra spanning 1.5 octaves from VIS to NIR*, Opt. Express **20**(3), 3076–3081 (Januar 2012).

- [Hea93] D. R. Heatley, a. M. Dunlop, W. J. Firth, *Kerr lens effects in a ring resonator with an aperture mode locking and unidirectional operation.*, Optics letters **18**(2), 170–2 (Januar 1993).
- [Heg11] R. Hegenbarth, A. Steinmann, G. Tóth, J. Hebling, H. Giessen, *Two-color femtosecond optical parametric oscillator with 1.7 W output pumped by a 7.4 W Yb:KGW laser*, J. Opt. Soc. Am. B **28**(5), 1344–1352 (2011).
- [Hof13] C. Hoffmann, T. Lang, U. Morgner, *Stimulated Raman scattering with a rapidly tunable non-collinear optical parametric oscillator*, The European Conference on Lasers and Electro-Optics **147**, 4799 (2013).
- [Hua11] S. Huang, G. Cirimi, J. Moses, K. Hong, *High-energy pulse synthesis with sub-cycle waveform control for strong-field physics*, Nature Photonics **5**(8), 475–479 (Juli 2011).
- [Kae01] F. X. Kaertner, U. Morgner, R. Ell, T. Schibli, J. G. Fujimoto, E. P. Ippen, V. Scheuer, G. Angelow, T. Tschudi, *Ultrabroadband double-chirped mirror pairs for generation of octave spectra"*, J. Opt. Soc. Am. B **18**(6), 882–885 (Juni 2001).
- [Khu07] J. B. Khurgin, *Optical parametric oscillator: Mirrorless magic*, Nat Photon **1**(8), 446–447 (August 2007).
- [Kog66] H. Kogelnik, T. Li, *Laser beams and resonators*, Proceedings of the IEEE **54**(10), 1312–1329 (1966).
- [Kra09a] G. Krauss, S. Lohss, T. Hanke, A. Sell, S. Eggert, R. Huber, A. Leitenstorfer, *Synthesis of a single cycle of light with compact erbium-doped fibre technology*, Nature Photonics **4**(1), 33–36 (Dezember 2009).
- [Kra09b] F. Krausz, *Attosecond physics*, Reviews of Modern Physics **81**(1), 163–234 (Februar 2009).
- [Lam09] T. P. Lamour, L. Kornaszewski, J. H. Sun, D. T. Reid, *Yb: fiber-laser-pumped high-energy picosecond optical parametric oscillator*, Opt. Express **17**(16), 14229–14234 (August 2009).
- [Lan12] T. Lang, T. Binhammer, S. Rausch, G. Palmer, M. Emons, M. Schultze, A. Harth, U. Morgner, *High power ultra-widely tuneable femtosecond pulses from a non-collinear optical parametric oscillator (NOPO)*, Optics express **20**(2), 912–7 (Januar 2012).

- [Lan13] T. Lang, A. Harth, J. Matyschok, T. Binhammer, M. Schultze, U. Morgner, *Impact of temporal, spatial and cascaded effects on the pulse formation in ultra-broadband parametric amplifiers*, Opt. Express **21**(1), 949–959 (Januar 2013).
- [Lee05] Y. Lee, J. Yi, Y. Cha, Y. Rhee, *Numerical analysis of soft-aperture Kerr-lens mode locking in Ti:sapphire laser cavities by using nonlinear ABCD Matrices*, Journal of the Korean Physical Society **46**(5), 1131–1136 (2005).
- [Liu02] T. Liu, G. Hu, *Measurement of Ultrashort Laser Pulses in life science*, Band 4536, 33–37 (April 2002).
- [Liu13] Y. Liu, T. Gerber, Y. Sych, P. Radi, G. Knopp, *Real-time observation of ultrafast internal conversion in ethylbenzene by femtosecond time-resolved photoelectron imaging*, Optics express **21**(14), 7034–7040 (2013).
- [Man56] J. Manley, H. Rowe, *Some General Properties of Nonlinear Elements-Part I. General Energy Relations*, Proceedings of the IRE **44**(7), 904–913 (Juli 1956).
- [Man09] E. Mansten, J. Dahlstroem, J. Mauritsson, T. Ruchon, A. L’Huillier, J. Tate, M. Gaarde, P. Eckle, A. Guandalini, M. Holler, F. Schapper, L. Gallmann, U. Keller, *Spectral Signature of Short Attosecond Pulse Trains*, Physical Review Letters **102**(8), 083002 (Februar 2009).
- [Mat12] L. Mateos, P. Molina, J. Galisteo, C. López, L. E. Bausá, M. O. Ramírez, *Simultaneous generation of second to fifth harmonic conical beams in a two dimensional nonlinear photonic crystal*, Optics express **20**(28), 29940–8 (Dezember 2012).
- [Mat13] J. Matyschok, T. Lang, T. Binhammer, *Temporal and spatial effects inside a compact and CEP stabilized, few-cycle OPCPA system at high repetition rates*, Optics ... **21**(24), 475–479 (2013).
- [Oie97] a. L. Oien, I. T. McKinnie, P. Jain, N. a. Russell, D. M. Warrington, L. a. Gloster, *Efficient, low-threshold collinear and noncollinear beta-barium borate optical parametric oscillators.*, Optics letters **22**(12), 859–61 (Juni 1997).
- [Pal08] G. Palmer, M. Schultze, M. Siegel, M. Emons, U. Bunting, U. Morgner, *Passively mode-locked Yb:KLu(WO₄)₂ thin-disk oscillator operated*

- in the positive and negative dispersion regime*, Optics Letters **33**(14), 1608 (Juli 2008).
- [Pro11] O. Pronin, J. Brons, C. Grasse, V. Pervak, *High-power 200 fs Kerr-lens mode-locked Yb: YAG thin-disk oscillator*, Optics **36**(24), 4746–4748 (2011).
- [Rau08] S. Rausch, T. Binhammer, A. Harth, J. Kim, *Controlled waveforms on the single-cycle scale from a femtosecond oscillator*, Opt. ... **16**(13), 327–331 (2008).
- [Rei98] D. Reid, G. Kennedy, A. Miller, W. Sibbett, M. Ebrahimzadeh, *Widely tunable, near- to mid-infrared femtosecond and picosecond optical parametric oscillators using periodically poled LiNbO₃ and RbTiOAsO₄*, IEEE Journal of Selected Topics in Quantum Electronics **4**(2), 238–248 (1998).
- [Ros02] I. Ross, P. Matousek, G. New, K. Osvay, *Analysis and optimization of optical parametric chirped pulse amplification*, JOSA B **19**(12), 2945–2956 (2002).
- [Rot10] J. Rothhardt, S. Hädrich, E. Seise, M. Krebs, F. Tavella, A. Willner, S. Düsterer, H. Schlarb, J. Feldhaus, J. Limpert, J. Rossbach, A. Tünnermann, *High average and peak power few-cycle laser pulses delivered by fiber pumped OPCPA system*, Optics express **18**(12), 12719–26 (Juni 2010).
- [Rot12] J. Rothhardt, S. Demmler, S. Hädrich, J. Limpert, A. Tünnermann, *Octave-spanning OPCPA system delivering CEP-stable few-cycle pulses and 22 W of average power at 1 MHz repetition rate.*, Optics express **20**(10), 10870–8 (Mai 2012).
- [Row11] J. D. Rowley, S. Yang, F. Ganikhanov, *Power and tuning characteristics of a broadly tunable femtosecond optical parametric oscillator based on periodically poled stoichiometric lithium tantalate*, J. Opt. Soc. Am. B **28**(5), 1026–1036 (2011).
- [Sar12a] C. J. Saraceno, F. Emaury, O. H. Heckl, C. R. E. Baer, M. Hoffmann, C. Schriber, M. Golling, T. Südmeyer, U. Keller, *275 W average output power from a femtosecond thin disk oscillator operated in a vacuum environment.*, Optics express **20**(21), 23535–41 (Oktober 2012).
- [Sar12b] C. J. Saraceno, O. H. Heckl, C. R. E. Baer, C. Schriber, M. Golling, K. Beil, C. Kränkel, T. Südmeyer, G. Huber, U. Keller, *Sub-100 femtosecond pulses*

- from a SESAM modelocked thin disk laser, *Applied Physics B* **106**(3), 559–562 (Januar 2012).
- [Sch10] M. Schultze, T. Binhammer, G. Palmer, *Multi- μ J, CEP-stabilized, two-cycle pulses from an OPCPA system with up to 500 kHz repetition rate*, *Optics express* **18**(26), 327–332 (2010).
- [Sch13] M. Schultze, E. M. Bothschafter, A. Sommer, S. Holzner, W. Schweinberger, M. Fiess, M. Hofstetter, R. Kienberger, V. Apalkov, V. S. Yakovlev, M. I. Stockman, F. Krausz, *Controlling dielectrics with the electric field of light*, *Nature* **493**(7430), 75–8 (Januar 2013).
- [Sie86] A. E. Siegman, *Lasers* (University Science Books, 1986).
- [Szi75] E. a. Sziklas, a. E. Siegman, *Mode calculations in unstable resonators with flowing saturable gain. 2: Fast Fourier transform method.*, *Applied optics* **14**(8), 1874–89 (August 1975).
- [Tre01] R. Trebino, P. OSHEA, M. Kimmel, X. Gu, *Measuring ultrashort laser pulses*, *Optics and Photonics News* **12**, 22–25 (2001).
- [Yam91] K. Yamamoto, K. Mizuuchi, K. Takeshige, Y. Sasai, T. Taniuchi, *Characteristics of periodically domain-inverted LiNbO₃ and LiTaO₃ waveguides for second harmonic generation*, *Journal of Applied Physics* **70**(4) (1991).
- [Zip03] W. R. Zipfel, R. M. Williams, W. W. Webb, *Nonlinear magic: multiphoton microscopy in the biosciences.*, *Nature biotechnology* **21**(11), 1369–77 (November 2003).

List of Figures

2.1	Schematic of propagation directions relative angles in a BBO-like index ellipsoid	9
2.2	Illustration of the origin of the two generalized coupled equations . . .	13
2.3	Schematic of the different non-collinear phase-matching geometries . .	16
2.4	Color-map of the broadband phase-matching conditions BBO	17
2.5	Schematic of spatial pulse shaping and in-homogeneous efficiency during optical parametric amplification	19
2.6	Illustration of the temporal pulse shaping dynamics while parametric amplification in BBO	22
2.7	Distribution of propagation with respect of spatial and optical frequency in BBO	24
2.8	Typical input computational field arrays for the (2+1)D simulation . .	26
2.9	Principle of the split-step simulation model	27
2.10	Interpretation of simulation data: spatiotemporal and spectral illustration	30
2.11	Spectrally and angularly resolved timing map for NOPO (PVWC) . .	31
3.1	Schematic setup of the high power double stage OPCPA-system . . .	35
3.2	Comparison of simulated and experimental results of the double stage high power OPCPA	37
3.3	Angular variation of the intensity distribution with respect to the delay between pump and seed pulse	40
3.4	Illustration of the spectral, angular and temporal distributions of all visible and non-visible mixing products occurring in a high power OPCPA	42
3.5	Schematic setup of the two-color pumped OPCPA-system	46
3.6	Simulated and experimentally measured spectrum and phase of a two-color pumped OPCPA-system	47

3.7	Angularly resolved optical spectrum and spatiotemporal power distribution results from the simulation of a two-color pumped OPCPA-system	50
3.8	Overview of different OPA-regimes in the two non-collinear phase-matching geometries	54
3.9	Wavelength depended beam quality factor $M^2(\lambda)$ with respect to the angular integrated signal output spectrum	55
3.10	Overview of the compressibility of different OPA-regimes	57
4.1	Simplified schematic of a synchronously pumped non-collinear optical parametric oscillator	66
4.2	Illustration of the chaotic pulse formation in a broadly phase-matched NOPO without sufficient positive dispersion	67
4.3	Schematic of the widely tuneable non-collinear optical parametric oscillator setup	68
4.4	NOPO internal net dispersion for different amounts of glass	70
4.5	Longterm stability and beam quality of the tuneable NOPO	71
4.6	Power slope and RF-noise measurement of the tuneable NOPO	72
4.7	Intensity autocorrelation and RF-noise measurement of the tuneable NOPO in stable and unstable conditions	73
4.8	NOPO tuning behaviour with moderate dispersion	74
4.9	Spectral bandwidth and uncompressed pulse duration of the tuneable NOPO	76
4.10	Compressed pulses of the tuneable NOPO	77
4.11	Tuneability of the signal wavelength by changing the resonator length of the NOPO	79
4.12	PVWC-NOPO optimized for wide and smoothed spectral tuneability	80
4.13	Fast spectral ramping of the NOPO signal wavelength and cross-correlation trace with the IR-pump pulse	82
4.14	TPG-NOPO optimized for wide and smoothed spectral tuneability	83
4.15	Schematic setup of two-foci NOPO with KLM-mode coupling and breathing pulse dispersion management	86
4.16	Calculated beam radius in the two-foci NOPO	86
4.17	First results from the two-foci NOPO with optimized Kerr-lens action	89
6.1	Principle of the adapted split-step numerical model for the NOPO simulation	97
6.2	Comparison of experimental and simulated highly dispersive NOPO	98

6.3 Principle of the adapted split-step numerical model for the NOPO simulation	99
---	----

Appendix A

Acknowledgements (German)

Ein sehr schöner und wichtiger Teil am Ende einer solchen Arbeit ist es, sich bei allen Menschen zu bedanken, die direkt oder indirekt am Gelingen beteiligt waren.

An erster Stelle möchte ich Uwe Morgner danken, der mir die Möglichkeit gegeben hat in einem solch faszinierenden aber auch ergiebigen Themengebiet zu forschen.

Bei Prof. Franz Kärtner und Prof. Christian Ospelkaus bedanke ich mich für die Übernahme des Koreferats und bei Prof. Manfred Lein für den Vorsitz bei der Disputation.

Mein besonderer Dank gilt meinen lieben alten Kollegen aus Heidelberger und den neueren aus Diplomzeiten, die, nachdem ich eigentlich schon den Weg in die Wirtschaft angetreten hatte, sich genau im richtigen Moment an mich erinnerten und mir damit diesen Weg eröffneten. Mein Dank wird euch ewig nachschleichen¹.

Vielen Dank an die OPCPA-Künstler Anne und Jan für die tolle Zusammenarbeit; ein großer Teil der präsentierten Ergebnisse basiert darauf. Für das Gelingen einer solchen Arbeit, die sich ja immerhin über vier Jahre erstreckt, sind aber auch erquickende Diskussionen, Humor und lustige Momente, aber auch die Möglichkeit jemandem sein Leid zu klagen, kurzum ein positives Betriebsklima, unbezahlbar. Ich möchte mich von ganzem Herzen bei allen Menschen bedanken, die jeden Tag aufs Neue zu diesem wunderbaren Umfeld beigetragen haben. Mein besonderer Dank gilt hier meinen Kollegen und Freunden (in zufälliger Reihenfolge:) Thomas, Stefan, Anne, Moritz, Marcel, Guido, Hauke, Heiko und Martin, aber auch allen anderen lieben Kollegen, die nicht im Einzelnen aufgeführt sind.

An dieser Stelle möchte ich mich auch ganz herzlich bei der gesamten Werkstatt und dem gesamten Sekretariat bedanken. Besonders Frau Hünitzsch muss hier Erwäh-

¹Sächsische Redewendung

nung finden, die mir nicht nur einmal mit Rat und Tat aus übelster Misere geholfen hat. Manche Dinge bleiben wohl unvergessen.

A special thank you goes out to the greatest proofreaders ever. Julia, Jose, Moritz and especially Thomas, you guys were amazing!

Zum Schluss möchte ich noch ein besonders herzliches Dankeschön an meine liebe Familie und meine engen Freunde in der Heimat schicken, nicht zu vergessen meine großartige Edi, die mir während des Schreibens alle Sorgen vom Hals gehalten hat.

Vielen Dank euch allen!

Appendix B

Curriculum Vitae

Personal Details

Tino Lang
Comeniusstraße 16
30451 Hannover

born 7th of June, 1978 in Reichenbach/Vogtl., Germany
unmarried, German

Professional Experience

02/2008–04/2010 Full time job: Laser Zentrum Hannover e.V., Laser Development Department, Space Technologies Group, Development and qualification of a flight model UV laser for the ESA/NASA Mission ExoMars (DLR)

01/2001–07/2001 Full time job: Sächsisch-Bayerische Starkstrom-Gerätebau GmbH

Ph.D. Studies

since 05/2010 Ph.D. student at the Institute of Quantum Optics at the Leibniz Universität Hannover, research group of Prof. Dr. Uwe Morgner

2011 Theoretical exam in Quantum Mechanics at the Leibniz Universität Hannover

Related Work Experience

04/2006–10/2006 Intern: Michigan State University, East Lansing, USA, Fraunhofer USA inc. CLL, Miniature microwave plasma discharge for local area materials processing

09/2004–02/2005 Intern: Max-Planck-Institut für Kernphysik, Heidelberg, research group of Dr. Uwe Morgner, Development and assembly of a "reaction micro-scope" for multi-photon ionization of noble gas atoms

Education

- 02/2008 Final degree: Diplom-Ingenieur (FH) - mark "very good"
- 01/2007–01/2008 Diploma student at the Institute of Quantum Optics at the Leibniz Universität Hannover, research group of Prof. Dr. Uwe Morgner,
project: *Development of a high power RGB nonlinear wavelength conversion system*
- 10/2002–02/2008 Studies in Physical Technology at the University of Applied Sciences Zwickau (WHZ) / Zwickau
- 08/2001–06/2002 Fachoberschule Reichenbach/Vogtl.
Advanced Technical College Certificate
- 03/1999–12/2000 Military Service, Regensburg, maintenance of the digital communication network of the Air Force
- 08/1995–07/1998 Training in Industrial Mechanics and Energy Electronics

Appendix C

Scientific Publications

Journal Publications

1. T. LANG, A. HARTH, J. MATYSCHOK, T. BINHAMMER, M. SCHULTZE AND U. MORGNER
Impact of temporal, spatial and cascaded effects on the pulse formation in ultra-broadband parametric amplifiers, Optics express **21** (1), 949-959 (2013)
2. T. LANG, T. BINHAMMER, S. RAUSCH, G. PALMER, M. EMONS, M. SCHULTZE, A. HARTH AND U. MORGNER
High power ultra-widely tuneable femtosecond pulses from a non-collinear optical parametric oscillator (NOPO), Optics express **20** (2), 912-917 (2012)
3. J. MATYSCHOK, T. LANG, T. BINHAMMER, O. PROCHNOW, S. RAUSCH, M. SCHULTZE, A. HARTH, P. RUDAWSKI, C. L. ARNOLD, A. L'HUILLIER AND U. MORGNER
Temporal and spatial effects inside a compact and CEP stabilized, few-cycle OPCPA system at high repetition rates, Optics express **21** (24), 29656-29665 (2013)
4. A. HARTH, M. SCHULTZE, T. LANG, T. BINHAMMER, S. RAUSCH AND U. MORGNER
Two-color pumped OPCPA system emitting spectra spanning 1.5 octaves from VIS to NIR, Optics express **20** (3), 3076-3081 (2012)
5. M. SCHULTZE, T. BINHAMMER, G. PALMER, M. EMONS, T. LANG AND U. MORGNER
Multi- μ J, CEP-stabilized, two-cycle pulses from an OPCPA system with up to 500 kHz repetition rate, Optics express **18** (26), 27291-27297 (2010)
6. S. DEWALD, T. LANG, C. SCHRÖTER, R. MOSHAMMER, J. ULLRICH, M. SIEGEL AND U. MORGNER

Ionization of noble gases with pulses directly from a laser oscillator, Optics letters **31** (13), 2072-2074 (2006)

Contributions to International Conferences

1. Lasers and Electro-Optics Europe (CLEO EUROPE/IQEC), **CFIE-9-4**, 2013, Munich, Germany
Oral Presentation: *Impact of parasitic, cascaded, and spatial effects to the spatio-temporal pulse shaping dynamics in optical parametric amplifiers*
T. LANG, A. HARTH, M. SCHULTZE AND U. MORGNER
2. Ultrafast Phenomena (UP), 2012, Lausanne, Switzerland
Spectral high-speed sweeping of high power fs-pulses from a Non-collinear Optical Parametric Oscillator (NOPO)
T. LANG, T. BINHAMMER, S. RAUSCH, G. PALMER, M. EMONS, M. SCHULTZE, A. HARTH AND U. MORGNER
3. Advanced Solid-State Photonics (ASSP), **AT2A.2**, 2012, San Diego, USA
Oral Presentation: *Rapidly Spectral Ramping of an Ultra-wide Tuneable Femtosecond Non-collinear Optical Parametric Oscillator (NOPO) with High Average Output Power*
T. LANG, T. BINHAMMER, S. RAUSCH, G. PALMER, M. EMONS, M. SCHULTZE, A. HARTH AND U. MORGNER
4. Lasers and Electro-Optics Europe (CLEO EUROPE/IQEC), **CF6-5**, 2011, Munich, Germany
Oral Presentation: *Tuneable Broadband Optical Parametric Oscillator Pumped by an Yb:KLu(WO₄)₂ Thin-Disk Laser Oscillator*
T. LANG, T. BINHAMMER, S. RAUSCH, G. PALMER, M. SCHULTZE AND U. MORGNER
5. Frontiers in Ultrafast Optics: Biomedical, Scientific, and Industrial Applications XIV, **Proc. SPIE 8972**, 2014, San Francisco, USA
Compact, high-repetition rate OPCPA system for high harmonic generation
J. MATYSCHOK, T. BINHAMMER, T. LANG, O. PROCHNOW, S. RAUSCH, P. RUDAWSKI, A. HARTH, M. MIRANDA, C. GUO, E. LOREK, J. MAURITSSON, C. L. ARNOLD, A. L'HUILLIER AND U. MORGNER
6. Advanced Solid State Lasers, **AF2A.2**, 2013, Paris, France
Compact, few-cycle OPCPA system with ultralow CEP noise

- J. MATYSCHOK, T. BINHAMMER, T. LANG, O. PROCHNOW, S. RAUSCH, P. RUDAWSKI, M. MIRANDA, C. ARNOLD, A. L'HUILLIER AND U. MORGNER
7. Lasers and Electro-Optics Europe (CLEO EUROPE/IQEC), **CD-P-40**, 2013, Munich, Germany
Stimulated Raman scattering with a rapidly tunable non-collinear optical parametric oscillator
C. HOFFMANN, T. LANG AND U. MORGNER
 8. Lasers and Electro-Optics Europe (CLEO EUROPE/IQEC), 2013, Munich, Germany
4-f prism-based pulse shaper supporting single-cycle pulses in the visible
A. HARTH, T. NAGY, J. ANDRADE, S. RAUSCH, C. HOFFMANN, T. LANG, T. BINHAMMER AND U. MORGNER
 9. Lasers and Electro-Optics Europe (CLEO EUROPE/IQEC), **CFIE-9-1**, 2013, Munich, Germany
Ultra-stable fiber pumped CEP-stabilized dual stage OPCPA System
J. MATYSCHOK, T. BINHAMMER, T. LANG, O. PROCHNOW, S. RAUSCH, P. RUDAWSKI, C. ARNOLD, A. L'HUILLIER AND U. MORGNER
 10. CLEO: Science and Innovations, **CTh1N.5**, 2012, San Jose, USA
Spectra spanning over 1.5 Octaves from a Two-Color Pumped OPCPA System
A. HARTH, M. SCHULTZE, T. LANG, T. BINHAMMER, S. RAUSCH AND U. MORGNER
 11. Ultrafast-Phenomena (UP), 2012, Lausanne, Switzerland
Sub-100nm Structures by 3D Two-Photon Polymerization Using Few-Cycle-Laser Sources
M. EMONS, K. OBATA, M. SCHULTZE, T. LANG, T. BINHAMMER AND U. MORGNER
 12. Ultrafast Phenomena (UP), 2012, Lausanne, Switzerland
High repetition rate two-color pumped OPCPA system with a spectral bandwidth of 1.5 octaves from VIS to NIR
A. HARTH, M. SCHULTZE, T. LANG, S. RAUSCH, T. BINHAMMER AND U. MORGNER
 13. High Intensity Lasers and High Field Phenomena (HILAS), **HT1C. 5**, 2012, Berlin, Germany
Two-color Pumped OPCPA System with μ J Pulse Energy and a Spectral Band-

- width of 1.5 Octaves from VIS to NIR*
A. HARTH, M. SCHULTZE, T. LANG, S. RAUSCH, T. BINHAMMER AND U. MORGNER
14. Advanced Solid-State Photonics (ASSP), **AM4A.8**, 2012, San Diego, USA
Two color pumped OPCPA system delivering a 1.5 octave spanning coherent spectrum in the visible
A. HARTH, M. SCHULTZE, T. LANG, T. BINHAMMER AND U. MORGNER
15. Advanced Solid-State Photonics (ASSP), **AT4A.14**, 2012, San Diego, USA
Mode fluctuations in end-pumped passively Q-switched solid-state lasers
T. HÜLSENBUSCH, A. BÜTTNER, M. ERNST, T. LANG, C. KOLLECK, D. KRACHT AND J. NEUMANN
16. Lasers and Electro-Optics Europe (CLEO EUROPE/IQEC), **CF6-2**, 2011, Munich, Germany
Compact OPCPA System Generating CEP-stabilized Two-cycle Pulses with Repetition Rates up to 500 kHz
M. SCHULTZE, T. BINHAMMER, M. EMONS, T. LANG AND U. MORGNER
17. Advanced Solid-State Photonics (ASSP), **AWB3**, 2011, Istanbul, Turkey
High peak power from a mode-locked two-crystal Yb:KYW oscillator with cavity-dumping
G. PALMER, M. EMONS, M. SCHULTZE AND U. MORGNER
18. Advanced Solid-State Photonics (ASSP), **AMD2**, 2011, Istanbul, Turkey
CEP Stable, High Repetition Rate, Two-cycle Pulses from an OPCPA System with μ J Pulse Energies
M. SCHULTZE, T. BINHAMMER, G. PALMER, M. EMONS, T. LANG AND U. MORGNER
19. Lunar and Planetary Institute Science Conference Abstracts, **No. 1533, p. 1170**, 2010, The Woodlands, USA
Analysis of Mineral Soil Analog Samples with a Pulsed UV-Laser Source
M. HILCHENBACH, T. LANG, J. NEUMANN AND N. TARCEA
20. International Conference on Space Optics **4, (8)**, 2010, Rhodes, Greece
Development of a pulsed UV laser system for laser-desorption mass spectrometry on Mars
C. KOLLECK, A. BÜTTNER, M. ERNST, T. HÜLSENBUSCH, T. LANG, R. MARWAH, S. MEBBEN, M. PRIEHS, D. KRACHT AND J. NEUMANN

21. Proc. European Planetary Sci. Congr (EPSC) **4**, (2009-624), 2009, Potsdam, Germany
Development of a pulsed ultraviolet solid-state laser system for Mars surface analysis by laser desorption/ionization mass spectroscopy
J. NEUMANN, M. ERNST, F. GOESMANN, M. HILCHENBACH, A. KOCH, T. LANG, R. MARWAH, S. MEBBEN, A. MOALEM, O. RODERS, A. SCHNEIDER, E. STEINMETZ, I. SZEMEREY, C. WAGNER, C. KOLLECK AND D. KRACHT
22. Lunar and Planetary Institute Science Conference Abstracts **40**, (1162), 2009, The Woodlands, USA
UV-Laser Desorption Ion Source Applied to a Secondary Ion Mass Spectrometer
M. HILCHENBACH, T. LANG, K. HORNUNG, L. THIRKELL AND C. BRIOIS

